



University of
Stavanger

Faculty of Science and Technology

MASTER'S THESIS

Study program/Specialization: Petroleum Geosciences Engineering	Spring Semester, 2018 Open Access
Writer: Luís Marçal Correia Deyrieux Centeno	<hr/> (Writer's signature)
Faculty supervisor: Nestor Cardozo	
Title of thesis: Thermal evolution of the Nordkapp Basin and implications for its petroleum system	
Credits (ECTS): 30	
Keywords: Basin Modeling Thermal evolution Salt structures Nordkapp Basin	Pages: 94 Stavanger, June 15 th 2018

Copyright

by

Luís Marçal Correia Deyrieux Centeno

2018

Thermal evolution of the Nordkapp Basin and implications for its petroleum system

By

Luís Marçal Correia Deyrieux Centeno

Master Thesis

Presented to the Faculty of Science and Technology

University of Stavanger



The University of Stavanger

June 2018

Acknowledgements

The author of this thesis express special gratitude to:

Faculty supervisor Nestor Cardozo for his exceptional guidance, academic support and knowledge.

Luis Alberto Rojo Moraleda for providing the 2D structural restorations, for his time, academic knowledge and support.

Andrés Felipe Cedeño Motta for helping with the introduction of the PetroMod software, for his time and effort for discussion, discernment and proofreading.

The University of Stavanger for hosting me in this new environment, providing the workstation and the articles needed for the background knowledge, also to NPD for the well dataset and to Schlumberger for providing PetroMod license.

My parents (João Pedro Centeno and Ana Teresa Centeno) for their unconditional support, and my brothers (Miguel Centeno and Inês Centeno) for believing in me. Without my family, I would not be able to finish my Master Degree.

My girlfriend (Paula Dias) for her patience, love and support throughout my two-year Master Degree away from her.

My very good friends Khushal Adlakha, Eirinaios Chatzillari, Chalong Jaruwattanasakul, and Theodoros Rozos for sharing this new academic chapter with me and for their true friendship.

Thermal evolution of the Nordkapp Basin and implications for its petroleum system

Abstract

The Nordkapp Basin is an elongated salt-bearing basin that developed during Late Palaeozoic-Early Mesozoic rifting in the southwestern Barents Sea. The presence of salt structures within the basin modified its temperature distribution and evolution. This thesis focuses on two sections across the eastern and east-central sub-basins of the Nordkapp Basin. By using a paleo-stepping approach, the modeling enables integrating structural restoration and thermal modelling of the sections to determine the impact of salt related structures on the geothermal history of the Basin and implications on its petroleum system. The results show that salt diapirs induced a significant negative thermal anomaly, retarding maturation and generation of neighboring source rocks, as a function of the overlying sediments and salt structural evolution. Furthermore, salt structures enabled optimum reservoir temperatures for hydrocarbon preservation. Essential elements of the petroleum system include source rock limestones and shales from Late Permian and Early Triassic age, Middle to Late Triassic siliciclastic reservoirs, and Jurassic to Cenozoic overburden strata. Traps include reservoir beds pinching towards the salt structures, and traps at the basin boundaries associated with suprasalt faults, both sealed at the top by Cenozoic shales. Modeling the thermal influence of salt structures in the Nordkapp Basin allows generating new exploration models for the basin, and salt-related basin alike in the Barents Sea.

Contents

Acknowledgements	iv
Abstract	v
Contents	vi
List of Figures	viii
List of Tables	xi
1. Introduction.....	1
1.1. Background theory	2
1.2. Description of the problem.....	5
2. Geological Setting.....	5
2.1. Introduction	5
2.2. Evolution	6
2.2.1. Late Paleozoic	7
2.2.2. Triassic – Early Jurassic.....	8
2.2.3. Middle Jurassic – Early Cretaceous	8
2.2.4. Late Cretaceous – Cenozoic.....	9
3. Dataset.....	12
4. Methodology	13
4.1. Burial and thermal history	13
4.2. Model Building	14
4.3. Structural Restorations	16
5. Input	16
5.1. Boundary conditions	16
5.2. Kerogen Maturation	21
5.3. Structural Restorations	21
6. Results.....	23
6.1. Section 1.....	24
6.1.1. Lithology and structural evolution.....	24
6.1.2. Temperature evolution	26
6.1.3. Reservoir temperature evolution.....	28
6.1.4. Maturation of source rocks	30
6.2. Section 2.....	32
6.2.1. Lithology and structural evolution.....	32

6.2.2.	Temperature evolution	34
6.2.3.	Reservoir temperature evolution.....	36
6.2.4.	Maturation of source rocks	38
7.	Discussion	40
7.1.	Impact of halokinesis on petroleum system	41
7.1.1.	Thermal influence	41
7.1.2.	Potential petroleum system on the Nordkapp Basin	44
7.2.	Level of certainty	47
7.3.	Model Limitations and Mitigation	47
7.4.	Implications and future work	51
8.	Conclusions.....	51
9.	References.....	53
	Appendix.....	58
10.	Section 1.....	59
10.1.	Porosity Evolution	59
10.2.	Thermal Evolution.....	62
10.3.	VRo Maturation Evolution	66
11.	Section 2.....	70
11.1.	Porosity Evolution	70
11.2.	Temperature Evolution	74
11.3.	VRo Maturation Evolution	78
12.	Reservoir rock temperature/time plots.....	82
12.1.	Section 1	82
12.2.	Section 2	83

List of Figures

- Figure 1** – Inset map on the left shows the location of the Nordkapp Basin in the Norwegian Continental Shelf. The main map illustrates the principal structural elements of the Nordkapp Basin, including the Norsel high, Bjarmeland and Finnmark Platforms together with the location of the exploration wells (red) used in this study. (NPD Factpages, 2003)2
- Figure 2** - A) Vertical steady-state temperature gradient for a shale section with (solid line) and without (dashed line) salt (Jackson and Hudec, 2017). B) Thermal conductivity of different rocks and water as a function of temperature (Jackson and Hudec, 2017). Notice the high thermal conductivity of salt.3
- Figure 3** - A) Thermal evolution around salt structures (Jackson and Hudec, 2017). B) Zoom in of case (d) illustrating the area of thermal anomalies in red, which closely resemble the study case.....4
- Figure 4** - A) Main structural elements of the Barents Sea. The Tromsø, Nordkapp, and Tiddlybanken basins are salt-related basins with abundant diapiric structures. Inset map shows the location of the Barents Sea in the Arctic region. B) Main structural elements of the Nordkapp Basin. The basin is divided in three minibasins: western, central, and eastern minibasins. Black dots are exploration wells. Inset map displays the seismic data used by Rojo et al. (submitted). C) Regional profile illustrating the changes in structural style and geometries of the Barents Shelf between the Nordkapp Basin and the Atlantic margin (Henriksen et al., 2011). Vertical exaggeration is 10.6
- Figure 5** – A) The upper figure illustrates the location of the Barents Sea within the Arctic. The lower figure displays a tectonic basemap of the western Barents Sea area, with bathymetry (Jakobsson et al., 2008) and basin rifting/subsidence phases (Faleide et al., 2008). The figure also illustrates the location of the wells and seismic profile displayed in figure B. B) Interpreted and depth-converted seismic profile by Clark et al., (2014). Vertical exaggeration is 10. VVP, Vestbakken Volcanic Province; BB, Bjørnøya Basin; LH, Loppa High/Selis Ridge; OB, Ottar Basin; NB, Nordkapp Basin. C) Stretching factors for (a) Late Carboniferous rift phase, (b) Late Permian rift phase, (c) Late Jurassic rift phase, (d) Paleocene-Eocene rift phase (Clark et al., 2014). The red rectangles indicate the location of the Nordkapp Basin. 10
- Figure 6** - Lithostratigraphic column for the south-west Barents Sea by Clark et al. (2014). Modelled rift phases shown in right column, spanning the duration of rifting. Dotted black lines show the age of instantaneous rifting assigned in the basin model. Lithostratigraphy key – basement: red; continental sand: orange; continental shales: green; carbonates: blue; marine sand: yellow; marine shale: grey; undifferentiated: brown; missing section: white. Time scale after Gradstein et al. (2004). 11
- Figure 7** – A) Petroleum Geochemistry Report - NOCS well 7228/7-1A –1S (NPD Factpages, 2003). B) Map showing the position of the provided sections and their relation to the wells (red circles) (Rojo et al., submitted). 12
- Figure 8** - Crust and Lithosphere Properties entered to the software Genesis. This together with the VRo data, the burial history of the pseudowell, and the stretch factors from Clark et al. (2014), allowed the software to estimate the basin’s heat flow through time. 13

Figure 9 - 2D TecLink workflow	14
Figure 10 - On the left: Age to layer assignment; On the right: Block definition associated to their respective layers	16
Figure 11 - Bottom: pseudo-well position in the eastern minibasin. Top Left: Vitrinite Reflectance data from the selected two wells: logarithmic fit in red, average fit in orange, and the two linear fits used for calibration in the model in purple. Top right: Map showing the position of the section and the pseudo-well (black) and the wells with vitrinite data (green). Bottom: Cross section with pseudowell.....	18
Figure 12 - Genesis model at the location of the pseudowell. A) On the left: VRo data showing the 1 st trendline of combine VRo data from the wells; On the right: Present day burial history (red rectangle) and respective heat flow value. B) On the left: VRo data showing the 2 nd trendline corresponding to the last major rift event; On the right: Last rift related burial history showing the estimated heat flow value in the red rectangle. C) Late Permian rift phase showing estimated heat flow value in the red rectangle area. D) Late Carboniferous rift phase showing estimated heat flow value in the red rectangle.....	19
Figure 13 – Boundary conditions of the thermal model. Top: Paleowater depth (PWD), sediment water interface temperature (SWIT) and heat flow (HF) through time. Bottom: Zoom in of heat flow trend plot showing the times at which the heat flow was introduced in the model (red rectangles): A) Late Carboniferous rift; B) Late Permian rift; C) Late Jurassic rift; D) Present day.	20
Figure 14 - Facies definition. Association of the main source rocks with respective kinetics, TOC and HI values from Peters et al. (2005).	21
Figure 15 - Sequential structural restorations of two sections, one across the eastern minibasin (section 1), and the other across the eastern central minibasin (section 2). From Rojo et al. (submitted). Inset map shows the lines of the sections.....	22
Figure 16 – Lithological and structural evolution of section 1, including the timing of rifting events.	25
Figure 17 - Thermal evolution of section 1.....	27
Figure 18 - Present day temperature from two pseudo-wells to the N (A) and S (B) of the main salt structure in section 1. Present day reservoir rock temperatures are shown by the red rectangles. Location of the wells is shown in Figure 29 I.	28
Figure 19 - Reservoir temperature evolution in section 1.....	29
Figure 20 – Evolution of source rock maturation in section 1.....	31
Figure 21 – Lithological and structural evolution of section 2, including the timing of rifting events	33
Figure 22 -Thermal evolution of section 2.....	35
Figure 23 - Present day reservoir temperatures for four pseudo-wells along the section. Location of wells is shown in Figure 29 II.	36
Figure 24 – Evolution of reservoir temperatures in section 2.....	37
Figure 25 – Evolution of source rock maturation in section 2.....	39

Figure 26 - Subsidence rate of the Nordkapp basin at pseudowell (section 1).....	40
Figure 27 - Thermal behavior of the sag-basin in the first stage of its evolution from section 1; red circle shows the thermal response of salt from the radiogenic heat flow.	41
Figure 28 – Restorations (Rojo et al., submitted) showing possible migration of hydrocarbons and entrapment zones (red arrows). Left) Section 1; Right) Section 2.....	45
Figure 29 - Reservoir average temperature/time plots. I) section 1 pseudowells position and their respective reservoir temperature; II) section 2 pseudowells position and their respective reservoir temperature.	46
Figure 30 - Overlap of restoration 1 with the altered model showing the range of modifications. The blue marks represent the top width and the orange marks represent the bottom width. “a” represents the unaltered shape and “b” represents the altered one.....	49
Figure 31 - 2D TeckLink Block building limitation and solution. a) Present day Paleo Section with problematic area within the red square. b) Close up of the problematic area in red shows the limitation of the software. c) Mitigation by a 200m upward shift of the Kobbe Formation fault block indicated by the blue arrow.....	50
Appendix	
Figure 32 - Porosity modeled data from section 1 pseudowells. (1) Present day; (2) 100 My; (3) 152 My; (4) 208 My; (5) 220 My); (6) 250 My; (7) 290 My.....	62
Figure 33 - Temperature modeled data from section 1 pseudowells. (1) Present day; (2) 100 My; (3) 152 My; (4) 208 My; (5) 220 My); (6) 250 My; (7) 290 My	65
Figure 34 – Vitrinite Reflectance modeled data from section 1 pseudowells. (1) Present day; (2) 100 My; (3) 152 My; (4) 208 My; (5) 220 My); (6) 250 My; (7) 290 My	69
Figure 35 - Porosity modeled data from section 2 pseudowells. (1) Present day; (2) 100 My; (3) 152 My; (4) 208 My; (5) 220 My); (6) 250 My; (7) 290 My.....	73
Figure 36 - Temperature modeled data from section 2 pseudowells. (1) Present day; (2) 100 My; (3) 152 My; (4) 208 My; (5) 220 My); (6) 250 My; (7) 290 My	77
Figure 37 – Vitrinite Reflectance modeled data from section 2 pseudowells. (1) Present day; (2) 100 My; (3) 152 My; (4) 208 My; (5) 220 My); (6) 250 My; (7) 290 My	81
Figure 38 - Reservoir temperature to time plots for section 2. (1) Maximum temperature values of the reservoir units; (2) Minimum temperature values of the reservoir units; (3) Average temperature values of the reservoir units.	82
Figure 39 - Reservoir temperature to time plots for section 2. (1) Maximum temperature values of the reservoir units; (2) Minimum temperature values of the reservoir units; (3) Average temperature values of the reservoir units.	83

List of Tables

Table 1 - Assigned Ages of Paleo Sections.....	15
Table 2 - Major events associated with β -factors and estimated heat flow.....	17
Table 3 - Numerical values of temperature related to depth and position for section 1. The column in yellow is at the position of the salt diapir.	42
Table 4 - Numerical values of temperature related to depth and position for section 2. The columns in yellow are at the position of the salt diapirs.....	43
Table 5 - Quantitative geometrical alterations of the salt structures.....	49

1. Introduction

The study area is the Nordkapp Basin, which is located in the southwest Barents Sea (Figure 1). The Nordkapp Basin is a NE-SW-trending, salt-bearing basin developed during Late Paleozoic rifting. The presence of large thicknesses of Pennsylvanian-Lower Permian layered evaporite sequences (LES) and their subsequent Mesozoic and Cenozoic mobilization generated numerous salt structures, which could be potential structural and stratigraphic hydrocarbons traps (Gabrielsen et al., 1992; Jensen and Sørensen, 1992; Koyi et al., 1995a; Koyi et al., 1993, 1995b; Nilsen et al., 1995; Stemmerik, 2000).

Most of the exploration wells have been drilled at the basin's rim, targeting structural traps above salt pillows, while only three wells have been drilled through salt minibasins targeting sediment truncations against salt diapirs (Figure 1). Well 7228/7-1A was the only well drilled in salt minibasins which made a non-commercial discovery (Pandora discovery), proving the existence of a working petroleum system within the basin. This discovery consisted of oil and gas bearing sandstones from the Middle to Upper Triassic (Snadd Formation) and Lower Triassic (Klappmyss Formation) intervals (NPD FactPages, 2018).

Exploration within the Norwegian Barents Sea, including the Goliat discovery in the Hammerfest Basin and the Pandora discovery in the Nordkapp Basin (Henriksen et al., 2011b; Lundschieen et al., 2014; Stadtler et al., 2014) have proven the presence of Triassic units such as Fruholmen, Snadd, Kobbe, and Havert Formations with potential reservoir intervals. Also, newly discoveries in the Loppa High like Alta, Gotha and Neiden are interpreted to have been generated by Triassic source rocks (Petersen et al., 2018). The Templefjorden Group and Havert Formation are known hydrocarbon plays on the Finnmark Platform and Loppa High (Jafarian et al., 2017). Some of these intervals can be found at relatively large depths (e.g. > 4 km) in the Nordkapp Basin due to the impact of Triassic halokinesis. Therefore, there is a risk that these deeply buried source rocks are overmatured.

However, previous studies by Mello et al. (1995) and McBride et al. (1998) have shown that potential reservoirs and source rocks can be found in the Gulf of Mexico and offshore Brazil at large depths due to the presence of highly thermal conductive salt structures. Hence, this unlocks the potential for similar scenarios in the salt-bearing basins of the Barents Sea.

The purpose of this thesis is to explore the role of the negative thermal anomaly induced by salt structures in modifying the thermal history of the Nordkapp Basin and maturation of source rocks. To accomplish the objective, this study uses 2D structural restorations of the basin together with thermal modelling through time.

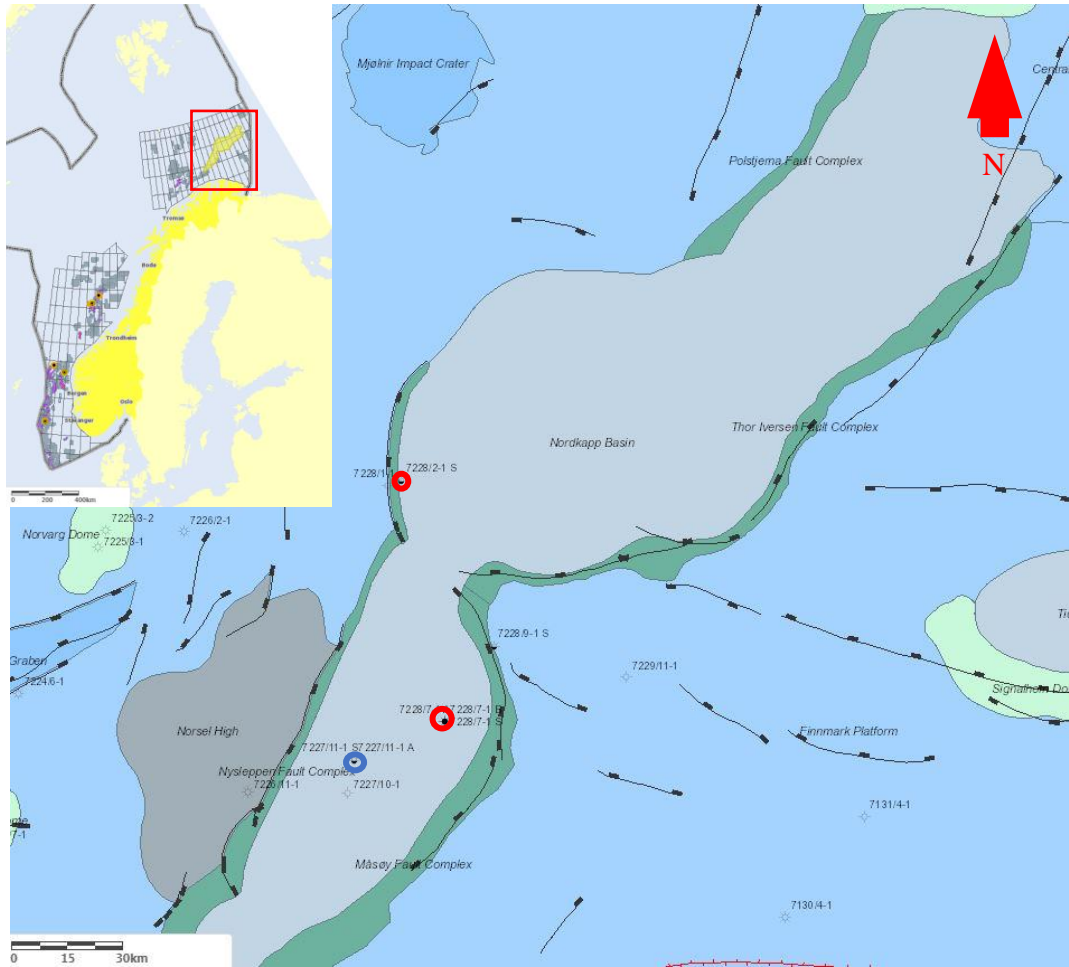


Figure 1 – Inset map on the left shows the location of the Nordkapp Basin in the Norwegian Continental Shelf. The main map illustrates the principal structural elements of the Nordkapp Basin, including the Narsjø high, Bjarmeland and Finnmark Platforms together with the location of the exploration wells (red) used in this study. (NPD Factpages, 2018)

1.1. Background theory

Modelling of the temperature distribution around various salt structures shows that in general the refraction of heat flow within salt induces a dipole-shaped temperature anomaly; a positive anomaly towards the top of the salt structure and a negative anomaly towards its base (Mello et al., 1995). The negative anomaly towards the base and at the lateral boundaries of the salt structure will receive more attention in this thesis. There are two main factors contributing to these thermal anomalies: (1) the difference in thermal conductivity between the salt and the surrounding sediments (Figure 2), and (2) the geometry of the salt structure (Mello et al., 1995). The thermal conductivity of salt (halite and anhydrite) is around $5.5 \text{ Wm}^{-1}\text{C}^{-1}$ at $100 \text{ }^\circ\text{C}$, while shales may have conductivities between 1.0 and $2.5 \text{ Wm}^{-1}\text{C}^{-1}$ at the same temperature. Sandstones and limestones have thermal conductivities between those of shales and salt (Figure 2b) (Bjørlykke, 2015). Furthermore, these thermal conductivity contrasts enhance temperature variations by the heat flow refractive effects associated with the salt

structures (Figure 3) (Mello et al., 1995). Thus, if the conductivity of the salt is three times larger than the surrounding sediments, the distance of influence of the thermal anomalies is around two to three times the salt dome radius (O'brien and Lerche, 1984).

Salt transfers heat more efficiently from deeper strata and keeps the underlying strata anomalously cool (Mello et al., 1995; O'brien and Lerche, 1988; Waples, 1994). Therefore, a petroleum system can be significantly affected by the evolution of salt structures. The high thermal conductivity of evaporites retards the thermal maturation of source rocks in neighboring areas, causing late generation and expulsion (McBride et al., 1998).

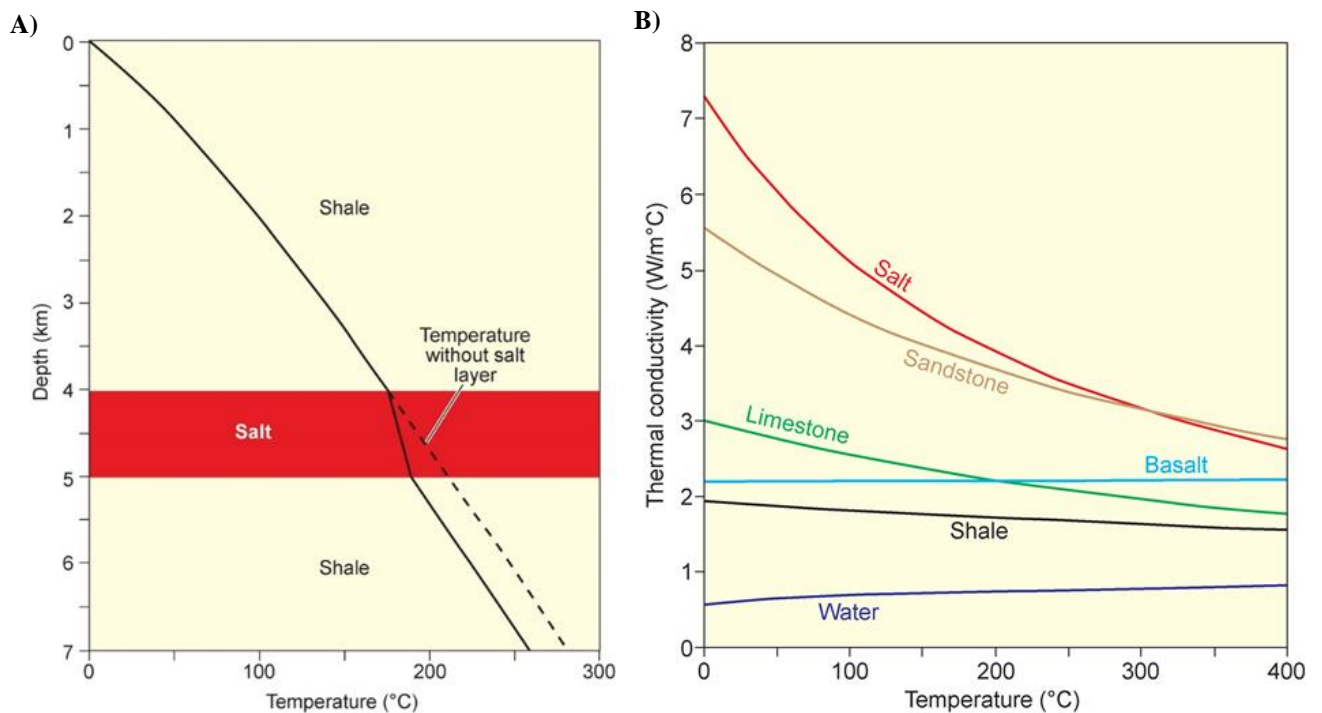


Figure 2 - A) Vertical steady-state temperature gradient for a shale section with (solid line) and without (dashed line) salt (Jackson and Hudec, 2017). B) Thermal conductivity of different rocks and water as a function of temperature (Jackson and Hudec, 2017). Notice the high thermal conductivity of salt.

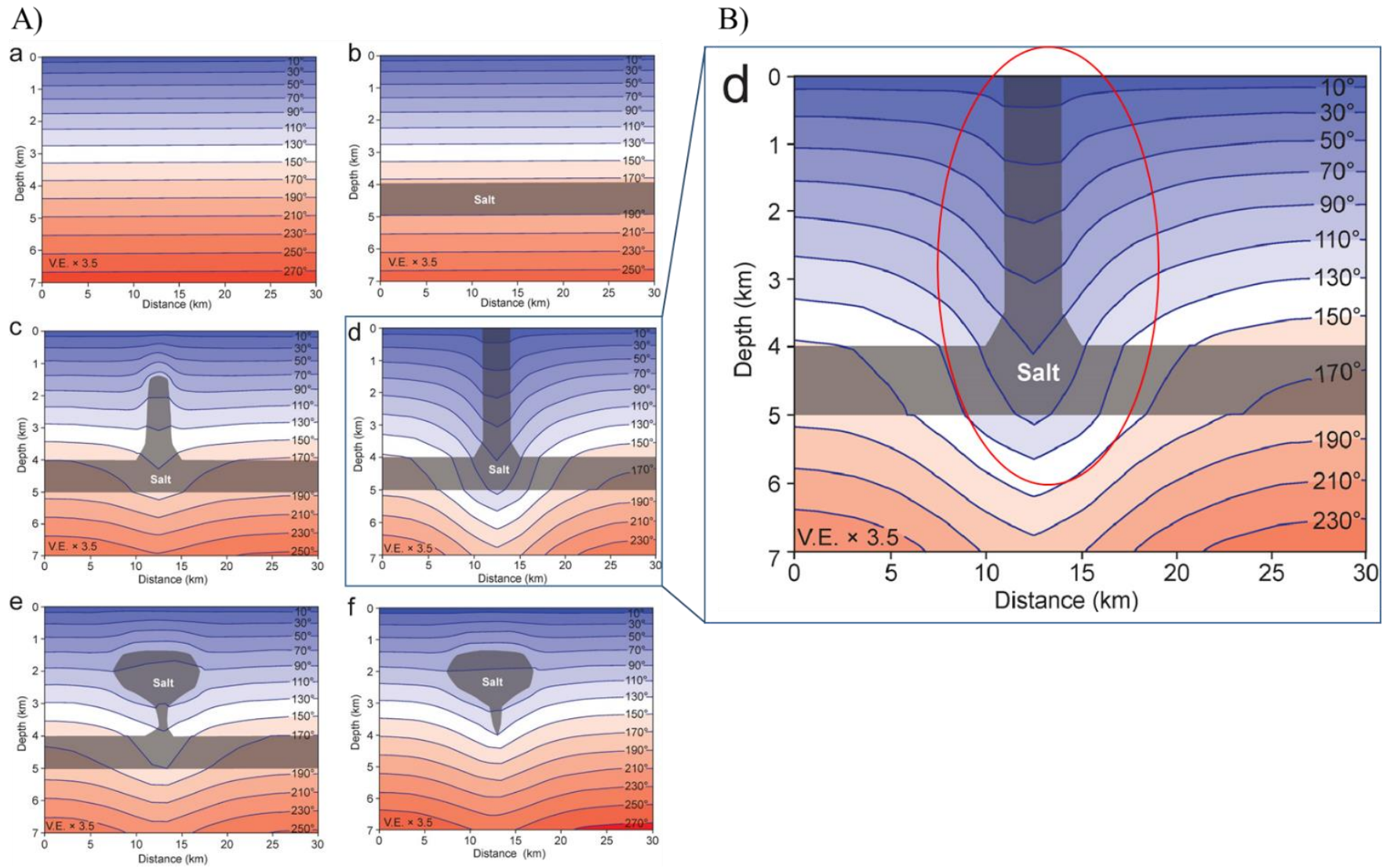


Figure 3 - A) Thermal evolution around salt structures (Jackson and Hudec, 2017). B) Zoom in of case (d) illustrating the area of thermal anomalies in red, which closely resemble the study case.

1.2. Description of the problem

There are no detailed studies regarding temperature distribution throughout the evolution of the Nordkapp Basin and therefore, the influence of salt diapirs on the maturity of source rocks and temperature of reservoirs in the surrounding minibasins remains poorly understood. This lack of understanding is also due to insufficient well data in the minibasins.

In order to better understand the thermal influence of salt in the Nordkapp Basin, this study uses 2D structural restorations of the basin at key times. Each restoration step displays differences in some of the variables that can influence the thermal history and maturation such as: (1): incremental geometry of salt structures; (2) lithologies distribution; (3) stretching factors; (4) basement geometry; (5) sedimentary thicknesses. The geometry of the basin strongly influences temperature changes. Each lithology has different thermal properties that contribute to varied behaviors under basal heat flow. The stretching factors of the rifting events that occurred in the Nordkapp Basin are also important to understand paleo-heat flow (McBride et al., 1998). The basement geometry of the Nordkapp Basin strongly controls halokinesis (Koyi et al., 1995b).

Modelling the thermal anomalies provides new constraints for source rock maturation near growing salt diapirs. In addition, it can provide new exploration concepts for reservoirs in this region. Nevertheless, present heat flow and thermal gradients are crucial to understand the thermal evolution of the basin and to constrain the boundary conditions of the model to ensure more realistic results.

2. Geological Setting

2.1. Introduction

The Barents Sea comprises the shelf area between the Kola Peninsula to the S, the shelf edge towards the Norwegian Sea to the W, Svalbard to the NW, Franz Josef Land to the NE, and Novaya Zemlya to the E ((Henriksen et al., 2011b), Figure 4). This study focuses on the Nordkapp Basin in the southwestern Barents Sea (SWBS). The Nordkapp Basin is an ENE-WSW, 100 km long basin, ranging in width from 30 to 80 km (Figure 1). It is bordered by the Finnmark Platform to the S and the Norsel High and Bjarmeland Platform to the N. In map view, the basin exhibits a dog-leg shape pattern that allows dividing it in three minibasins: western (NE-SW), central (E-W), and eastern (NE-SW) minibasins (Figure 1). The western minibasin is a half-graben, whereas the central and eastern minibasins resemble more symmetrical grabens (Gabrielsen et al., 1992). The Nordkapp Basin is one of the main salt-

bearing basins in the SWBS, and presents several types of salt structures such as salt walls, stocks, and pillows (Gabrielsen et al., 1993; Gabrielsen et al., 1990; Nilsen et al., 1995).

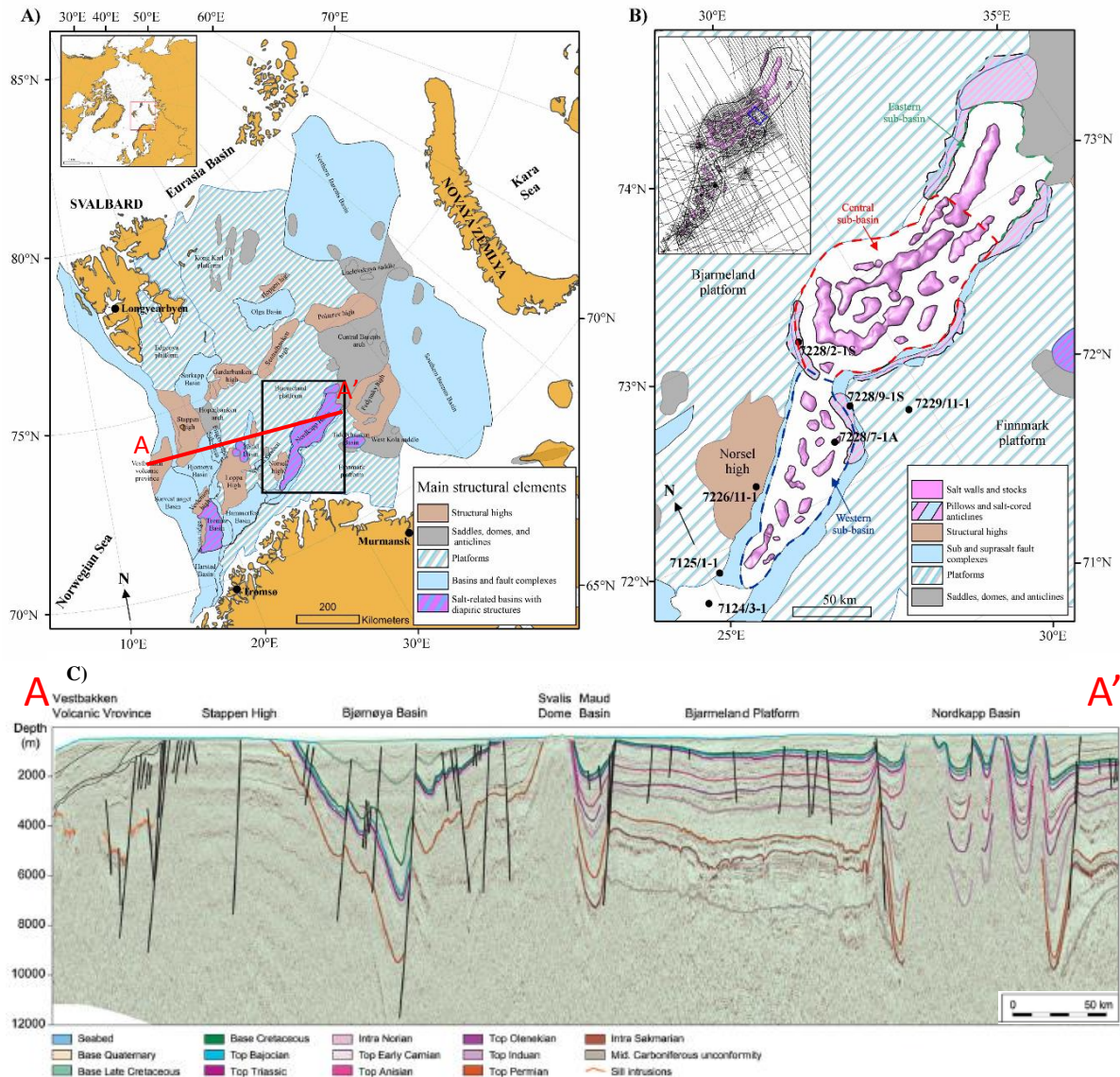


Figure 4 - A) Main structural elements of the Barents Sea. The Tromsø, Nordkapp, and Tiddlybanken basins are salt-related basins with abundant diapiric structures. Inset map shows the location of the Barents Sea in the Arctic region. B) Main structural elements of the Nordkapp Basin. The basin is divided in three minibasins: western, central, and eastern minibasins. Black dots are exploration wells. Inset map displays the seismic data used by Rojo et al. (submitted). C) Regional profile illustrating the changes in structural style and geometries of the Barents Shelf between the Nordkapp Basin and the Atlantic margin (Henriksen et al., 2011). Vertical exaggeration is 10.

2.2. Evolution

The tectonic evolution of the Barents Sea has been discussed by previous authors (Faleide et al., 1984; Faleide et al., 2008; Faleide et al., 1993; Gudlaugsson et al., 1998; Rønnevik and Jacobsen, 1984) and can be summarized in four rift phases with continuous sedimentation from the Late Paleozoic to the Cenozoic (Figure 5) (Clark et al., 2014). The

western Barents Sea has a complex distribution of structural highs, domes, platforms and basins including the Nordkapp Basin (Rojo et al., submitted) (Figure 4, C). The evolution of the Barents Sea and the Nordkapp Basin is the result of a series of tectonic processes and climatic variations that affected the Barents Sea from the Late Devonian to the present (Rojo et al., submitted, Figure 6).

2.2.1. Late Paleozoic

In the Carboniferous period, a major rifting event took place in response to the collapse of the Late Devonian-Early Carboniferous Caledonian orogen. This led to the formation of NE-SW (e.g. Nordkapp and Hammerfest basins) and NW-SE (e.g. Ottar Basin) symmetric grabens and half-grabens surrounded by structural highs and platforms (Clark et al., 2013; Fossum et al., 1999; Gernigon et al., 2014; Henriksen et al., 2011b). A recent study by Rowan and Lindsø (2017) suggests that the different along strike variations of the Nordkapp Basin are a result of two rifting episodes with different directions: (1) WNW-ESE rifting during Late Devonian to Pennsylvanian, which shaped the central minibasin, and (2) NW-SE Pennsylvanian rifting that created the western and eastern minibasins.

The Late Paleozoic sequence is characterized by significant thickness variations in the SWBS, associated with local rift grabens. These variations reflect the Carboniferous rifting, defined in Clark et al. (2014) as an initial rift phase. For this initial rifting, Clark et al. (2014) predicts a maximum stretching factor (β) of 2 around the Bjørnøya Basin and the Nordkapp Basin (Figure 4).

The Late Devonian-Early Carboniferous period was characterized by tropical humid conditions resulting in the deposition of alluvial-fluvial coaly sediments known as the Billefjorden Group (Henriksen et al., 2011b). By the end of the Paleozoic, the Barents shelf experienced a transition from humid/tropical to sub-tropical and arid due to the continental drift of Pangea towards the north (Henriksen et al., 2011b). The ongoing rifting caused basin isolation with the consequent deposition of large thickness of basinwide evaporite sequences (LES) in the basins axes (e.g. Tromsø, Nordkapp and Tyddlybanken basins), whereas platform evaporites or sabkhas occurred in the rift shoulders (e.g. Finnmark and Bjarmeland platforms) (Stemmerik et al., 1999; Stemmerik and Worsley, 2005). During the mid-Permian, the entire Barents Sea witnessed dramatic changes in oceanic circulation systems. Since a marine seaway was developed between Norway and Greenland, cool water flowed across the Barents Shelf (Stemmerik et al., 1999; Stemmerik and Worsley, 2005). This resulted in Early Permian temperate water carbonates (Gipsdalen Group) being succeeded by cool water carbonates and

cherts on the Bjarmeland (Early Permian) and Tempelfjorden (Mid Permian) Groups (Figure 6) (Larssen et al., 2005).

2.2.2. Triassic – Early Jurassic

During the Late Permian to Early Triassic, rapid subsidence occurred in response to an extensional event characterized by a β -factor ~ 1.3 , mainly on the SWBS (Clark et al., 2013; Johansen et al., 1993) (Figure 4). The subsidence from this rift event provided the accommodation space required for large volumes of clastic sedimentation. This extensional event is interpreted to be the trigger for halokinesis in salt-related basins such as the Nordkapp Basin (Gabrielsen et al., 1992; Jensen and Sørensen, 1992; Koyi et al., 1993, 1995b). Studies by Dengo and Røssland (2013) and Rowan and Lindsø (2017) suggest that NW-progradation of a clastic wedge sourced from the Uralides could be also one of the triggers of halokinesis in the Early Triassic. Sediment loading and active extensional tectonics contributed to upwards salt movement and creation of several salt structures with various geometries. Salt movement was followed by a series of shorter growth phases throughout Triassic times (Nilsen et al., 1995). This contributed to the formation of complex minibasins flanked by salt diapirs at high depths (5 to 6 km) (Jensen and Sørensen, 1992; Koyi et al., 1995a; Koyi et al., 1993, 1995b; Nilsen et al., 1995).

Recent studies show that the general sedimentation in the Barents Shelf during the Triassic was characterized by NW prograding fluviodeltaic systems. The source of this sedimentation was the Uralide Orogen in the E and the Fennoscandian Shield in the S (Glørstad-Clark et al., 2010; Klausen et al., 2015; Riis et al., 2008). The sedimentation during the Early Triassic in the Nordkapp Basin was characterized by shallow prodelta facies (Havert-Klappmyss Fms.), followed by Middle Triassic delta-front and shoreface deposits (Kobbe Formation), and finally overlaid by Late Triassic fluvio-deltaic deposits (Snadd Formation) (Henriksen et al., 2011b) (Figure 5). During the Late Triassic – Early Jurassic, the NW prograding fluviodeltaic sediments transitioned into more condensed shallow marine-fluviodeltaic deposits (Tubåen, Nordmela, and Stø Fms.) (Anell et al., 2014; Henriksen et al., 2011b).

2.2.3. Middle Jurassic – Early Cretaceous

Throughout the Middle Jurassic, the Atlantic rifting influenced the western margin of the Barents Sea shelf (Brekke et al., 2001; Tsikalas et al., 2012). However, the Nordkapp Basin only underwent passive subsidence without major faulting (Jensen and Sørensen, 1992), as

shown in Clark et al. (2014) with a β -factor of less than 1.5 (Figure 4). This was followed by Early Cretaceous tectonic subsidence along the western margin, which created accommodation space for thick Cretaceous successions in the Harstad, Tromsø, Bjørnøya and Sørvestsnaget basins (Breivik et al., 1998; Faleide et al., 1993). Moreover, during the Early Cretaceous, the northern Barents Sea underwent uplift and extensive magmatism in response to the rifting and eventual sea floor spreading of the Arctic Basin (Corfu et al., 2013; Gjelberg and Steel, 1995; Grogan et al., 2000).

The Upper Jurassic sedimentation in the Nordkapp Basin and in most of the areas in the Barents Shelf consisted of marine fine-grained siliciclastics (Fuglen Formation) overlain by marine organic-rich sediments (Hekkingen Formation) (Henriksen et al., 2011b). As a result of Early Cretaceous uplift, the shelf deposits prograded into the southern parts of the Barents shelf. Based on recent studies by Marin et al. (2017), most of the southwestern part of the Nordkapp Basin was characterized by deep-water depositional environments with deposition of fine siliciclastics (Knurr/Kolmule Fms.) (Marin et al., 2017). Differences in sedimentary thicknesses in the Nordkapp Basin in the Lower Cretaceous, suggests that diapir growth continued either by salt supply from underneath (Koyi et al., 1993, 1995b), or gravity-induced contraction (Nilsen et al., 1995).

2.2.4. Late Cretaceous – Cenozoic

Renewed extension in the Late Cretaceous related to the opening of the Atlantic Ocean (Faleide et al., 2008), reactivated the Nylseppen, Masøy and Thor Iversen fault complexes around the Nordkapp Basin (Gabrielsen et al., 1992; Nilsen et al., 1995). This produced gravitational gliding and consequent squeeze and growth of salt structures (Gabrielsen et al., 1992; Nilsen et al., 1995). The Late Cretaceous and Early Cenozoic evolution of the Barents Sea was mainly concentrated in the western margin. In Cenozoic times, a regional compressional event in the Barents Shelf led to inversion of some of the previous structures and diapir rejuvenation in the Nordkapp Basin (Jensen and Sørensen, 1992; Koyi et al., 1995b; Nilsen et al., 1995). Quaternary strata overlaying unconformably the deformed Cretaceous, indicate that the regional uplift eroded approximately 1300-1500 m of Cenozoic and Mesozoic strata (Baig et al., 2016; Henriksen et al., 2011a; Ohm et al., 2008).

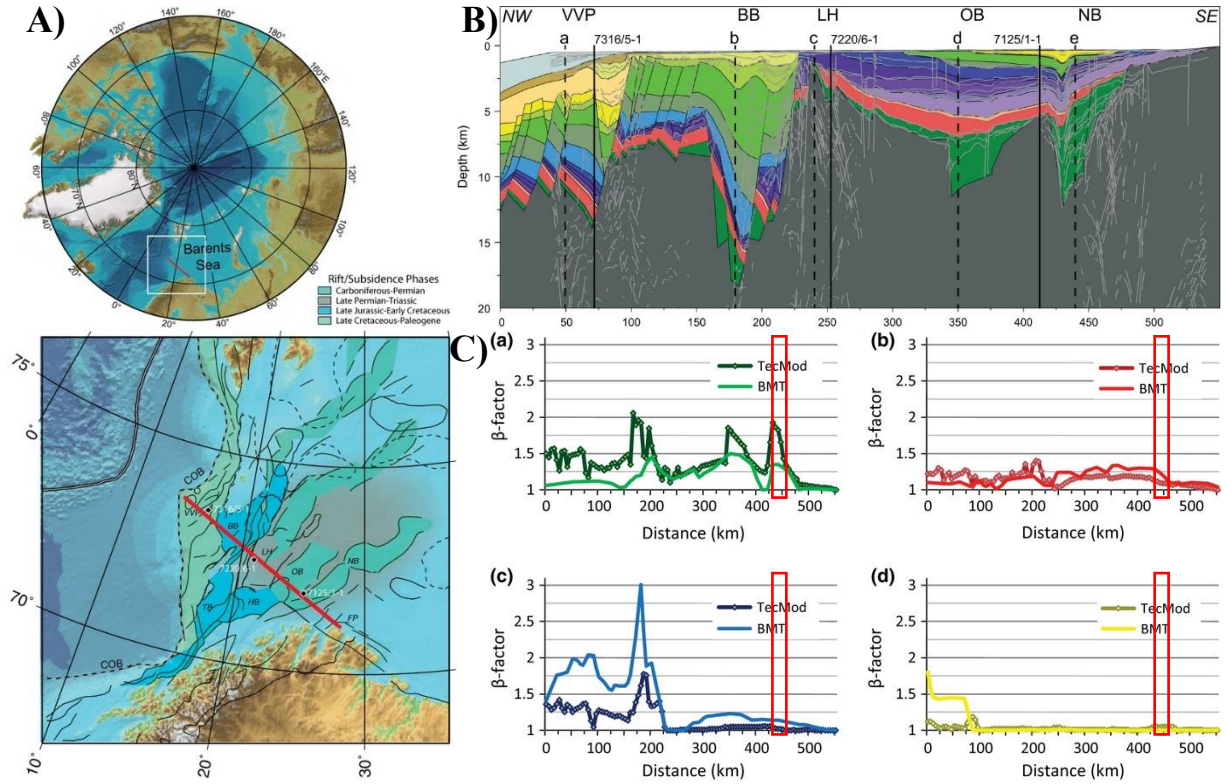


Figure 5 – A) The upper figure illustrates the location of the Barents Sea within the Arctic. The lower figure displays a tectonic basemap of the western Barents Sea area, with bathymetry (Jakobsson et al., 2008) and basin rifting/subsidence phases (Faleide et al., 2008). The figure also illustrates the location of the wells and seismic profile displayed in figure B. B) Interpreted and depth-converted seismic profile by Clark et al., (2014). Vertical exaggeration is 10. VVP, Vestbakken Volcanic Province; BB, Bjørnøya Basin; LH, Loppa High/Selis Ridge; OB, Ottar Basin; NB, Nordkapp Basin. C) Stretching factors for (a) Late Carboniferous rift phase, (b) Late Permian rift phase, (c) Late Jurassic rift phase, (d) Paleocene-Eocene rift phase (Clark et al., 2014). The red rectangles indicate the location of the Nordkapp Basin.

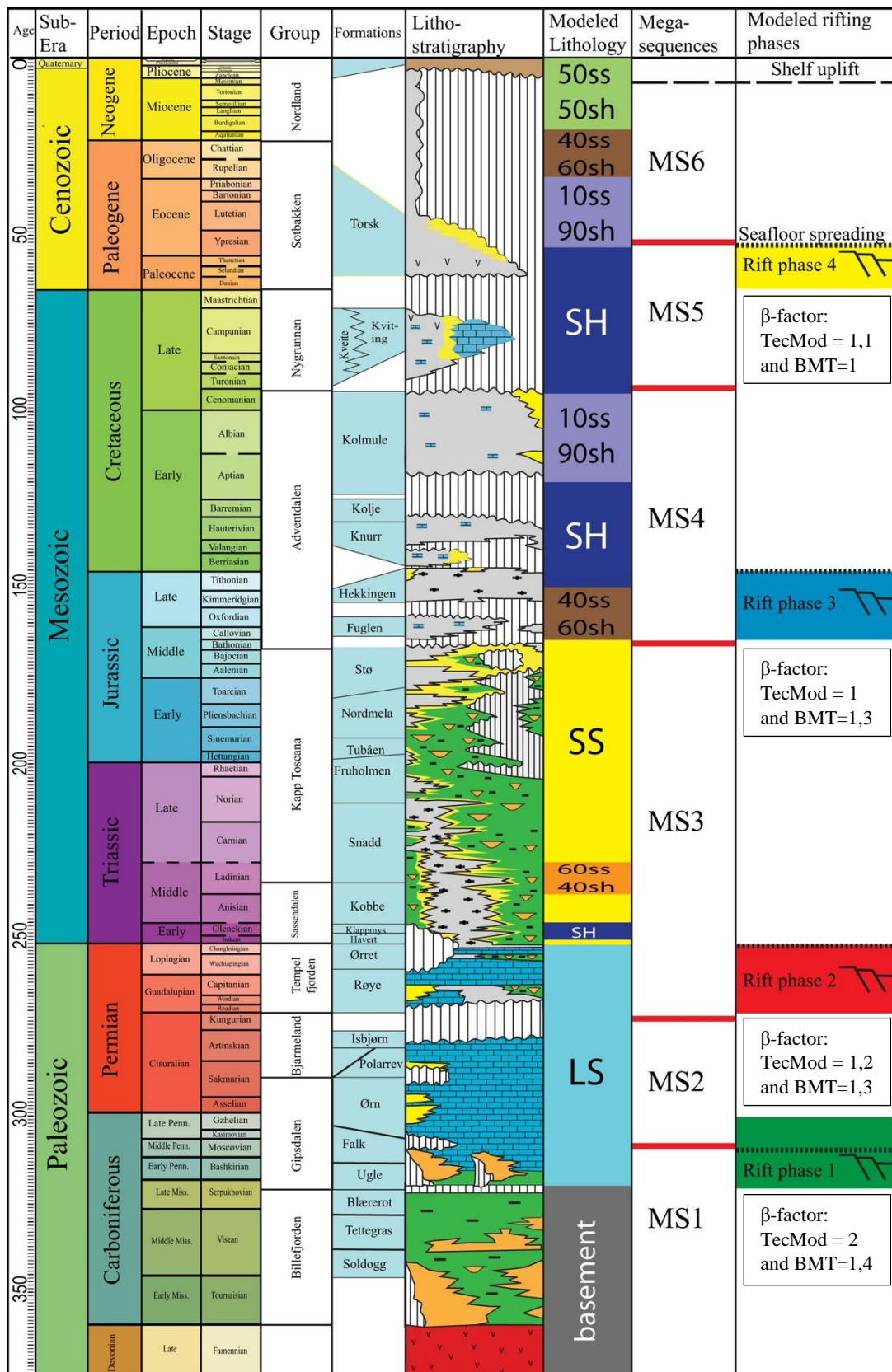


Figure 6 - Lithostratigraphic column for the south-west Barents Sea by Clark et al. (2014). Modelled rift phases shown in right column, spanning the duration of rifting. Dotted black lines show the age of instantaneous rifting assigned in the basin model. Lithostratigraphy key – basement: red; continental sand: orange; continental shales: green; carbonates: blue; marine sand: yellow; marine shale: grey; undifferentiated: brown; missing section: white. Time scale after Gradstein et al. (2004).

3. Dataset

This study utilizes borehole data from two exploration wells (7228/7-1A, -1S and 7228/2-1 S) provided by the Norwegian Petroleum Directorate (NPD) via the DISKOS database, and 2D structural restorations by Rojo et al. (submitted) (Figure 7B). Vitrinite reflectance (VRo) data from the wells were used in order to support heat flow calculations (Figure 7A). The 2D restorations by Rojo et al. (submitted) are the main input for model building, since they illustrate the progressive evolution of salt structures and associated deformation.

A)

Well	Sample Type	AFT no	Lower Depth (in MD RKB)	%Rb	SD	Number of Measurements	Sample Quality
7228/7-1S	DC	11050	520	0.37	0.07	11	P
7228/7-1S	DC	11051	610	0.37	0.07	5	P
7228/7-1S	DC	11052	710	0.32	0.03	3	P
7228/7-1S	DC	11053	810	0.33	0.04	6	P
			alt pop	0.51	0.07	9	
7228/7-1S	DC	11054	910	0.50	0.05	6	P
7228/7-1S	DC	11055	1010	0.52	0.08	9	P
7228/7-1S	DC	11056	1110	0.50	0.05	14	M
7228/7-1S	DC	11057	1210	0.53	0.08	9	P
7228/7-1S	DC	11058	1308	0.45	0.05	6	P
7228/7-1S	DC	11059	1314	0.49	0.04	4	P
7228/7-1A	DC	11032	1347	0.40	0.03	23	M/G
7228/7-1A	DC	11034	1434	0.40	0.04	22	G
7228/7-1A	DC	11035	1566	0.50	0.05	25	G
7228/7-1A	DC	11036	1647	0.45	0.05	24	M/G
7228/7-1A	DC	11038	1755	0.42	0.05	8	P
7228/7-1A	DC	11039	1899	0.50	0.05	8	P
7228/7-1A	DC	11040	1935	0.47	0.05	8	P
7228/7-1A	DC	11041	1977	0.58	0.07	25	G
7228/7-1A	DC	11042	2031	0.57	0.06	29	G
7228/7-1A	DC	11043	2103	0.50	0.04	7	P
7228/7-1A	DC	11044	2229	0.59	0.04	8	P
7228/7-1A	DC	11045	2376	0.55	0.06	26	G
7228/7-1A	COCH	11022	2455 52	0.69	0.05	8	P
7228/7-1A	COCH	11023	2457 34	0.59	0.06	26	G
7228/7-1A	DC	11046	2511	0.63	0.06	23	M
7228/7-1A	DC	11047	2670	0.52	0.01	2	P
			alt pop	0.71	0.04	12	
7228/7-1A	DC	11048	2742	0.65	0.05	3	P
			alt pop	0.81	0.04	14	
7228/7-1A	DC	11049	2781	0.45	0.08	3	P
			alt pop	0.85	0.07	11	
7228/7-1A	COCH	11025	2842 27	0.66	0.05	11	M
7228/7-1A	COCH	11027	2860 28	0.72	0.01	4	M
			alt pop	0.85	0.04	13	

B)

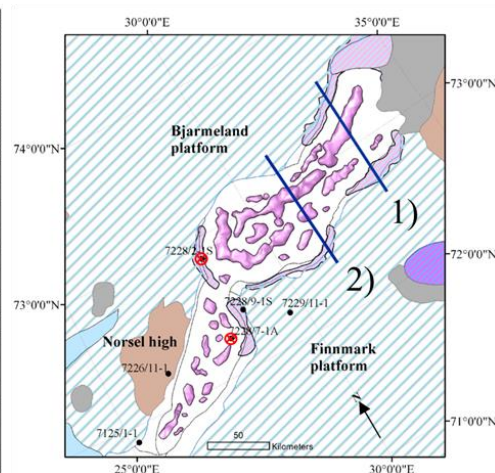


Figure 7 – A) Petroleum Geochemistry Report - NOCS well 7228/7-1A –1S (NPD FactPages, 2018). B) Map showing the position of the provided sections and their relation to the wells (red circles) (Rojo et al., submitted).

4. Methodology

4.1. Burial and thermal history

Understanding heat flow and its variation through time is imperative for the success of petroleum exploration in sedimentary basins. Roughly, half of the heat flow in thermally relaxed sedimentary basins (i.e. older than 60 My) is generated from crystalline basement while the other half derives from the mantle (e.g. Ritter et al. 2004). The heat production from the crystalline basement is caused by decay of long-lived radiogenic isotopes of Thorium, Potassium and Uranium (e.g., (Turcotte and Schubert, 2002). The concentration of these elements shows wide variation within the mainland crystalline basement of Norway (Pascal et al., 2011).

Acidic rocks of the Precambrian gneisses and granites produce more heat than intermediate-mafic rocks from the Caledonian nappes and high-grade metamorphic units (e.g. the Lofoten gneiss complex). These two rock units are representative of the middle and lower crust of the Barents Sea (Pascal et al., 2011). Mafic rocks from underplated bodies provide a transient heat pulse at the time of deposition. Assuming a constant heat production from the continental crust and from the mantle will lead to significant errors with regard to the calculation of the temperature regime in the sedimentary basin; therefore, this work uses variable/transient heat flow values through time.

Vitrinite Reflectance (VRo) is the most widely used maturity indicator in geohistory modeling calibrations (Li et al., 2010) and one of the main indicators of thermal maturity (Cardott, 2012). Two sets of VRo values from the wells 7228/7-1A and 7228/2-1S (Figure 7B) were used as maturity indicators to calibrate the model. The analysis of these data is a fundamental step to determine the input heat flow and thermal gradients, as well as to establish a link between the tectonic events of the Nordkapp Basin and its heat flow history.

	Thickness (km)	Thermal Conductivity (W/m/K)	Heat Production (microW/m3)	Density (kg/m3)	Heat Capacity (J/kg/K)
Upper Crust:	25	3.5	1.5	2670	900
Lower Crust:	17	3.1	0	2850	1050
Mantle Lid:	88	2.5	0	3300	1200

Heat production depth decay (km)

Crust/Sub crust stretch ratio (0=no crust stretching, 1=uniform stretching)

Depth to basement m

Radiogenic heat from lithosphere = 18.25 mW/m2 (0.44 HFU)

OK Cancel

Figure 8 - Crust and Lithosphere Properties entered to the software Genesis. This together with the VRo data, the burial history of the pseudowell, and the stretch factors from Clark et al. (2014), allowed the software to estimate the basin's heat flow through time.

Since the basin is considerably deep (~8km) the total radiogenic heat production cannot be neglected (Hu et al., 2001). The radiogenic heat production in the Barents Sea crust is about $1.5 \mu\text{W}/\text{m}^3$ (Hokstad et al., 2017). In addition, mantle heat flow in the Barents Sea is about $18 \text{ mW}/\text{m}^2$ (Jaupart and Mareschal, 2015). These values, including Pascal et al. (2011) crust and mantle density values provide the basis for estimating the present day thermal conditions.

In an attempt to reproduce the basins thermal history, a pseudo-well was created in the eastern minibasin (section 1 of this study, Figure 7B). The burial history of this well was reconstructed from backstripping taking into account paleo-sea-level, water depth, unconformities, missing sediment thickness, the compaction properties of sediments, and the compaction of each layer through time.

The present day radiogenic heat production, mantle heat flow, crust and mantle density data by Pascal et al. (2011), the VRo data from the two exploration wells, the burial history of the pseudowell, and the stretching factors from Clark et al. (2014) were all integrated in the software Genesis (Figure 8). This was necessary to attain the heat flow history of the basin at the pseudowell location. The heat flow results of this simulation are part of the boundary conditions for the thermal model.

4.2. Model Building

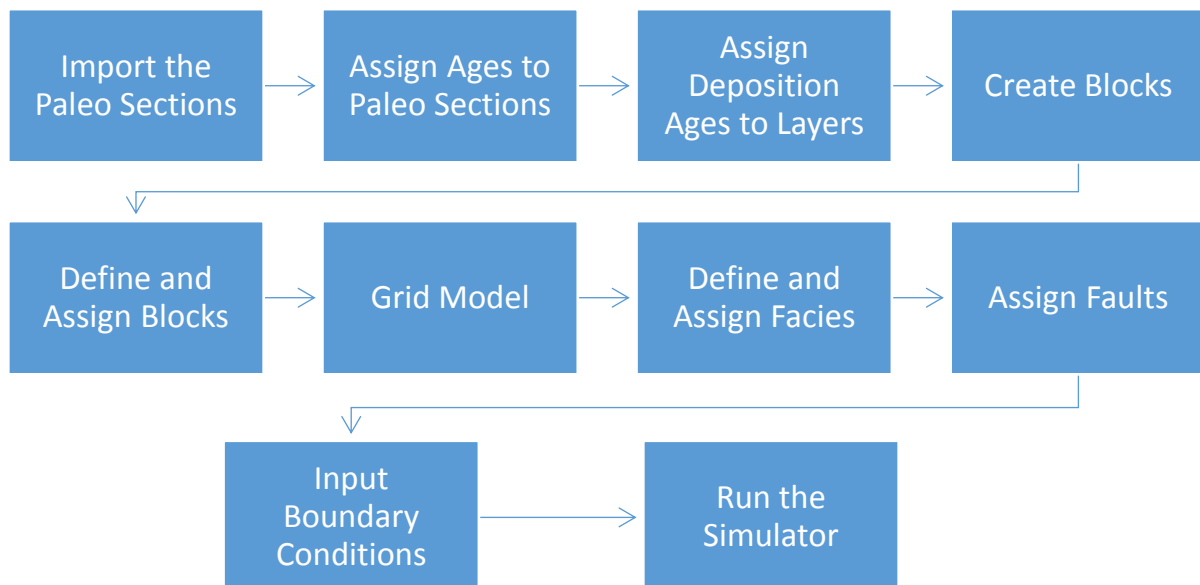


Figure 9 - 2D TecLink workflow

Thermal modeling was performed using the TecLink 2D module of PetroMod, which links structural modeling with petroleum systems modeling by enabling users to integrate the reconstructed paleo-sections into 2D models, using the workflow illustrated in Figure 9. In standard models, paleo geometries are created by incorporating depositional/erosional ages followed by calculating the compaction of layers. TecLink models, on the other hand, are based on the paleo-stepping approach (PetroMod TecLink 2D reference guide). The basin's geometry through time is provided by the reconstructions in Rojo et al. (submitted) reconstructions, which were performed in the software Move. The two sections included in this study (Figure 7B) consist of seven restoration steps (Table 1): 1. Early Permian, 2. Late Permian, 3. Lower and Middle Triassic, 4. Late Triassic, 5. Late Jurassic, 6. Lower Cretaceous, and 7. Present day.

When building the model, each restoration step was compartmentalized in several blocks or polygons, each of them associated with their respective lithological properties. In order to complete the model, these property blocks were then assigned to their respective layers (Figure 10).

Table 1 - Assigned Ages of Paleo Sections

Paleo Section	Age (Ma)
7stp	0
6stp	100
5stp	152
4stp	208
3stp	220
2stp	250
1stp	290

The thermal modeling delivers the evolution of temperature, heat flow and maturation ratio for the source rock intervals in the basin. Based on these results, this study evaluates the ideal time-temperature window for hydrocarbon preservation in reservoirs (Nadeau et al., 2005), and the relationship with maturation of source rock units (Templefjorden Group, Havert Formation and Hekkingen Formation) in order to develop a better understanding of the petroleum system in the Nordkapp Basin. Since the Triassic source rock potential (Havert Formation) is not completely clear, different source intervals at different depths within the Triassic were assumed to explore the response of these intervals to the modelled temperature evolution.

Age [Ma]	Horizon	-	Layer	-	Event Type	No. of Sublayers	Max. Time Step [Ma]
0.00	Horizon_1						
			Layer_1		Erosion		20.00
70.00	Horizon_2						
			Layer_2		Deposition	1	60.00
80.00	Horizon_3						
			Layer_3		Deposition	1	20.00
150.00	Horizon_4						
			Layer_4		Deposition	1	52.00
210.00	Horizon_5						
			Layer_5		Deposition	1	49.00
242.00	Horizon_6						
			Layer_6		Deposition	1	7.00
248.00	Horizon_7						
			Layer_7		Deposition	1	12.00
252.00	Horizon_8						
			Layer_8		Deposition	1	32.00
254.00	Horizon_9						
			Layer_9		Deposition	1	38.00
290.00	Horizon_10						
			Layer_10		Deposition	1	69.00
359.00	Horizon_11						

Name	Color	Parent Block	Block Order	
Basement			1	Layer 10
Salt1		Basement	4	Layer 9
Salt		Basement	5	
Templ		Basement	9	
Templ_1		Salt	10	Layer 8
Templ_2		Salt	11	
Templ_3		Salt	12	
Hav_1		Templ_1	15	
Hav_2		Templ_2	16	Layer 7
Hav_3		Templ_3	17	
Kobbe_1		Hav_1	20	
Kobbe_2		Hav_2	21	Layer 6
Kobbe_3		Hav_3	22	
Snadd_1		Kobbe_1	25	
Snadd_2		Kobbe_2	26	Layer 5
Snadd_3		Kobbe_3	27	
Hekk_1		Snadd_1	30	
Hekk_2		Snadd_2	31	Layer 4
Hekk_3		Snadd_3	32	
UK_1		Hekk_1	35	
UK_2		Hekk_2	36	Layer 2
UK_3		Hekk_3	37	

Figure 10 - On the left: Age to layer assignment; On the right: Block definition associated to their respective layers

4.3. Structural Restorations

This study uses two restored sections in the Nordkapp Basin from Rojo et al. (submitted). Both sections are depth-converted and located in the eastern minibasin and central minibasin (Figure 7B). The restorations are kinematic: Cenozoic strata was reconstructed based on Ohm et al. (2008) and restored using flexural slip. Pre-kinematic units were also restored with flexural slip, while syn-kinematic units were restored using vertical shear. Flexural compensation of the loads was assumed, using an elastic thickness T_e of 20 km (Gac et al., 2016).

5. Input

5.1. Boundary conditions

Boundary conditions such as paleo-water depth (PWD), sediment-water interface temperature (SWIT), and heat flow (HF) through time should be entered to the thermal model. The structural restorations provide the PWD values. Moreover, the AutoSWIT feature in PetroMod, delivered SWIT values based on global mean temperature at sea level (Wygrala, 1989). Figure 13 shows PWD and SWIT through time.

Combined VRo data from the two wells and backstripping of the pseudowell in the eastern minibasin were used to estimate the heat flow values (Figure 11). It is important to

notice that there are two main trends in the VRo profile. The first trend is above 3500 m of depth and the second below (Figure 11). The higher slope of the first trend indicates a more recent maturation trend, since it has values until the surface displaying no significant alteration of its trend. This shallower VRo trend was used to estimate the present-day heat flow, which is around 40 mW/m² (Figure 12A).

On the other hand, a lower slope for the deeper second trend suggests a higher heat influx (Figure 12B). VRo is susceptible to thermal alteration; therefore, it could be argued that higher heat flows may come from tectonic events or magmatic intrusions. However, to the best of our knowledge, there are no major igneous intrusions in the Nordkapp Basin. Thus, it is possible to rule out magmatic intrusions as the source of the increased heat, and instead relate the deeper VRo trend to a tectonic event. Therefore, it is assumed that the second trend is a thermal consequence of the Late Jurassic rifting event. The Genesis rift model and the deeper VRo trend combined give an approximate heat flow value of 45 mW/m² for this event (Figure 12B).

For the Late Permian rifting event, and the first rifting event in the Late Carboniferous, the calibrated Genesis rift model with their corresponding stretching factors (Table 2), delivers heat flow values of 53 mW/m² (Figure 12C) and 77 mW/m² (Figure 12D), respectively with a considerable level of uncertainty. These values are used in thermal model. Figure 13 (bottom) and Table 2 summarize the heat flow and rifting events through time.

Table 2 - Major events associated with β -factors and estimated heat flow.

Age	Heat flow (mW/m ²)	β -Factor
Late Carboniferous rifting (315-298)	~77	1,5 - 2
Late Permian rifting (270-251)	~53	1,1 - 1,6
Late Jurassic to Early Cretaceous rifting (148-135)	~45	1,25
Today	~40	-

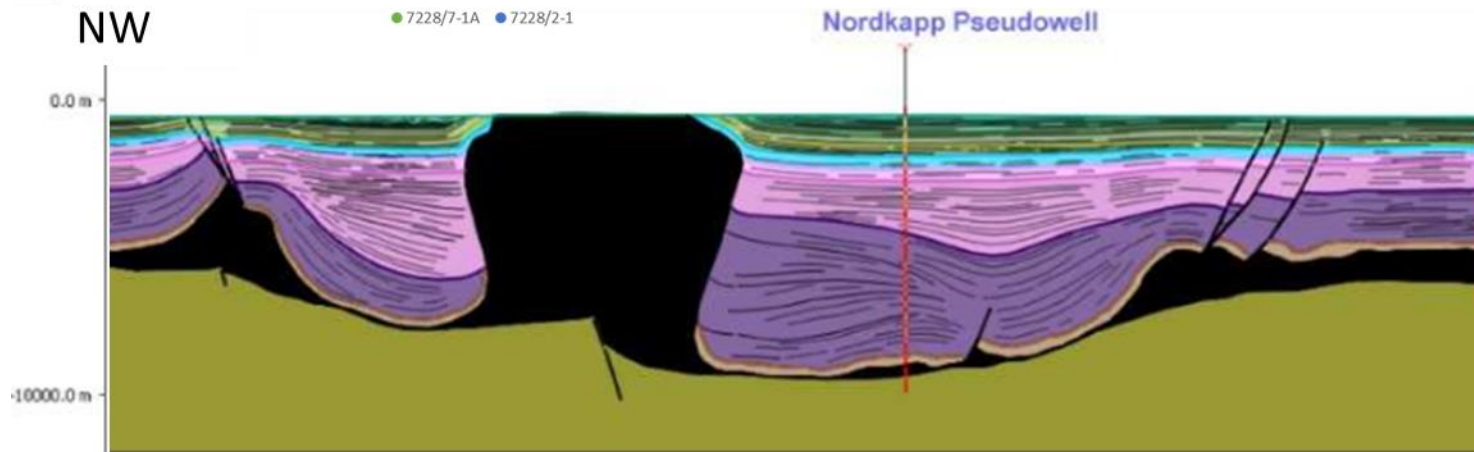
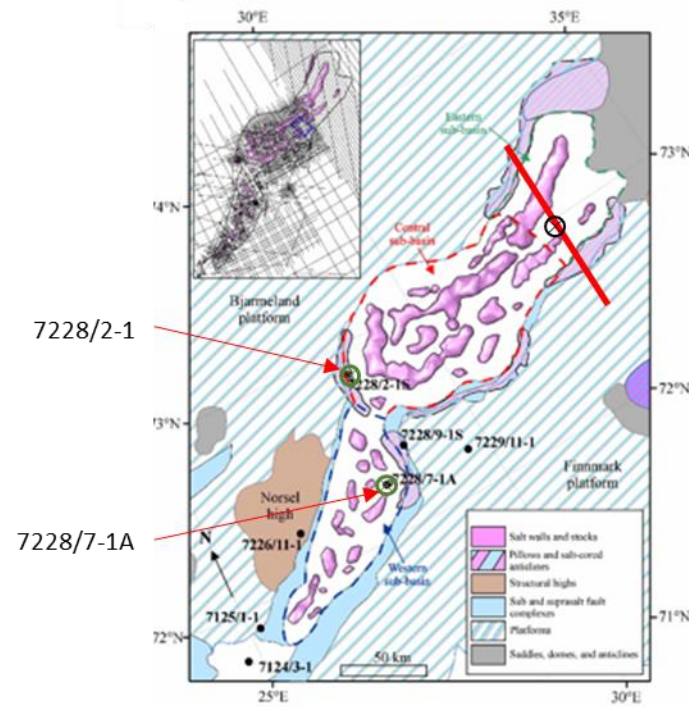
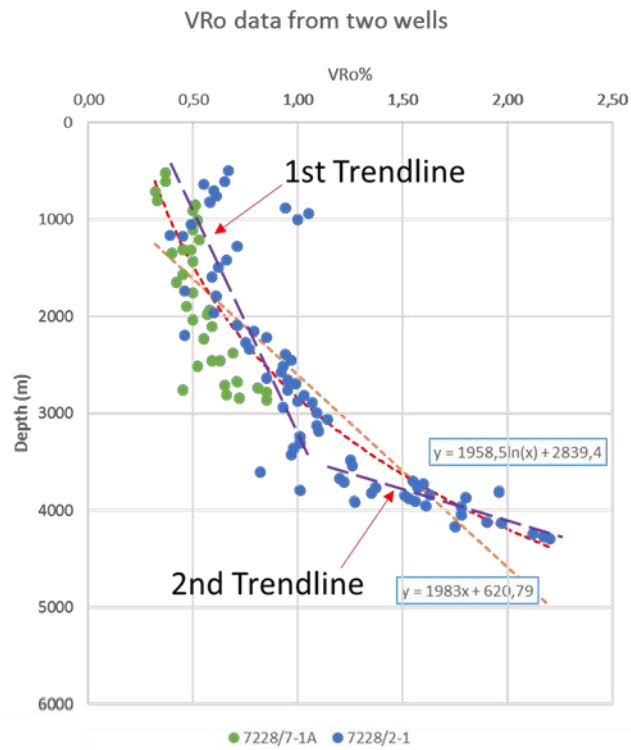


Figure 11 - Bottom: pseudo-well position in the eastern minibasin. Top Left: Vitrinite Reflectance data from the selected two wells: logarithmic fit in red, average fit in orange, and the two linear fits used for calibration in the model in purple. Top right: Map showing the position of the section and the pseudo-well (black) and the wells with vitrinite data (green). Bottom: Cross section with pseudowell.

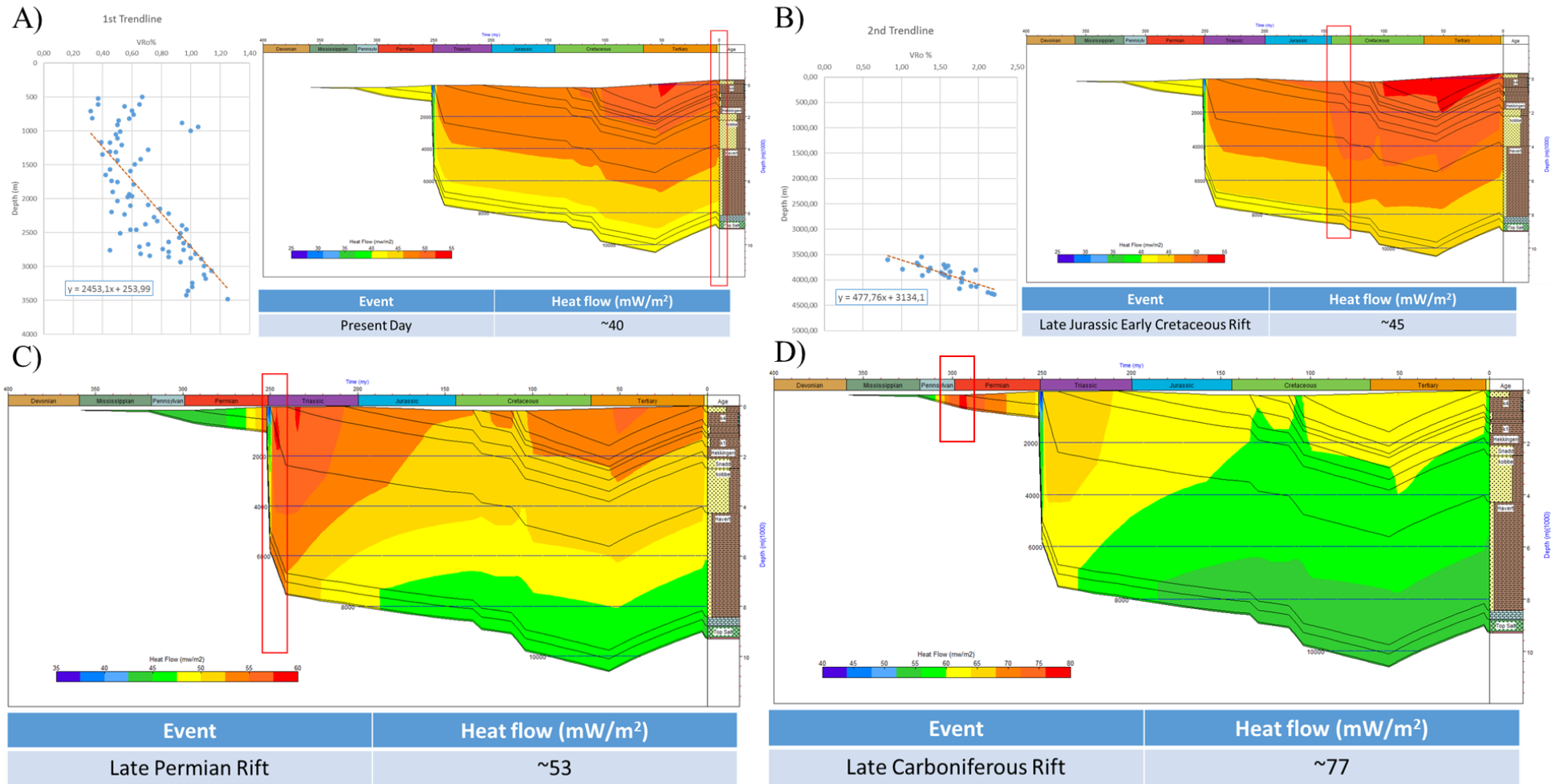


Figure 12 - Genesis model at the location of the pseudowell. A) On the left: VRo data showing the 1st trendline of combine VRo data from the wells; On the right: Present day burial history (red rectangle) and respective heat flow value. B) On the left: VRo data showing the 2nd trendline corresponding to the last major rift event; On the right: Last rift related burial history showing the estimated heat flow value in the red rectangle. C) Late Permian rift phase showing estimated heat flow value in the red rectangle area. D) Late Carboniferous rift phase showing estimated heat flow value in the red rectangle.

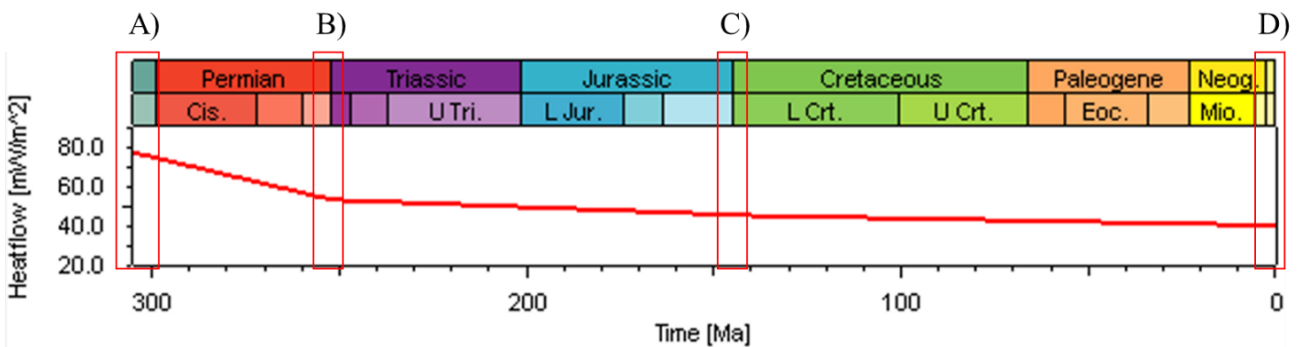
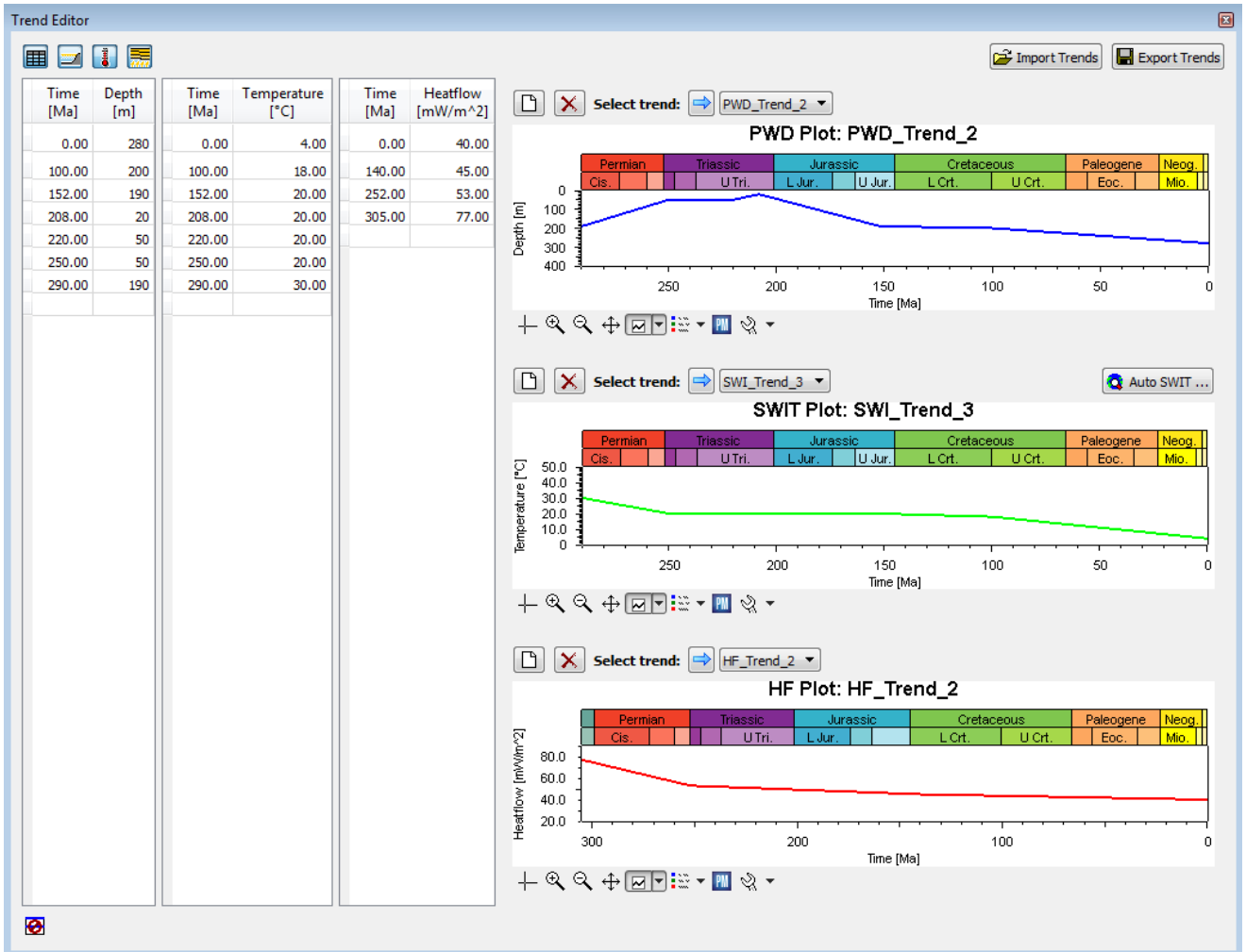


Figure 13 – Boundary conditions of the thermal model. Top: Paleowater depth (PWD), sediment water interface temperature (SWIT) and heat flow (HF) through time. Bottom: Zoom in of heat flow trend plot showing the times at which the heat flow was introduced in the model (red rectangles): A) Late Carboniferous rift; B) Late Permian rift; C) Late Jurassic rift; D) Present day.

5.2. Kerogen Maturation

The kerogen maturation models used in this study are based on first-order kinetics applicable to decomposition reactions (Behar et al., 1997). The three representative source rocks of the Nordkapp Basin are the limestones of the Templefjorden Group, shales from the Havert Formation, and shales from the Hekkingen Formation. According to Stemmerik et al. (1999), Stemmerik and Worsley (2005) and Henriksen et al. (2011b), these source rocks are type 2 kerogen (marine). Therefore, the Behar et al. (1997) type 2 (PB) kinetics is entered in the model (Figure 14). The input source rocks TOC and HI values represent the average values of each formation from Ohm et al. (2008) source rock characteristics diagram.

























Name	Color	Lithology Value	Kinetics	TOC Mode	TOC Value [%]	TOC Map	HI Mode	HI Value [mgHC/gTOC]	HI Map	Petroleum System Elements
Layer_2_Facies		Sandstone (clay rich)								Overburden Rock
Layer_4_Facies		Shale (typical)	Behar_et_al(1997)_TII(PB)	Value	7.00		Value	300.00		Source Rock
Layer_5_Facies		Sandstone (typical)								Overburden Rock
Layer_6_Facies		Sandstone (clay rich)								Reservoir Rock
Layer_7_Facies		Shale (typical)	Behar_et_al(1997)_TII(PB)	Value	1.20		Value	333.00		Source Rock
Layer_8_Facies		Limestone (shaly)	Behar_et_al(1997)_TII(PB)	Value	2.10		Value	206.00		Source Rock
Layer_9_Facies		Salt								Seal Rock
Layer_10_Facies		Gneiss								none

Figure 14 - Facies definition. Association of the main source rocks with respective kinetics, TOC and HI values from Peters et al. (2005).

The sandstones from the Kobbe and Snadd Formations were input as reservoir rocks considering their petrophysical properties (Figure 14). Salt was assumed to be the seal rock, and the remaining units, the overburden.

5.3. Structural Restorations

Figure 15 shows the structural restorations of the two sections provided by Luis Rojo. Section 1 is located in the eastern minibasin, and section 2 in the central minibasin. The pre-kinematic seismic units (SU1 to SU7) and eight key horizons are included in each section. SU1 corresponds to Top Gipsdalen Group (Salt layer), SU2 to Top Templefjorden Group SU3 to Top Havert Formation, SU4 to Top Kobbe Formation, SU5 to Top Snadd Formation, SU6 to Top Hekkingen Formation, and SU7 to Upper Cretaceous-Cenozoic (Rojo et al., submitted). As mentioned before, Figure 15 is the geometrical framework for constructing the “units blocks” in the thermal model.

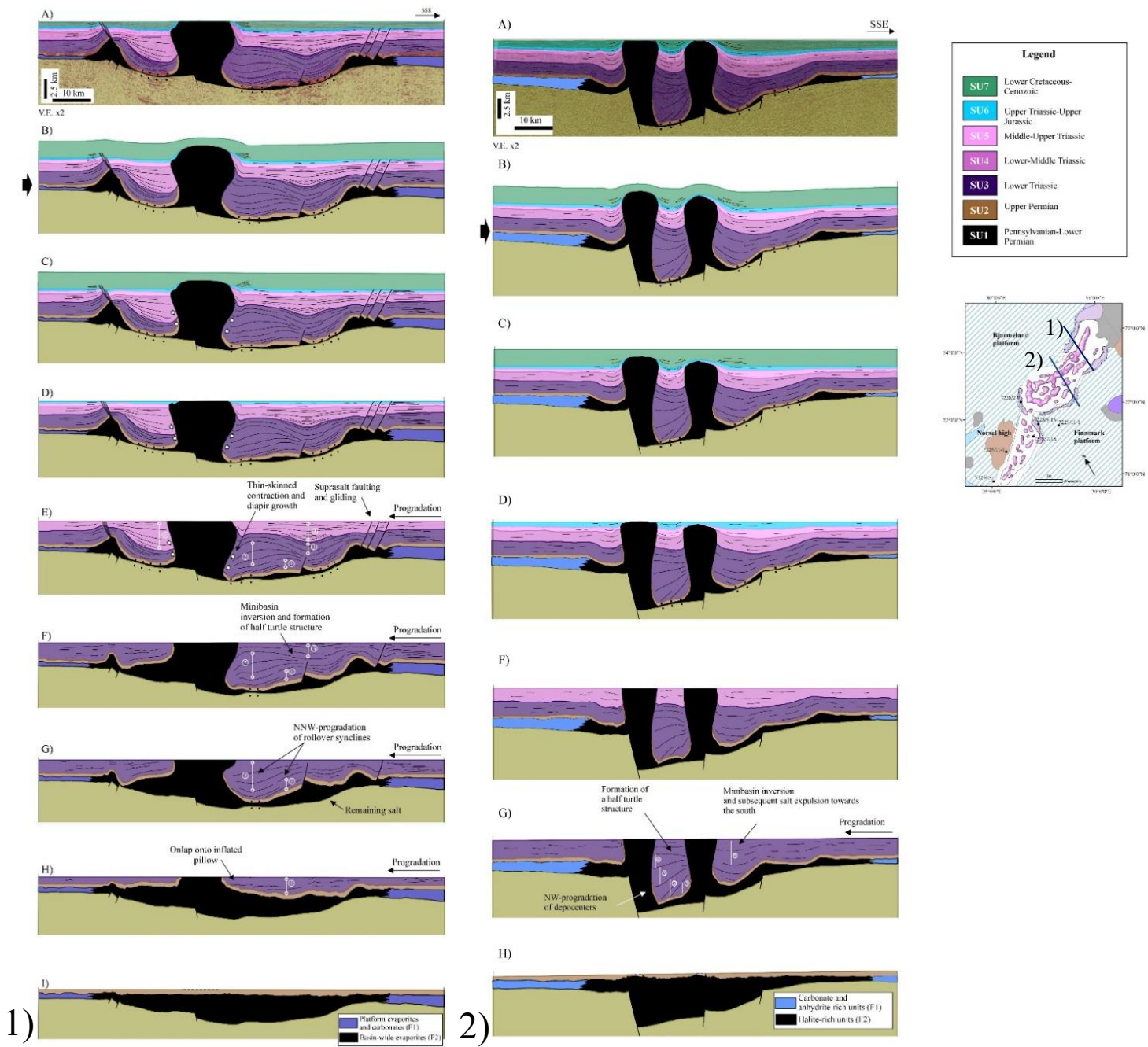


Figure 15 - Sequential structural restorations of two sections, one across the eastern minibasin (section 1), and the other across the eastern central minibasin (section 2). From Rojo et al. (submitted). Inset map shows the lines of the sections.

6. Results

This chapter provides the results for the thermal modelling of the two restored sections (Figure 15). The results are grouped into four categories: (1) lithology and structural evolution, (2) temperature evolution, (3) reservoir temperature, and (4) source rock maturation.

Lithology evolution is one of the main parameters for understanding the thermal evolution of the basin. It takes into account the evolution of porosity, permeability, thermal conductivity, thickness and compaction through time. For a correct assessment of these parameters, structural evolution is key. It is important to notice that the shape of the diapirs in the provided restorations was slightly altered in the thermal model, because the thermal modelling software could not accommodate diapir overhangs. This is a limitation of the software and it will be further touched upon in the discussion.

Temperature evolution involves thermal conductivity contrasts between the salt and the surrounding overburden, which are significantly illustrated in the models. As previously mentioned, the impact distance of the thermal anomalies is around two to three times the diapir radius (O'Brien and Lerche, 1988). This anomaly increases exponentially towards the center of the salt diapir.

Reservoir temperature displays the temperature in the units thought to have reservoir properties, which in the Nordkapp Basin are the Kobbe and Snadd Formations. Upper Cretaceous/Cenozoic units can also be considered as reservoirs.

Source rock maturation evaluates the impact of thermal changes on the maturity of organic material in the surrounding sediments. The VRo model developed by Sweeney and Burnham (1990) is used for estimating the maturation. The maximum permitted value of vitrinite reflectance is 5%, which is adequate for sedimentary basins. It is beyond the upper limit of thermogenic gas generation (Escalona et al., 2011), and thus beyond the interest of this study. The main source rocks are the Templefjorden Group limestones, Havert Formation shales, and Hekkingen Formation shales. The Havert Formation is a mix of sandstones and shales with a thickness of 2 km. Therefore, it was divided in three different sublayers (lower, mid and upper Havert Formation) in order to better explore the response of this interval to the modelled temperature evolution.

6.1. Section 1

6.1.1. Lithology and structural evolution

After the Late Carboniferous rifting, a sag-basin was formed, allowing deposition of significant amounts of salt in the main depocenters. This event was followed by the deposition of the Late Permian limestones (step 1; Figure 16). Significant amounts of Lower Triassic sediments load the basin and induced halokinesis soon after the Late Permian rifting (step 2; Figure 16). This deposition was triggered by NW prograding sediments, and it stopped in the end of Lower Triassic (step 3; Figure 16). The porosity of the Upper Permian limestone started to drop because of the thick Lower Triassic unit above. Overall, porosity gradually decreased with further deposition of younger units (Figure 32 in Appendix). Continuous loading of the LES (layered evaporite sequences) by the Havert Formation siliciclastics generated a series of NNW-prograding, sigmoidal depocenters interpreted by Rojo et al (submitted) as rollover synclines (step 3; Figure 16). During deposition of the sandstones of the Kobbe Formation, the main depocenter shifted to the NW minibasin since most of the salt was evacuated in the SE minibasin (step 4; Figure 16). Despite complete salt depletion by the end of Late Triassic, salt structures continued growing during the deposition of Jurassic and Cretaceous units (steps 5 and 6; Figure 16).

6.1.2. Temperature evolution

Gradual thermal increase from steps 1 to 2 occurred due to Late Carboniferous rifting showing high geothermal gradient, due to the high heat flow values estimated during this rifting event (Figure 17). However, salt deposition affected the geothermal gradient soon after this event (step 1; Figure 17). Diapir growth significantly reduced the temperature of the surrounding units throughout the basins evolution (step 2 and onwards, Figure 17; Figure 33 in Appendix). Not only the main diapir had influence, but also the northern fault-related salt wedge induced a positive thermal anomaly, which increased the temperature of the overlain units (steps 3 to 7; Figure 17). Following the Late Permian rifting, roughly 2km of siliciclastic strata from the Havert Formation deposited, which led to a rapid increase of the temperature in the SE minibasin, from $\sim 120^{\circ}\text{C}$ to $\sim 200^{\circ}\text{C}$ (step 3; Figure 17), although also decreasing the influx of heat flow from the basement. The temperature remained relatively steady from steps 3 to 6, with the SE minibasin reaching temperatures of around 210°C , and the NW minibasin reaching temperatures of 180°C (Figure 17). After the tectonic inversion (step 7; Figure 17), the temperature decreased in the NW and SE minibasins to around 150°C and 180°C , respectively (Figure 17), also due to low heat flow values.

6.1.3. Reservoir temperature evolution

The Kobbe and Snadd Formations are the oldest reservoir units present, although the Havert Formation can also have potential reservoir units (mix of shale and sandstone). After the deposition of these sediments in the Late Triassic, the temperatures reached more than 90°C in the NW and SE minibasins (step 4; Figure 19). The temperature in the reservoirs gradually increased and stabilized (steps 5, 6; Figure 19), where minibasins reached maximum temperatures of around 120°C. Late Jurassic rifting did not have a significant impact in the thermal evolution of the reservoir rocks (step 6; Figure 19). Present day reservoir rock temperatures dropped considerably after inversion, leaving the highest temperatures in the minibasins at around ~90°C (Figure 18A) to ~60°C (Figure 18B) (step 7; Figure 19).

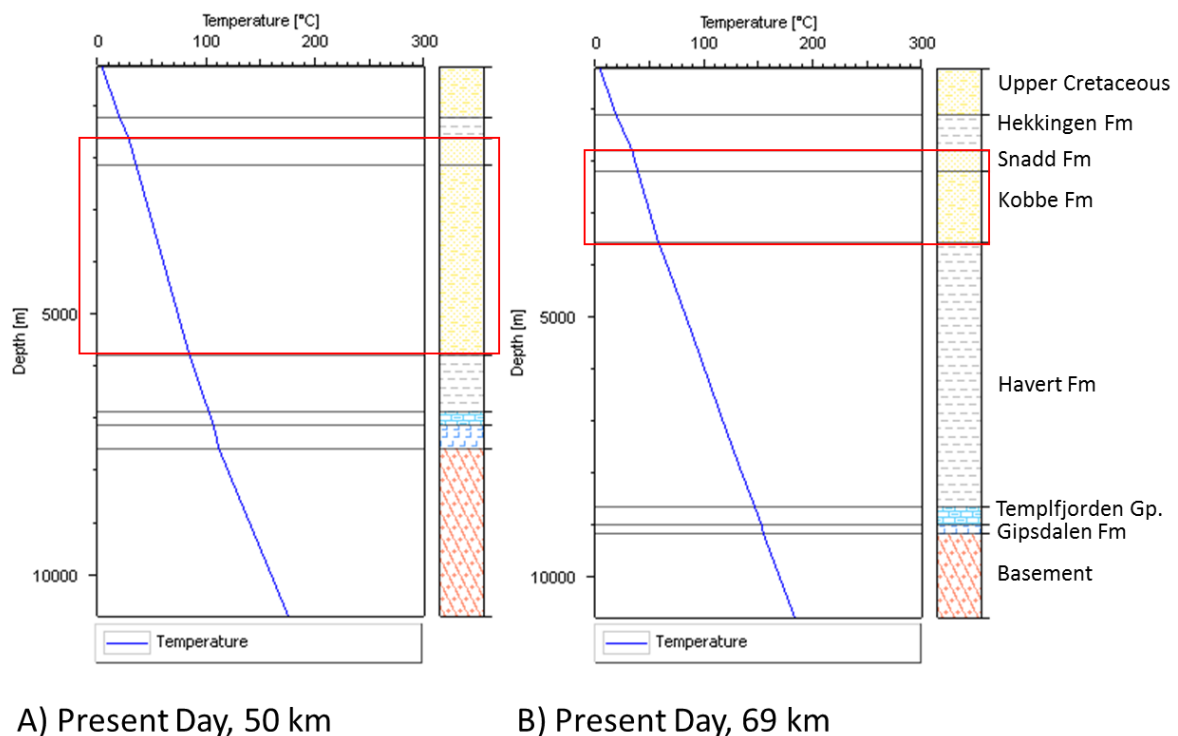


Figure 18 - Present day temperature from two pseudo-wells to the N (A) and S (B) of the main salt structure in section I. Present day reservoir rock temperatures are shown by the red rectangles. Location of the wells is shown in Figure 29 I.

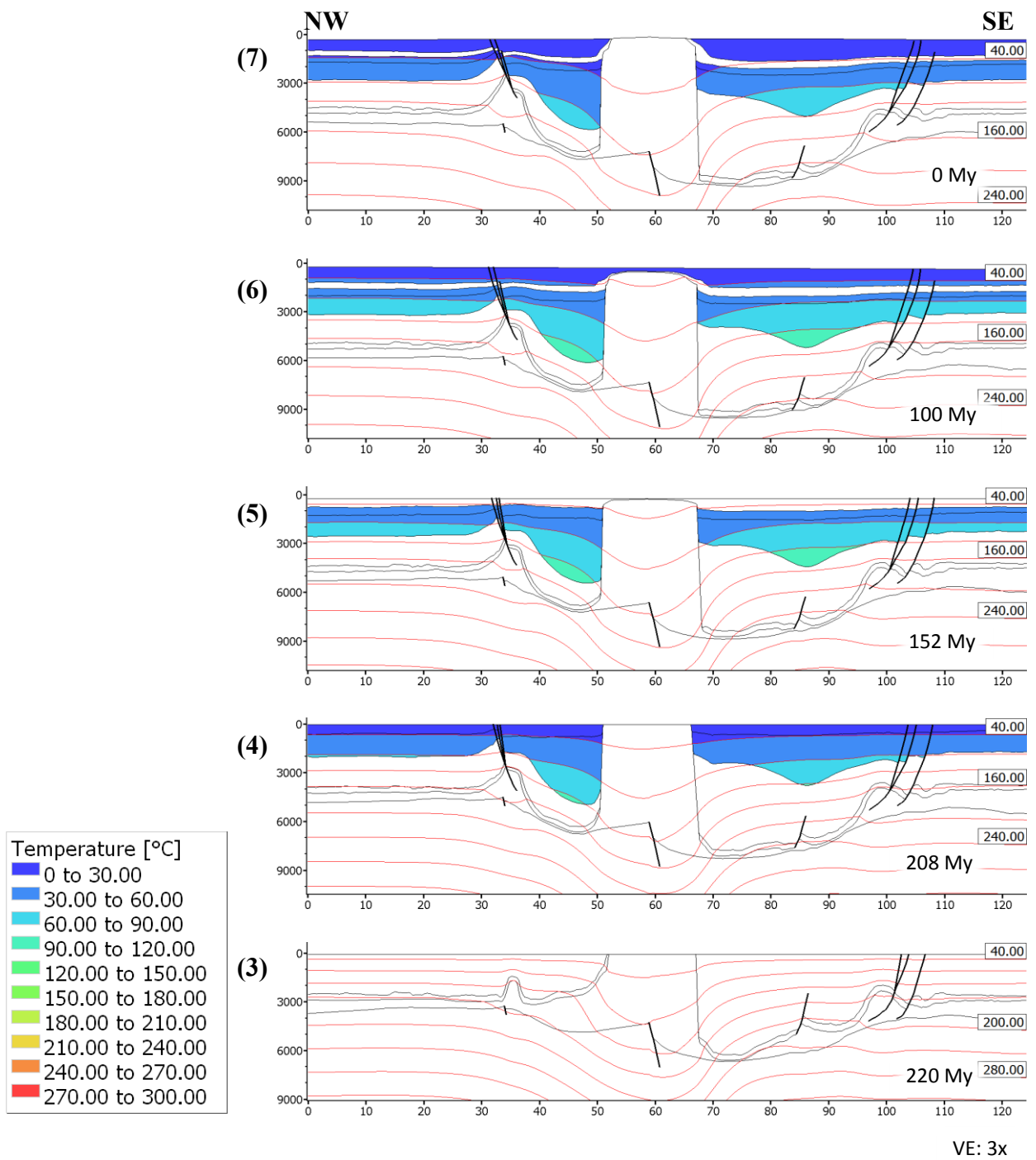


Figure 19 - Reservoir temperature evolution in section I.

6.1.4. Maturation of source rocks

Source rock maturation started along the flanks of the growing salt diapir after the Late Permian rifting (step 2, Figure 20) with a maturation ratio between 0 to 0.55% by 250 My. Away from the salt diapir, maturation reached higher levels of 0.55 to 1%, indicating early oil to main oil stages for the Lower Triassic interval. Following the Early Triassic, the Templefjorden Group in the SE minibasin reached a maturation ratio between 1.3 to 4%, indicating wet to dry gas stages by 220 My (step 3; Figure 20). The Lower and Mid Havert Formation show ratios between 0.7% (Mid Havert Formation) and less than 4% (Lower Havert Formation). On the northern area, the source rocks hardly show alteration of maturity values from the previous step (step 3; Figure 20).

Continuous loading of the Triassic units allowed the NW minibasin to reach higher maturity values by 208 My (step 4; Figure 20). The Lower Havert Formation and Templefjorden Group reached values between 1 to more than 1.3%, indicating late oil to wet gas early stages. The Upper and Mid Havert Formations show maturation values from 0.55 to 1%, representing early to main oil stages (step 4; Figure 20). Around the same time, the maturation values of the source rocks slightly increased in the SE minibasin (step 3 to 4; Figure 20).

The maturation values increased gradually in the source rocks until 100 My (steps 4 to 6; Figure 20). However, along the diapir flank, maturation indicates lower values because of the salt thermal impact (step 2 to 6; Figure 20 and Figure 34 in Appendix). In these flanks, source rock maturation values hardly reach wet gas stages throughout the basins evolution (Figure 20 and Figure 34 in Appendix). After tectonic inversion at about 65 My, maturation barely increased (step 7; Figure 20), mostly due to low heat flow during this period.

Today, in the NW minibasins diapir flank, the source rocks between Upper Havert Formation and Templefjorden range from more than 0.55 to 1% Ro, indicating early to main oil (step 7; Figure 20). The SE minibasin shows low maturation values along the diapir flank, demonstrating immaturity values in the Upper Havert Formation; early oil stages in the Mid Havert Formation; and main oil to wet gas stages in the Lower Havert and Templefjorden source rocks (step 7; Figure 20). Away from the diapir flank, present day model shows the Upper Havert Formation reaching late oil stages; the Mid Havert Formation dry gas stages; and the Lower Havert and Templefjorden source rocks show dry gas to overmature values (step 7; Figure 20 and Figure 34 in Appendix). The shallowest Hekkingen Formation source rocks never reached early oil stages (steps 5 to 7; Figure 20).

Source rocks:
 a) Hekkingen Fm.
 b) Upper Havert Fm.
 c) Mid Havert Fm.
 d) Lower Havert Fm.
 e) Templefjorden Gp.

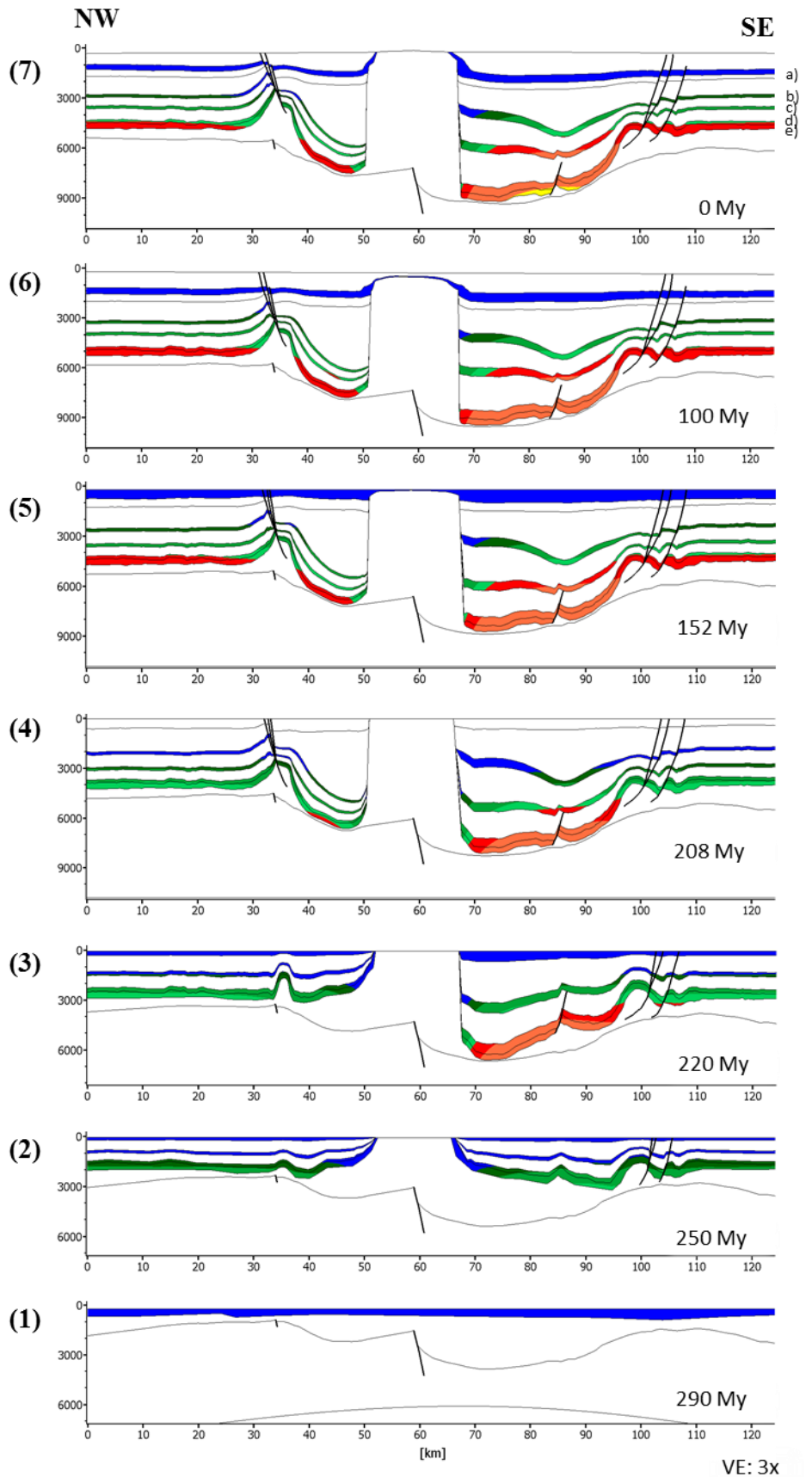
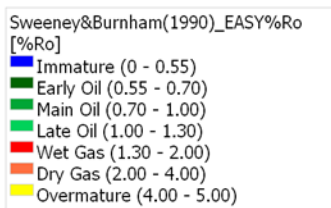


Figure 20 – Evolution of source rock maturation in section 1

6.2. Section 2

6.2.1. Lithology and structural evolution

After the initial stage (step 1; Figure 21), salt movement started first at the basin axis, causing NW migration of depocenters and leaving a significant amount of salt in the southeastern area (step 2; Figure 21). Following the Late Permian rifting, the shales and sandstones of the Havert Formation began depositing in the main depocenters (step 2; Figure 21). A central minibasin was created soon after the two salt diapirs began piercing through the overburden (step 2; Figure 21). Triassic sedimentation increased loading and the remaining salt was evacuated, causing minibasin inversion and half turtle structures (step 4; Figure 21). Salt growth resulted in truncation of the Templefjorden Group limestones by the Kobbe Formation in the NW minibasin (steps 3 to 7; Figure 21). Late Cretaceous/Cenozoic NW progradation of the Kobbe Formation siliciclastics continued, depositing thicker units in the SE (steps 4 to 6; Figure 21). NW sedimentary progradation and halokinesis induced significant sinking of the central and SE minibasins, with siliciclastic units reaching 9 km of depth today (Figure 21). Porosity values of the sedimentary units decreased through time with increasing loading (Figure 35 in Appendix). After tectonic inversion (65 My), erosional events allowed the diapirs to reach the surface (step 7; Figure 21).

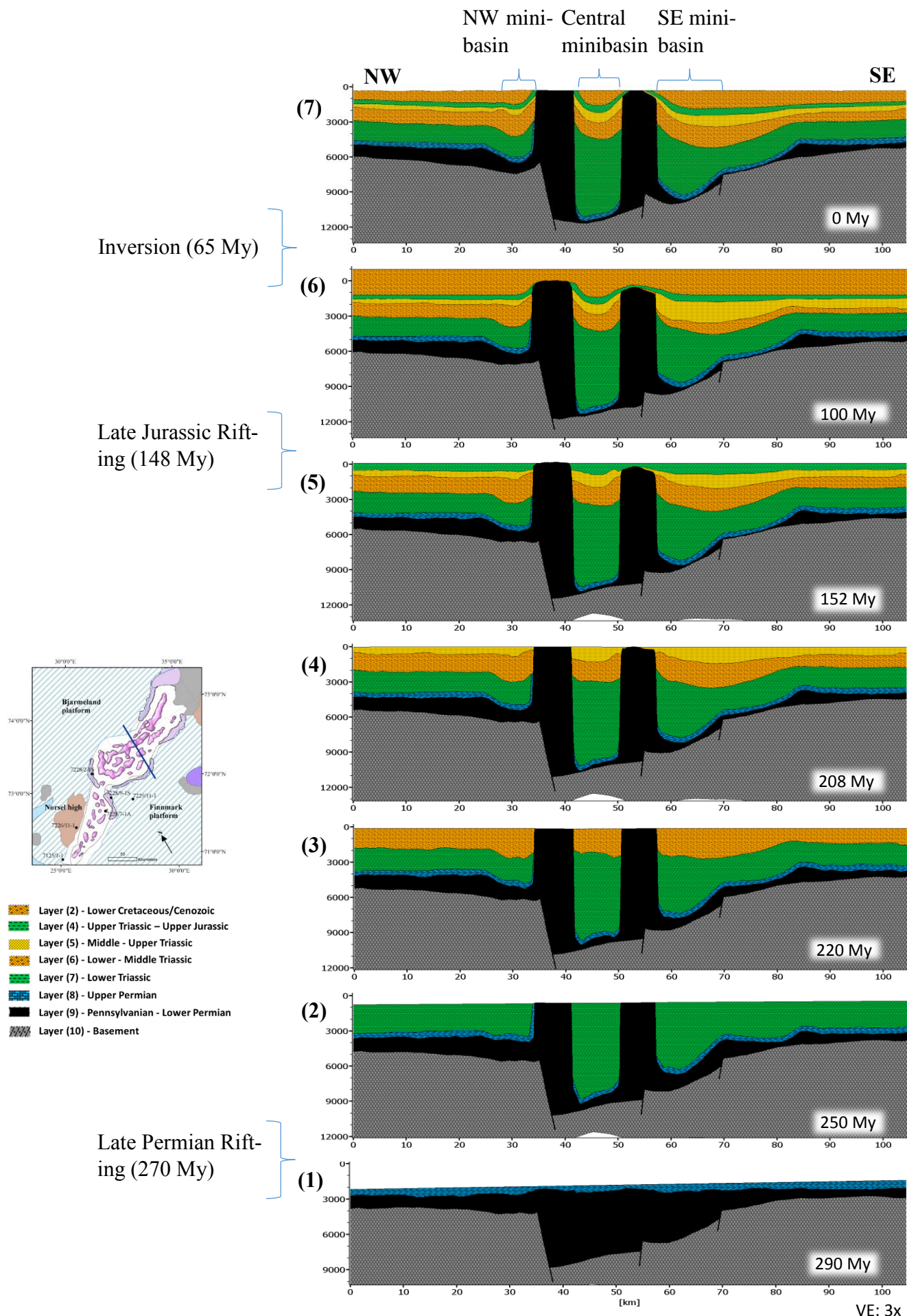


Figure 21 – Lithological and structural evolution of section 2, including the timing of rifting events

6.2.2. Temperature evolution

During the initial Carboniferous-Permian stage (step 1; Figure 22), the temperature was relatively low (30 to 60°C) despite the high heat flow values from the basement. Throughout the basin initial stages (steps 2 to 4; Figure 22) temperature was relatively unaltered until an overall increase during Late Jurassic rifting (step 5 to 6; Figure 22). However followed by a general thermal decrease after the basin's Cenozoic inversion at 65 My until present day (step 6 to 7; Figure 22).

After the salt diapirs started piercing the overburden, the basin was divided in three minibasins with different temperature histories. The temperature in the NW minibasin increased gradually from ~90°C (step 2) to ~180°C (step 6) (Figure 22), followed by a rapid temperature decrease after inversion and its lower heat flow, where today the temperature is ~120°C (step 7; Figure 22). After the Late Permian rifting, the central minibasin's temperature rose steadily until the Late Jurassic rifting (steps 2 to 5; Figure 22). Subsequently, the temperature increased from ~240°C (step 5) to ~270°C (step 6, Figure 22). Following tectonic inversion at step 7, heat flow is significantly lower when compared to the former rifting events, therefore the temperature in the central minibasin reduced considerably from ~270°C (step 6) to ~180°C (step 7, Figure 22).

The SE minibasin followed a very similar thermal evolution as the central minibasin. The SE minibasin shows temperatures reaching around 180°C in step 2 (Figure 22). Here the temperature rose gradually attaining more than 240°C just before the Late Jurassic rifting (steps 2 to 5; Figure 22). Following this rifting event, the temperature in the SE minibasin reached its highest value of ~270°C (step 6; Figure 22). After tectonic inversion, the temperature decreased considerably to a maximum of ~210°C (step 7; Figure 22), which is also related to lower heat flow values.

6.2.3. Reservoir temperature evolution

After the Kobbe and Snadd Formations were deposited, the temperatures in the reservoir rocks in the three minibasins ranged from 30 to 90°C (steps 3, 4; Figure 24). The temperature in the reservoirs increased gradually through time until the tectonic inversion (step 3 to 6; Figure 24). The SE minibasin shows the largest reservoir temperature variations from ~90°C (step 3) to ~220°C (step 6; Figure 24). The central minibasin reveals the lowest reservoir temperature variations ranging from ~60°C (step 3) to ~140°C (step 6) (Figure 24). Sedimentation of the Hekkingen Formation contributed to further burial of the reservoir rocks inducing an increase in temperature during the Late Jurassic rifting in all three minibasins (step 5; Figure 24). However, after tectonic inversion, the reservoir rock temperatures decreased considerably until the present day, mainly due to low heat flow values (Figure 23 and Figure 24, step 7). Figure 23 illustrates the present-day reservoir temperatures of four pseudo wells along the section. Notice the Upper Cretaceous/Cenozoic unit low temperature. Despite being a unit with reservoir properties, it shows very low temperatures due to its closeness to the surface.

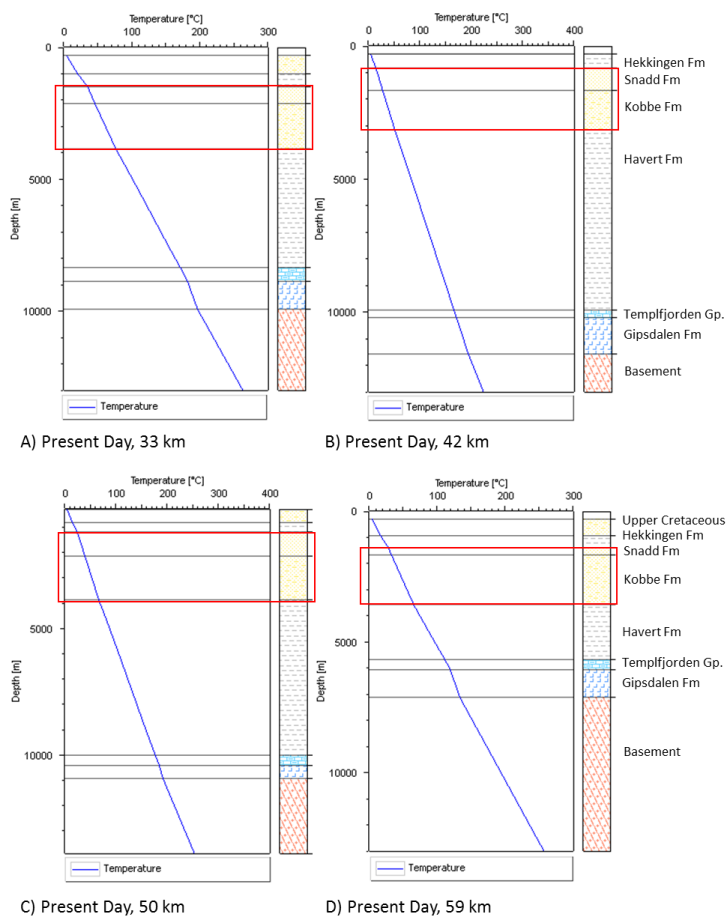


Figure 23 - Present day reservoir temperatures for four pseudo-wells along the section. Location of wells is shown in Figure 29 II.

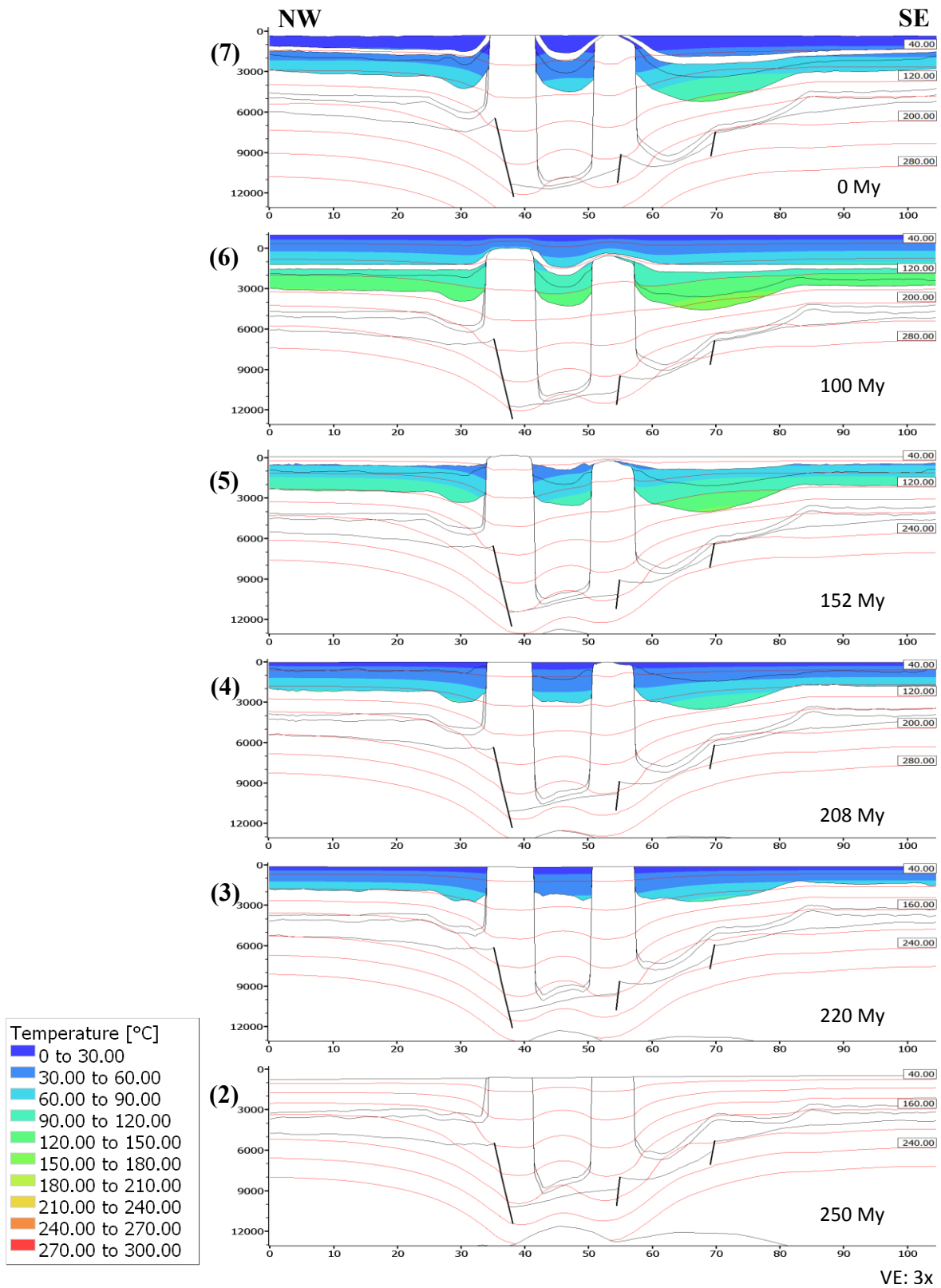


Figure 24 – Evolution of reservoir temperatures in section 2.

6.2.4. Maturation of source rocks

Source rock maturation started after Late Permian rifting (270 My). The central and SE minibasins shared a similar maturation evolution. The maturation of the NW minibasin was progressive through time. The Templefjorden Group and Lower Havert Formation in the central and SE minibasins show high maturation values ranging from 1.3 to 2% by 250 My. However, in the diapir flanks, maturation values are lower, showing ranges from 0.7 to 1.3%, indicating main and late oil stages (step 2; Figure 25). During the same period, the Mid Havert units in the central and SE minibasins reached early oil stages (0.55 to 0.7%). In the NW minibasins lower source rocks (Templefjorden Group and Lower Havert Formation) show maturation values ranging from 0.7 to 1.3%, although in the diapir flank, maturation values drop to a range of 0 to 0.7%, indicating immature to early oil stages by 250 My (step 2; Figure 25).

Source rock maturation increased steadily until the Late Jurassic rifting by 148 My (step 2 to 5; Figure 25 and Figure 37 in Appendix). After this rifting event, the basin's temperature increased and consequently source rock maturation followed accordingly. Lower source rocks (Templefjorden Group and Lower Havert Formations) in the central and in the SE minibasin show a maturation range of 2 to more than 4%, indicating dry gas and overmatured stages by 100 My (step 6; Figure 25). The Upper and Mid Havert Formation display maturation values from 1 to less than 2%, representing late oil to wet gas stages by 100 My (step 6; Figure 25). However, in the vicinity of the salt diapirs, maturation values are lower (Figure 25 and Figure 37 in Appendix). At the same time, the Hekkingen source rocks in all three minibasins reached maturation values higher than 0.55%, indicating early oil stages (step 6; Figure 25). After tectonic inversion and contrary from section 1, maturation values slightly increased (step 7; Figure 25). It is important to mention that today, source rocks in contact with the salt structure in the NW minibasin, show low maturity values despite maturation values of 1 to more than 4% in the distal parts.

7. Discussion

Assuming the existence of Upper Permian and Lower Triassic source rocks in the sections, the results suggest the existence of a working petroleum system in which tectonics and halokinesis caused profound temperature variations through time. Subsidence rates (total and tectonic subsidence) in the Nordkapp Basin were considerably high, particularly in the Early Triassic (Figure 26). The Early Triassic (approximately at 250 My) high subsidence rate was mainly due to rifting ($\beta = 1.4$) and loading of the LES by Lower Triassic siliciclastics, inducing halokinesis (Rojo et al. submitted). During this rifting phase, Upper Permian and Lower Haverf source rocks subsided to depths of 5 to 9 km (Figure 17 step 2 and Figure 22 step 2, respectively). Furthermore, continuous sedimentary deposition through time led the basin to reach depths of 9 km in section 1 and 11 km in section 2 at 100 My (Figure 17 step 6 and Figure 22 step 6).

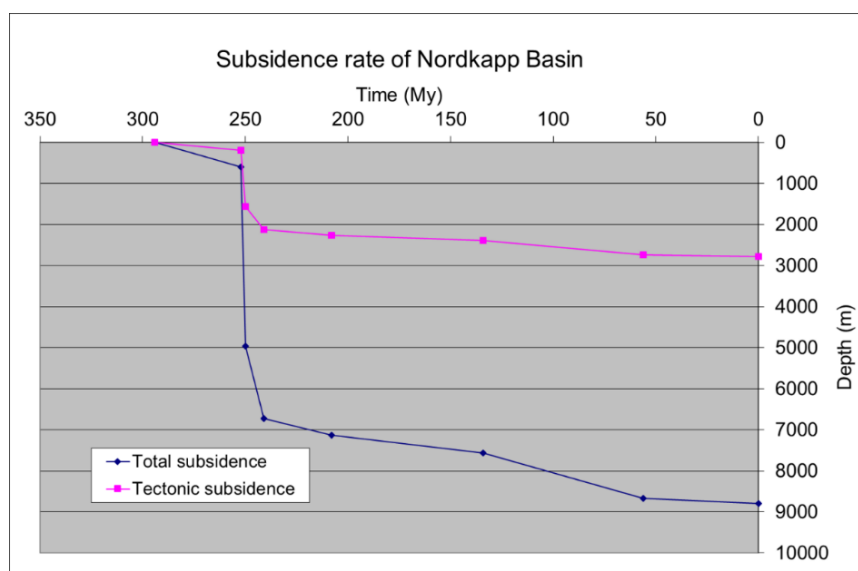


Figure 26 - Subsidence rate of the Nordkapp basin at pseudowell (section 1).

Temperature is important for both maturation and transformation of source rocks and hydrocarbon preservation in reservoir rocks. The concept of the ideal temperature window or optimum entrapment zone for hydrocarbon preservation by Nadeau et al. (2005) was used to evaluate preservation as function of temperature. This *golden zone* is defined empirically, based on a statistical analysis of temperature, pressure, hydrocarbon occurrences, and petrological analysis of basins worldwide, as the depth interval in the temperature range 60–120°C, where reservoir rocks have the highest potential to preserve hydrocarbons. Nadeau et al. (2005) suggested that above 120°C pore pressure starts to reach the hydro-fracturing pressure, entering the ‘hydrocarbon expulsion zone’, whereas biodegradation occurs under 60°C.

7.1. Impact of halokinesis on petroleum system

In order to understand the impact of salt on the petroleum system, (1) numerical tables of thermal influence, (2) integrated combined plots of source rock maturation, and (3) temperature history plots of potential Triassic reservoir rocks, were made.

7.1.1. Thermal influence

Heat flow was higher in the early stages of the basin development. The Late Carboniferous rifting phase had the highest stretching factor of all rifting phases (β factor of 2) throughout the basin history (Clark et al., 2014), contributing to high temperatures. β decreased through time; therefore, later rifting events had only a slight heat flow impact on the basin temperature (Figure 17 and 22).

In section 1 and 2, at 290 My, the basin was covered by the salt layer. This inevitably reduced the basin temperature despite the high heat flow, which is evidenced by the 80°C isotherm around 60 km (Figure 27). Notice the temperature decrease caused by the high thermal conductivity of the salt. Therefore, the fact that the salt layer was covering the basin resulted in thermal depletion throughout the basin evolution. Otherwise, the basin geothermal gradient would have been greater.

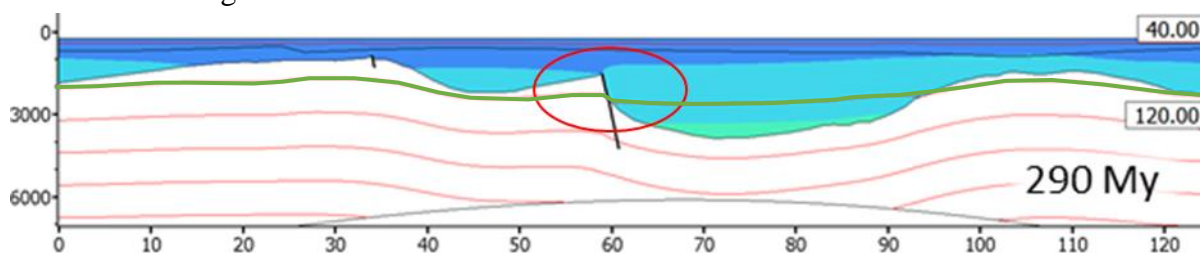


Figure 27 - Thermal behavior of the sag-basin in the first stage of its evolution from section 1; red circle shows the thermal response of salt from the radiogenic heat flow; green line shows the 80°C isotherm.

Tables 3 and 4 show numerically the halokinetic thermal impact in both sections. The sections outer boundaries are likely to show a more stable thermal behavior since the salt diapir thermal impact does not reach these regions. This is evidenced by the steady temperature values away from the diapir (Tables 3 and 4). Therefore, these outer regions are assumed to be the standard thermal behavior without the influence of halokinesis. The closer the point of observation is to the center of the diapir, the lower the temperature (tables 3 and 4). In average, the temperature from the outer boundaries is reduced 40 °C towards the center of the diapir in section 1 (table 3), and 37°C in section 2 (table 4). This confirms a major temperature reduction on the units surrounding the diapirs.

		Distance (Km)													
Present day	Depth	10	20	30	40	50	60	70	80	90	100	110	120		
	3000	89	80	79	70	50	31	40	59	78	80	80	80	Degree (°C)	
	5000	140	131	129	120	80	59	90	121	140	148	130	130		
	7000	-	-	-	-	110	78	122	178	190	185	170	170		
		Distance (Km)													
100 My	Depth	10	20	30	40	50	60	70	80	90	100	110	120		
	3000	110	100	100	90	80	60	75	90	100	100	100	100	Degree (°C)	
	5000	170	170	160	140	100	90	118	140	160	165	150	150		
	7000	-	-	-	180	145	100	160	190	210	200	195	195		
		Distance (Km)													
152 My	Depth	10	20	30	40	50	60	70	80	90	100	110	120		
	3000	120	120	120	110	80	60	90	105	115	120	120	120	Degree (°C)	
	5000	200	200	180	160	115	85	125	160	165	180	180	180		
	7000	-	-	-	-	150	110	160	210	230	220	220	220		
		Distance (Km)													
208 My	Depth	10	20	30	40	50	60	70	80	90	100	110	120		
	2000	80	80	80	75	55	45	55	60	60	60	60	60	Degree (°C)	
	4000	160	160	155	130	90	70	95	120	120	155	150	150		
	6000	-	-	-	-	130	100	140	195	200	190	195	195		
		Distance (Km)													
220 My	Depth	10	20	30	40	50	60	70	80	90	100	110	120		
	1000	80	80	75	65	60	35	55	75	80	90	80	80	Degree (°C)	
	2000	120	120	120	100	80	45	75	90	100	120	110	110		
	3000	170	170	160	150	90	60	100	130	130	150	150	150		
		Distance (Km)													
250 My	Depth	10	20	30	40	50	60	70	80	90	100	110	120		
	1000	80	80	75	60	55	30	55	60	70	80	70	70	Degree (°C)	
	2000	130	125	120	100	80	45	80	100	100	120	110	110		
		Distance (Km)													
290 My	Depth	10	20	30	40	50	60	70	80	90	100	110	120		
	1000	60	60	60	60	55	50	60	60	60	65	60	60	Degree (°C)	
	2000	80	80	85	80	75	70	70	70	70	80	85	80		

Table 3 - Numerical values of temperature related to depth and position for section 1. The column in yellow is at the position of the salt diapir.

		Distance (Km)												
Present day	Depth	10	20	30	40	50	55	60	70	80	90	100	Degree (°C)	
	3000	89	80	74	45	50	45	61	89	90	91	91		
	5000	152	150	117	82	90	80	100	140	165	170	171		
	7000	-	-	152	115	121	115	150	195	200	200	200		
		Distance (Km)												
100 My	Depth	10	20	30	40	50	55	60	70	80	90	100	Degree (°C)	
	3000	150	150	130	120	120	125	130	140	145	145	145		
	5000	220	215	180	155	160	160	170	180	230	220	200		
	7000	-	-	220	190	200	200	230	245	-	-	-		
		Distance (Km)												
152 My	Depth	10	20	30	40	50	55	60	70	80	90	100	Degree (°C)	
	3000	150	145	110	80	100	100	110	135	150	160	160		
	5000	210	200	160	120	140	145	165	200	210	220	220		
	7000	-	-	-	-	185	180	210	250	-	-	-		
		Distance (Km)												
208 My	Depth	10	20	30	40	50	55	60	70	80	90	100	Degree (°C)	
	2000	90	90	70	60	60	60	65	80	85	105	105		
	4000	170	160	120	95	90	90	110	130	150	180	180		
	6000	-	-	-	130	130	130	150	200	-	-	-		
		Distance (Km)												
220 My	Depth	10	20	30	40	50	55	60	70	80	90	100	Degree (°C)	
	2000	90	90	70	60	60	55	60	80	90	95	95		
	4000	170	165	130	100	100	100	120	160	180	180	180		
	6000	-	-	-	130	140	135	160	210	-	-	-		
		Distance (Km)												
250 My	Depth	10	20	30	40	50	55	60	70	80	90	100	Degree (°C)	
	2000	90	90	80	50	50	50	70	90	100	100	100		
	4000	170	165	130	90	90	85	120	180	180	180	180		
	6000	-	-	-	130	130	130	180	210	-	-	-		
		Distance (Km)												
290 My	Depth	10	20	30	40	50	55	60	70	80	90	100	Degree (°C)	
	1000	70	70	70	65	70	65	70	70	70	70	70		
	2000	-	-	-	95	90	95	100	120	-	-	-		

Table 4 - Numerical values of temperature related to depth and position for section 2. The columns in yellow are at the position of the salt diapirs.

7.1.2. Potential petroleum system on the Nordkapp Basin

In order to assess a petroleum system, one must consider (1) source rock maturation, (2) reservoir temperature and properties, (3) migration pathways and (4) trapping/accumulation of hydrocarbons. The diapir flanks have the best conditions for the petroleum system, mainly due to the salt thermal influence in source rocks and reservoirs. The diapir flanks also exhibit pinch-outs at the end of offlapping beds. Hence, pseudowells were made near the salt diapir flanks and evaluated (Figure 29).

(1) Kerogen in source rocks of Late Permian and Lower Triassic age started to transform into hydrocarbons by 250 My as substantiated by vitrinite reflectances higher than 0.6% Ro (Figure 20 and 25). In section 1, early to late oil stages in the diapir flanks were reached by 100 My (step 5, Figure 20). In section 2, these conditions were reached by the same time (step 5, Figure 25). This period marks the highest maturation levels attained in the basin and a wide variety of petroleum phases.

(2) Reservoir rocks (Kobbe and Snadd Formations) in the minibasins and salt diapir flanks from both sections display temperature values within the golden zone (Figure 29). In section 1, reservoirs in the northern pseudowell were within the golden zone since 208 My until almost the present, while reservoirs in the southern pseudowell achieved the golden zone by 152 My until roughly 50 My (Figure 29 I). In section 2, reservoirs in all four pseudowells were in the golden zone by 152 to around 40 My (Figure 29 II). These reservoir temperatures were optimum for hydrocarbon preservation. However, during and after inversion (70 My) the temperature of the reservoir units decreased. Consequently, the reservoir quality is lower today.

In section 1 and 2 reservoir porosity reached 20-35% by 152 My, indicating very good porosity values. After Late Jurassic rifting, reservoir porosities decreased with deposition of Late Jurassic and Upper Cretaceous units. However, during this period (100 My) porosity values are between 15-25% in section 1 and 15-20% in section 2, indicating good reservoir porosity (Figure 1 and 4). In addition, present day average reservoir porosity values are more than 15% in both sections. Therefore, it is reasonable to say that the reservoir units have a decent quality.

(3) NW progradation of Lower Triassic units caused salt movement (Rojo et al., submitted). Continuous salt growth induced up-dip lateral truncation (or pinch-out) of the Triassic units towards the salt diapir (Figure 28). Therefore, hydrocarbon migration from the source rocks could migrate laterally and upwards to the overlying reservoir units.

(4) After the shales of the Hekkingen Formation were deposited, the sediments covering the salt domes could provide conditions to trap hydrocarbons due to its low permeability properties, especially during and after inversion (Figure 28 step B), assuming the compression provided trapping structures. In addition, the shales from the Hekkingen Formation could prevent the hydrocarbons in the reservoir to further migrate upwards assuming a high seal capacity.

There are also potential structural traps at the basin boundaries associated with suprasalt faults. However, along these faults reservoir units have been offset several times thus increasing the risk of leakage.

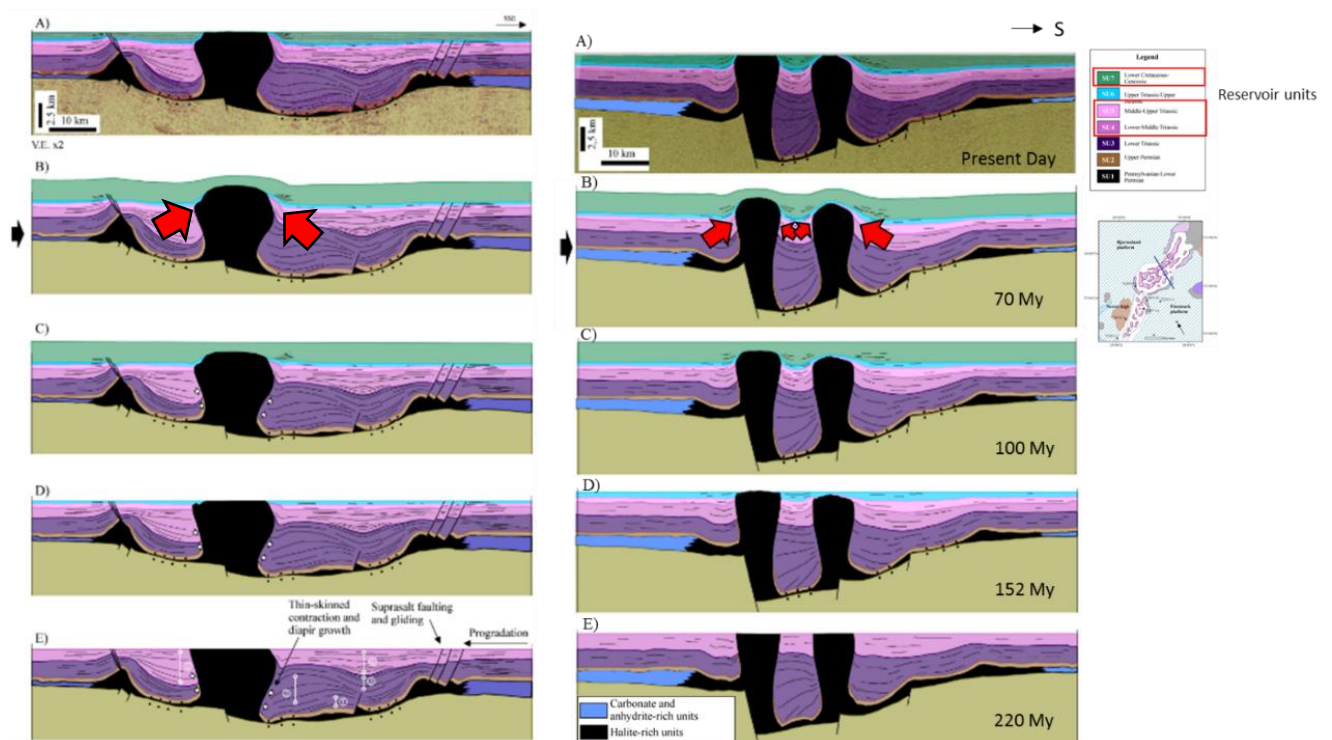


Figure 28 – Restorations (Rojo et al., submitted) showing possible migration of hydrocarbons and entrapment zones (red arrows). Left) Section 1; Right) Section 2.

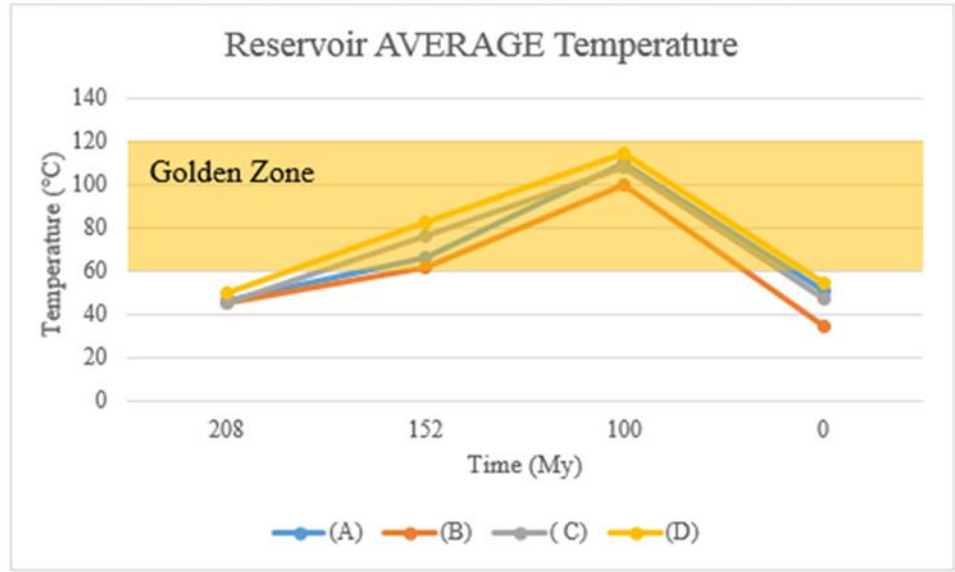
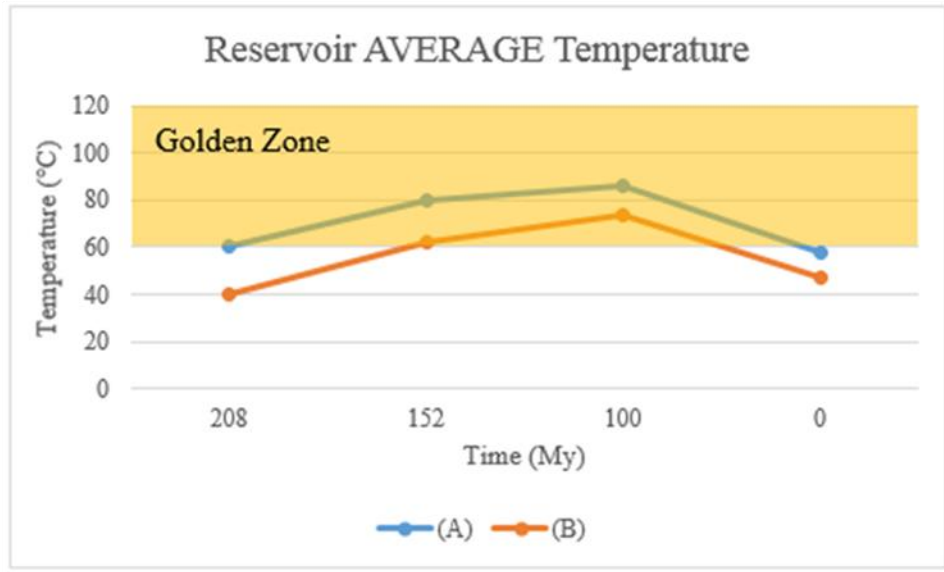
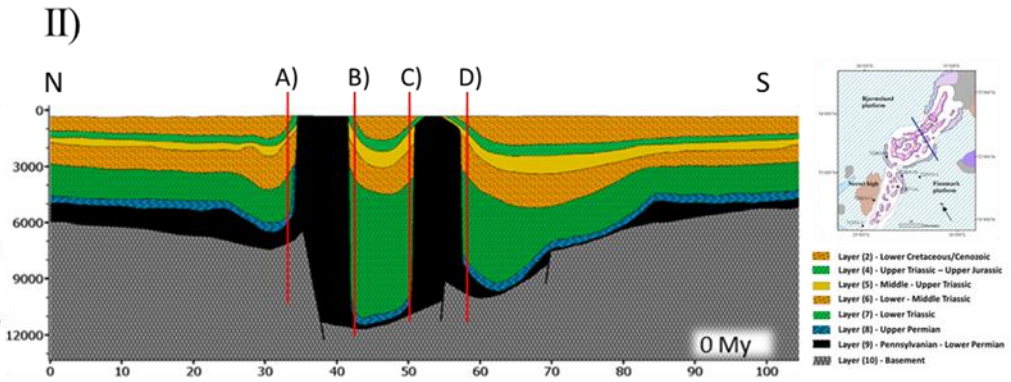
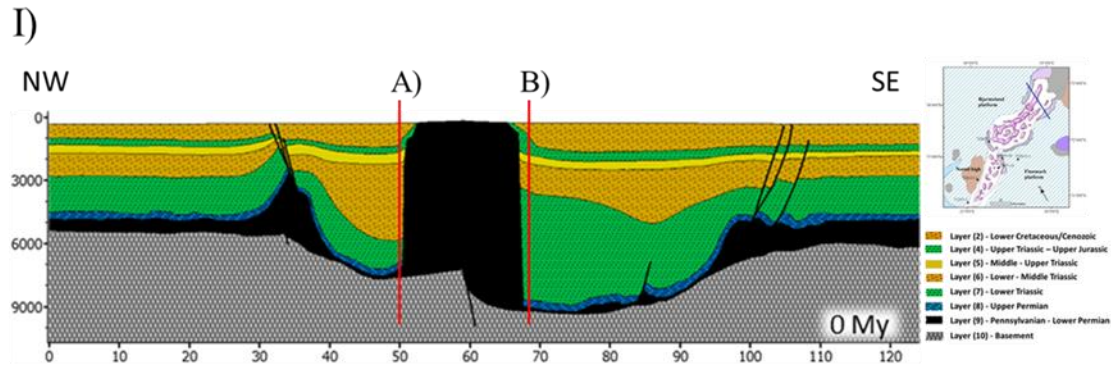


Figure 29 - Reservoir average temperature/time plots. I) section 1 pseudowells position and their respective reservoir temperature; II) section 2 pseudowells position and their respective reservoir temperature.

7.2. Level of certainty

The level of certainty for a petroleum system represents the degree to which the available geological and geochemical data support the hypothesis that petroleum within the reservoir rocks originated from the designated source rocks occurs (Magoon and Dow, 1994). There are three levels of certainty: (1) known, (2) hypothetical, and (3) speculative (see Magoon and Dow, 1994).

Heat flow values were crucial to establish the boundary conditions for the model. Present day and Late Jurassic rifting heat flow values were estimated by a correlation between burial history rift models and VRo well data. Therefore, the level of certainty for these estimates could perhaps be raised to known, despite the closeness of the wells to the sections (the closest well is 152 km away from section 1 and 87 km from section 2). On the other hand, Late Permian and Late Carboniferous rifting events were not correlated with wellbore VRo data, but only with a burial history, rift model, therefore the level of certainty for these estimates can be considered hypothetical.

There is overall agreement that the source of oil in the Barents Sea comes from the Early to Late Permian Templefjorden Group, which is a known hydrocarbon play in the Arctic region, e.g. on the Finnmark Platform, Loppa High and Sverdrup Basin (Jafarian et al., 2017). The Templefjorden Group in the Nordkapp basin is at depths well below hydrocarbon generation (e.g. Bissada et al., 1990; Sassen et al., 1993). Because, the proposed deep source rocks have not been penetrated by wells nor confirmed to be actual sources of petroleum, the level of certainty for the Templefjorden Group is considered hypothetical. In addition, lithological properties of the shales of the Havert Formation suggest the possibility that they can be a source rock. However, since this unit is a 2 km thick mix of shales and sandstones, the probability of hydrocarbon generation in this unit is ambiguous. Therefore, the level of certainty for the Havert Formation to be a source rock is speculative. In addition, this study assumes that if the Hekkingen Formation shales have seal capacity, then hydrocarbon preservation in the Nordkapp basin is plausible. Nevertheless, without lithological data in the area, the level of certainty for top sealing remains hypothetical.

The modelled geometry of the salt structures in the present study do not represent their real shape. This was due to the software limitations (see next section).

7.3. Model Limitations and Mitigation

When building the model, two limitations were found. In the restorations, the salt structures contain overhangs. This overhang is a major limitation, since the steepest diapir

margin the program can simulate is vertical (vertical grid). In the first trials, the real shape of the salt structures was modeled. However, once simulated, the results demonstrated problems recognizing its shape, defying geological basic structural concepts.

The other limitation relates to the fault blocks in the northern part of section 1, particularly in the last restoration step. When building the formation blocks, I was faced with fault blocks that were juxtaposing with two or more formations below (Figure 31, b). The problem arose when creating the formation block, since the program did not allow the blocks as they were exhibited in the provided restoration (Figure 31).

In order to overcome these two limitations, some decisions were made. For the first limitation, I was forced to adjust the shape of the salt diapirs. They were modified in a way to realistically approximate the diapirs actual shape. This alteration was conducted to create an average width of the diapirs (Table 3) and make them columnar as shown in Figure 30. These geometrical alterations were made in all restorations steps where the salt structure had an overhang (Model 1: step 3 to 7; Model 2: step 2 to 7). In Model 1, the top width of the salt structure was reduced in every step approximately 1.5 km, and the bottom width increased around 2 km (Figure 30). In Model 2, the top width of the salt structures was reduced approximately 2 km, and the bottom width was increased approximately 1 km (Figure 30). For the second limitation, I was forced to shift the fault block upward, just enough for the model to simulate it properly (Figure 31, c). This shift was not significant enough to change the overall geometry of the formations. However, this shift could have influenced the temperature distribution, although not in a critical position for evaluating hydrocarbon accumulation and preservation.

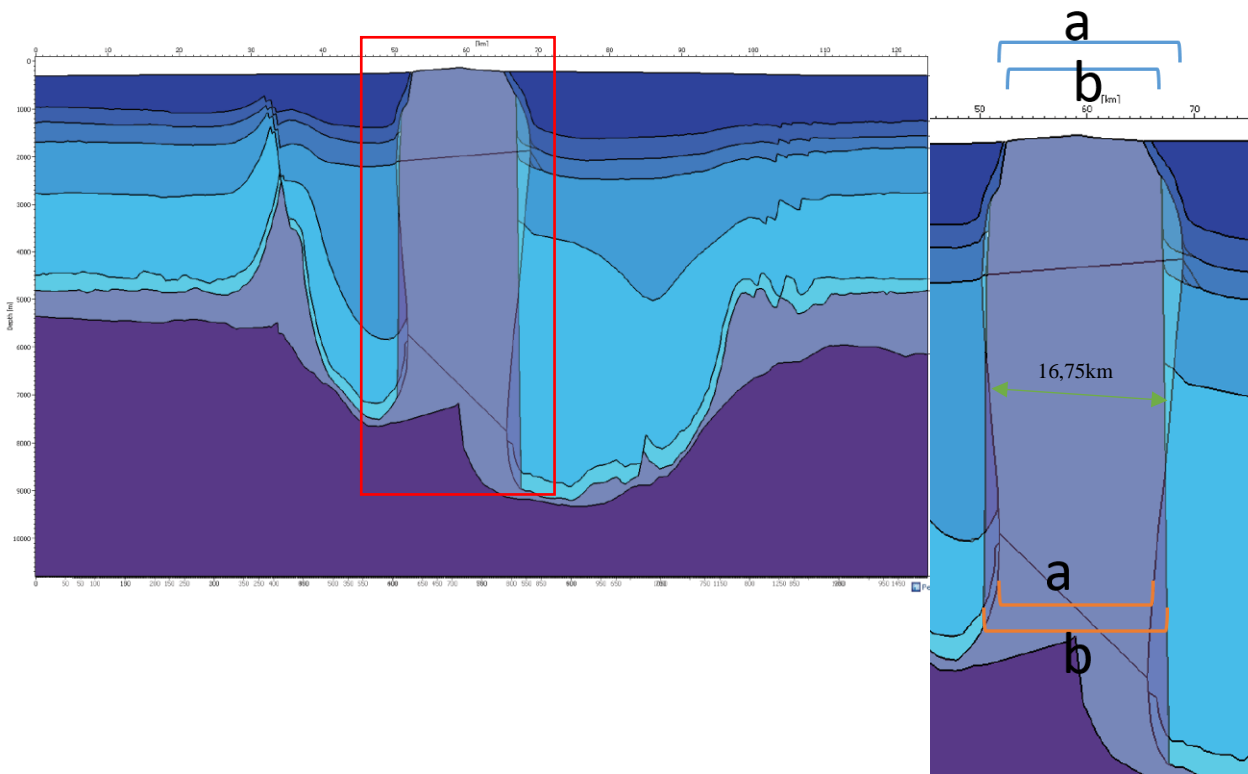


Figure 30 - Overlap of restoration 1 with the altered model showing the range of modifications. The blue marks represent the top width and the orange marks represent the bottom width. “a” represents the unaltered shape and “b” represents the altered one.

Table 5 - Quantitative geometrical alterations of the salt structures.

		Name	Width (km)	Average (km)
Section 1	Unaltered	a	18,5	16,75
		a	15	
	Altered	b	16	16,75
		b	17,5	
Section 2	Unaltered	a	10	8
		a	6	
	Altered	b	7	8
		b	9	

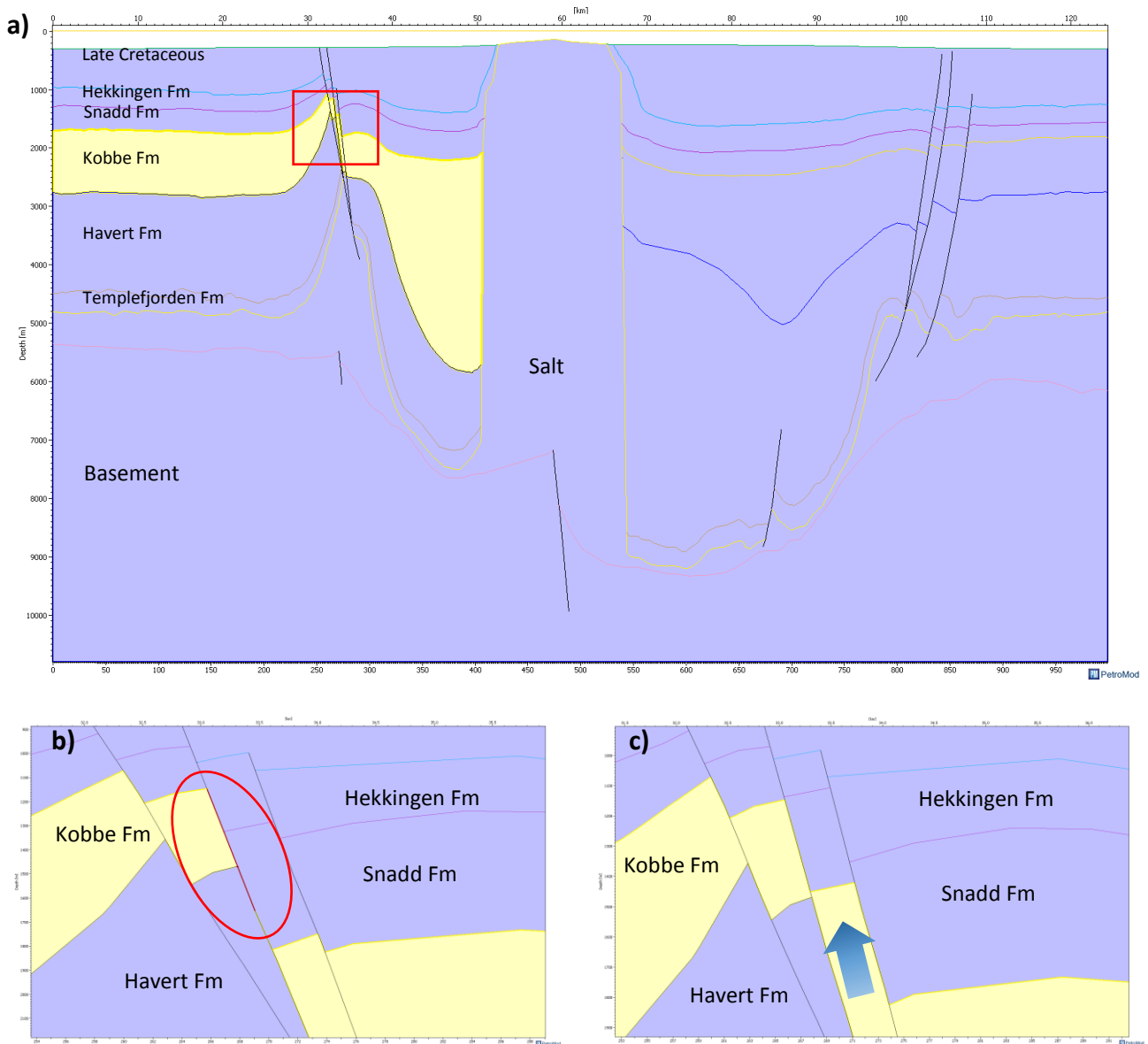


Figure 31 - 2D TeckLink Block building limitation and solution. a) Present day Paleo Section with problematic area within the red square. b) Close up of the problematic area in red shows the limitation of the software. c) Mitigation by a 200m upward shift of the Kobbe Formation fault block indicated by the blue arrow.

7.4. Implications and future work

Considering the vast area of salt deposition in the Barents Sea (Rowan and Lindsø, 2017), it is safe to assume that the salt and its mobilization influenced the geothermal gradient of the region. Without Early Permian salt deposition and posterior salt mobilization, the geothermal gradient of the region would have been relatively higher.

Without deposition of the salt, the basin would present overmature source rocks and reservoirs, since the influence of the basement radiogenic heat flow would have been higher. Moreover, without halokinesis, the source rocks and the reservoirs could also have been overmatured. Therefore, a comparison between a basin with salt structures and a basin without is key to understand the full scope of salt effect on a basin's thermal evolution.

Since the present study relies on a modelling software that has limitations modelling the real shape of the salt diapirs, it is crucial to perform a more accurate study incorporating the actual shape of the diapirs. This is important because the shape of the salt structures influences the radius of their thermal impact. After improving the diapirs shapes in 2D, a 3D model would be very important for understanding the thermal evolution of the basin in 3D.

Moreover, it is important to have better data related to the petrophysical properties of the formations, since in this study I assumed some of the formations properties due to the lack of well data in the area. This would improve the assessment of a working petroleum system in the Nordkapp basin.

8. Conclusions

Modelling the thermal evolution of different salt structures has shown that the refraction of heat flow within and around the structures induces a dipole shaped temperature anomaly. The thermal effect of these high conductivity structures provides new constraints for evaluating the petroleum system in the Nordkapp basin. Therefore, after modelling the basin, this region can potentially hold a petroleum system at high depth (e.g. > 3 km). Essential elements of this system include source rocks of Late Permian and Early Triassic age; Middle to Late Triassic siliciclastic reservoir rocks, salt diapirs as migration barriers, and thick overburden strata ranging from Jurassic shales to Cenozoic siliciclastics. Although the petroleum system might cover a much larger area regionally, the modelling was restricted to two 2D restorations and thermal evolution of the basin.

The petroleum system of the study area was significantly affected by Early Permian halokinesis. Evaluating this evolving petroleum system requires a means of quantifying the halokinetic thermal influence (Table 3 and 4). The integration of stratigraphy and structural

evaluation of halokinesis provides the necessary foundation for conducting thermal maturation modelling and petroleum migration analyses. Sequence stratigraphy indicates the lithological properties and their geometries related to ages of the incremental structural restorations. These incremental restorations, in turn, show the salt geometries and thickness variations through time. The salt high thermal conductivity retards the thermal maturation of the source rocks at high depths and leads to optimum reservoir rock temperatures within the golden zone. The siliciclastic strata of the region in association with hydrocarbon buoyancy, overpressures and synkinematic strata related with salt growth caused hydrocarbon migration to be deflected from vertical to laterally up the diapirs and accumulated by strata truncation on the flanks of the salt diapir. The Hekkingen Formation shales covering the Triassic reservoir rocks could have provide the top seal preventing further vertical fluid flow. Therefore, creating an ideal entrapment zone.

Major halokinesis started during source rock deposition and evolved through time until present day. Besides temperature, halokinesis influenced migration pathways and thus created zones of petroleum concentration neighboring the salt structures. In section 1, maturation started after Late Permian rifting and reached its maturation peak at 100 My, with source rock neighboring the salt diapir reaching mainly the late oil window. In section 2, source rock maturation showed a similar history from section 1, reaching its peak with late oil to dry gas stages at 100 My. During this time, reservoir rocks from both sections were well inside the golden zone. Both sections show a significant period of time where reservoirs temperature was ideal for hydrocarbon preservation. However today's reservoir temperature suggests that they are no longer inside the golden zone.

The proposed methodology of evaluating the thermal evolution sheds light on deep salt-bearing basins and its impact on petroleum systems. Sequential structural restorations coupled with thermal modelling for petroleum systems analysis, can provide substantial benefits to explorationists in addition to validating interpretations. The overall technique, despite the software limitations, motivates geoscientists to look for other exploration targets, such as the deep salt-related minibasins presented in this study.

9. References

- Anell, I., Braathen, A., and Olaussen, S., 2014, The Triassic--Early Jurassic of the northern Barents Shelf: a regional understanding of the Longyearbyen CO 2 reservoir: *Norwegian Journal of Geology/Norsk Geologisk Forening*, v. 94.
- Baig, I., Faleide, J. I., Jahren, J., and Mondol, N. H., 2016, Cenozoic exhumation on the southwestern Barents Shelf: Estimates and uncertainties constrained from compaction and thermal maturity analyses: *Marine and Petroleum Geology*, v. 73, p. 105-130.
- Behar, F., Vandenbroucke, M., Tang, Y., Marquis, F., and Espitalié, J., 1997, Thermal cracking of kerogen in open and closed systems: determination of kinetic parameters and stoichiometric coefficients for oil and gas generation: *Organic Geochemistry*, v. 26, no. 5-6, p. 321-339.
- Bjørlykke, K., 2015, Heat transport in sedimentary basins, *Petroleum Geoscience*, Springer, p. 273-277.
- Breivik, A. J., Faleide, J. I., and Gudlaugsson, S. T., 1998, Southwestern Barents Sea margin: late Mesozoic sedimentary basins and crustal extension: *Tectonophysics*, v. 293, no. 1-2, p. 21-44.
- Brekke, H., Sjulstad, H. I., Magnus, C., and Williams, R. W., 2001, Sedimentary environments offshore Norway—an overview, *Norwegian Petroleum Society Special Publications*, Volume 10, Elsevier, p. 7-37.
- Cardott, B. J., 2012, Introduction to vitrinite reflectance as a thermal maturity indicator, Adapted from an Oral Presentation at Tulsa Geological Society Luncheon, May 8, 2012, American Association of Petroleum Geologists Search and Discovery.
- Clark, S., Glorstad-Clark, E., Faleide, J., Schmid, D., Hartz, E., and Fjeldskaar, W., 2014, Southwest Barents Sea rift basin evolution: comparing results from backstripping and time-forward modelling: *Basin Research*, v. 26, no. 4, p. 550-566.
- Clark, S. A., Faleide, J. I., Hauser, J., Ritzmann, O., Mjelde, R., Ebbing, J., Thybo, H., and Flüh, E., 2013, Stochastic velocity inversion of seismic reflection/refraction traveltime data for rift structure of the southwest Barents Sea: *Tectonophysics*, v. 593, p. 135-150.
- Corfu, F., Polteau, S., Planke, S., Faleide, J. I., Svensen, H., Zayoncheck, A., and Stolbov, N., 2013, U–Pb geochronology of Cretaceous magmatism on Svalbard and Franz Josef Land, Barents Sea large igneous province: *Geological Magazine*, v. 150, no. 6, p. 1127-1135.
- Dengo, C., and Røssland, K., 2013, Extensional tectonic history of the western Barents Sea: Structural and tectonic modelling and its application to petroleum geology, *Norwegian Petroleum Society [NPF], special publication*, v. 1, p. 91-108.
- Escalona, A., Fjeldskaar, W., and Grunnaleite, I., 2011, Basin modelling across the emergent Lesser Antilles island arc, SE Caribbean and impact on petroleum systems: *First Break*, v. 29, no. 9, p. 77-87.
- Faleide, J. I., Gudlaugsson, S. T., and Jacquart, G., 1984, Evolution of the western Barents Sea: *Marine and Petroleum Geology*, v. 1, no. 2, p. 123-150.
- Faleide, J. I., Tsikalas, F., Breivik, A. J., Mjelde, R., Ritzmann, O., Engen, O., Wilson, J., and Eldholm, O., 2008, Structure and evolution of the continental margin off Norway and the Barents Sea: *Episodes*, v. 31, no. 1, p. 82-91.

- Faleide, J. I., Vågnes, E., and Gudlaugsson, S. T., 1993, Late Mesozoic-Cenozoic evolution of the south-western Barents Sea in a regional rift-shear tectonic setting: *Marine and Petroleum Geology*, v. 10, no. 3, p. 186-214.
- Fossum, B. J., Schmidt, W. J., Jenkins, D. A., Bogatsky, V. I., and Rappoport, B. I., 1999, New frontiers for hydrocarbon production in the Timan-Pechora Basin, Russia: *AAPG Bulletin*, v. 83, no. 12.
- Gabrielsen, R., Grunnaleite, I., and Ottesen, S., 1993, Reactivation of fault complexes in the Loppa High area, southwestern Barents Sea, Norwegian Petroleum Society Special Publications, Volume 2, Elsevier, p. 631-641.
- Gabrielsen, R., Kløvjan, O., and Stølan, T., 1992, Interaction between halokinesis and faulting; structuring of the margins of the Nordkapp Basin, Barents Sea region: *Proceedings Structural and tectonic modelling and its implication to petroleum geology; proceedings 1992*, v. 1, p. 121-131.
- Gabrielsen, R. H., Faereth, R. B., and Jensen, L. N., 1990, Structural Elements of the Norwegian Continental Shelf. Pt. 1. The Barents Sea Region, Norwegian Petroleum Directorate.
- Gac, S., Klitzke, P., Minakov, A., Faleide, J. I., and Scheck-Wenderoth, M., 2016, Lithospheric strength and elastic thickness of the Barents Sea and Kara Sea region: *Tectonophysics*, v. 691, p. 120-132.
- Gernigon, L., Brønner, M., Roberts, D., Olesen, O., Nasuti, A., and Yamasaki, T., 2014, Crustal and basin evolution of the southwestern Barents Sea: from Caledonian orogeny to continental breakup: *Tectonics*, v. 33, no. 4, p. 347-373.
- Gjelberg, J., and Steel, R. J., 1995, Helvetiafjellet Formation (Barremian-Aptian), Spitsbergen: characteristics of a transgressive succession, Norwegian Petroleum Society Special Publications, Volume 5, Elsevier, p. 571-593.
- Glørstad-Clark, E., Faleide, J. I., Lundschieen, B. A., and Nystuen, J. P., 2010, Triassic seismic sequence stratigraphy and paleogeography of the western Barents Sea area: *Marine and Petroleum Geology*, v. 27, no. 7, p. 1448-1475.
- Gradstein, F. M., Ogg, J. G., Smith, A. G., Bleeker, W., and Lourens, L. J., 2004, A new geologic time scale, with special reference to Precambrian and Neogene: *Episodes*, v. 27, no. 2, p. 83-100.
- Grogan, P., Nyberg, K., Fotland, B., Myklebust, R., Dahlgren, S., and Riis, F., 2000, Cretaceous magmatism south and east of Svalbard: evidence from seismic reflection and magnetic data: *Polarforschung*, v. 68, p. 25-34.
- Gudlaugsson, S., Faleide, J., Johansen, S., and Breivik, A., 1998, Late Palaeozoic structural development of the south-western Barents Sea: *Marine and Petroleum Geology*, v. 15, no. 1, p. 73-102.
- Henriksen, E., Bjørnseth, H., Hals, T., Heide, T., Kiryukhina, T., Kløvjan, O., Larssen, G., Ryseth, A., Rønning, K., and Sollid, K., 2011a, Uplift and erosion of the greater Barents Sea: impact on prospectivity and petroleum systems: *Geological Society, London, Memoirs*, v. 35, no. 1, p. 271-281.
- Henriksen, E., Ryseth, A., Larssen, G., Heide, T., Rønning, K., Sollid, K., and Stoupakova, A., 2011b, Tectonostratigraphy of the greater Barents Sea: implications for petroleum systems: *Geological Society, London, Memoirs*, v. 35, no. 1, p. 163-195.

- Hokstad, K., Tašárová, Z. A., Clark, S. A., Kyrkjebø, R., Duffaut, K., Fichler, C., and Wiik, T., 2017, Radiogenic heat production in the crust from inversion of gravity and magnetic data: *NORWEGIAN JOURNAL OF GEOLOGY*, v. 97, no. 3, p. 241-254.
- Hu, S., O'Sullivan, P. B., Raza, A., and Kohn, B. P., 2001, Thermal history and tectonic subsidence of the Bohai Basin, northern China: a Cenozoic rifted and local pull-apart basin: *Physics of the Earth and Planetary Interiors*, v. 126, no. 3-4, p. 221-235.
- Jackson, M. P., and Hudec, M. R., 2017, *Salt tectonics: Principles and practice*, Cambridge University Press.
- Jafarian, E., Kleipool, L., Scheibner, C., Blomeier, D., and Reijmer, J., 2017, VARIATIONS IN PETROPHYSICAL PROPERTIES OF UPPER PALAEOZOIC MIXED CARBONATE AND NON-CARBONATE DEPOSITS, SPITSBERGEN, SVALBARD ARCHIPELAGO: *Journal of Petroleum Geology*, v. 40, no. 1, p. 59-83.
- Jakobsson, M., Macnab, R., Mayer, L., Anderson, R., Edwards, M., Hatzky, J., Schenke, H. W., and Johnson, P., 2008, An improved bathymetric portrayal of the Arctic Ocean: Implications for ocean modeling and geological, geophysical and oceanographic analyses: *Geophysical Research Letters*, v. 35, no. 7.
- Jaupart, C., and Mareschal, J.-C., 2015, Heat flow and thermal structure of the lithosphere.
- Jensen, L., and Sørensen, K., 1992, Tectonic framework and halokinesis of the Nordkapp Basin, Barents Sea, Structural and tectonic modelling and its application to petroleum geology, Elsevier, p. 109-120.
- Johansen, S., Ostistiy, B., Fedorovsky, Y., Martirosjan, V., Christensen, O. B., Cheredeev, S., Ignatenko, E., and Margulis, L., 1993, Hydrocarbon potential in the Barents Sea region: play distribution and potential, Norwegian Petroleum Society Special Publications, Volume 2, Elsevier, p. 273-320.
- Klausen, T. G., Ryseth, A. E., Helland-Hansen, W., Gawthorpe, R., and Laursen, I., 2015, Regional development and sequence stratigraphy of the Middle to Late Triassic Snadd formation, Norwegian Barents Sea: *Marine and Petroleum Geology*, v. 62, p. 102-122.
- Koyi, H., Talbot, C. J., and Torudbakken, B., 1995a, Analogue models of salt diapirs and seismic interpretation in the Nordkapp Basin, Norway: *Petroleum geoscience*, v. 1, no. 2, p. 185-192.
- Koyi, H., Talbot, C. J., and Tørudbakken, B. O., 1993, Salt diapirs of the southwest Nordkapp Basin: analogue modelling: *Tectonophysics*, v. 228, no. 3-4, p. 167-187.
- , 1995b, Salt tectonics in the Northeastern Nordkapp basin, Southwestern Barents sea.
- Larssen, G., Elvebakk, G., and Henriksen, L., 2005, Upper Palaeozoic lithostratigraphy of the southern part of the Norwegian Barents sea; GB Larssen, G. Elvebakk, LB Henriksen et al: *Bulletin/Norges geologiske undersøkelse*.
- Li, M., Wang, T., Chen, J., He, F., Yun, L., Akbar, S., and Zhang, W., 2010, Paleo-heat flow evolution of the Tabei Uplift in Tarim Basin, northwest China: *Journal of Asian Earth Sciences*, v. 37, no. 1, p. 52-66.
- Lundschien, B. A., Høy, T., and Mørk, A., 2014, Triassic hydrocarbon potential in the Northern Barents Sea; integrating Svalbard and stratigraphic core data: *Norwegian Petroleum Directorate Bulletin*, v. 11, p. 3-20.
- Magoon, L. B., and Dow, W. G., 1994, *The petroleum system: chapter 1: Part I. Introduction*.

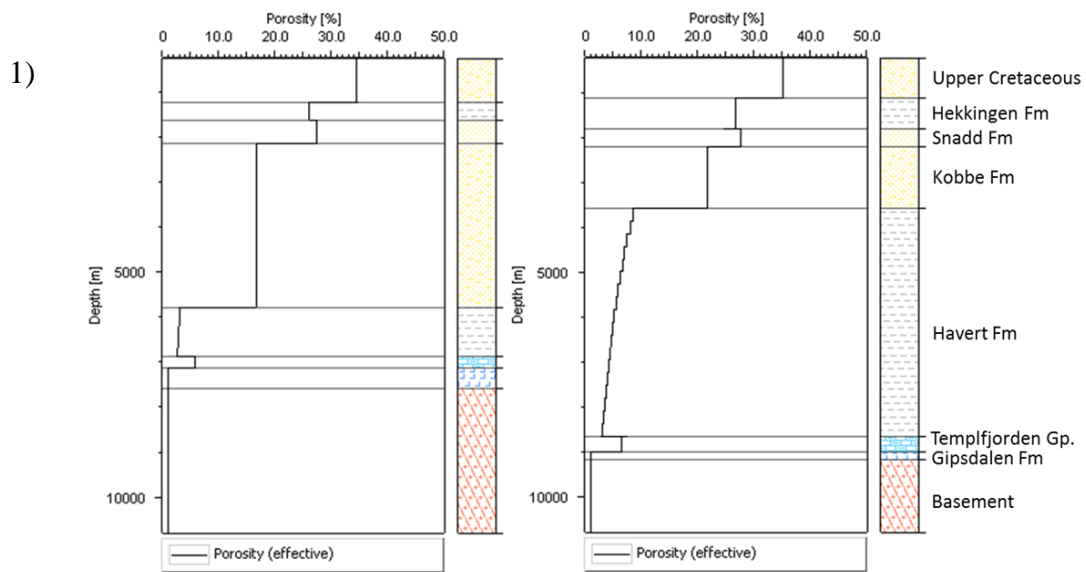
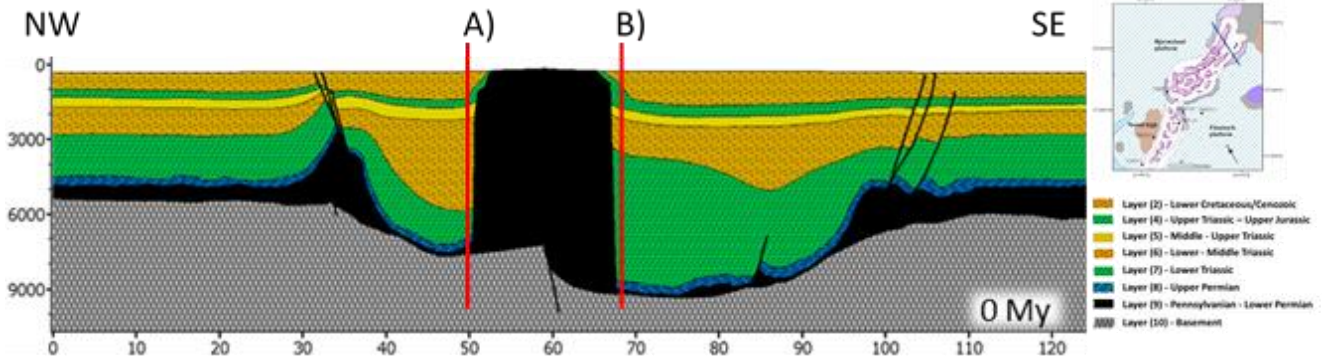
- Marin, D., Escalona, A., Śliwińska, K. K., Nøhr-Hansen, H., and Mordasova, A., 2017, Sequence stratigraphy and lateral variability of Lower Cretaceous clinofolds in the southwestern Barents Sea: *AAPG Bulletin*, v. 101, no. 9, p. 1487-1517.
- McBride, B. C., Weimer, P., and Rowan, M. G., 1998, The effect of allochthonous salt on the petroleum systems of northern Green Canyon and Ewing Bank (offshore Louisiana), northern Gulf of Mexico: *AAPG bulletin*, v. 82, no. 5, p. 1083-1112.
- Mello, U. T., Karner, G. D., and Anderson, R. N., 1995, Role of salt in restraining the maturation of subsalt source rocks: *Marine and Petroleum Geology*, v. 12, no. 7, p. 697-716.
- Nilsen, K. T., Vendeville, B. C., and Johansen, J.-T., 1995, Influence of regional tectonics on halokinesis in the Nordkapp Basin, Barents Sea.
- NPD FactPages, 2018, Norwegian Petroleum Directorate, NPD.
- O'Brien, J., and Lerche, I., 1988, Impact of heat flux anomalies around salt diapirs and salt sheets in the Gulf Coast on hydrocarbon maturity: models and observations.
- O'Brien, J., and Lerche, I., 1984, The influence of salt domes on paleotemperature distributions: *Geophysics*, v. 49, no. 11, p. 2032-2043.
- Ohm, S. E., Karlsen, D. A., and Austin, T., 2008, Geochemically driven exploration models in uplifted areas: Examples from the Norwegian Barents Sea: *AAPG bulletin*, v. 92, no. 9, p. 1191-1223.
- Pascal, C., Balling, N., Barrere, C., Davidsen, B., Ebbing, J., Elvebakk, H., Mesli, M., Roberts, D., Slagstad, T., and Willemoes-Wissing, B., 2011, HeatBar Final Report 2010, Basement Heat Generation and Heat Flow in the western Barents Sea-importance for hydrocarbon systems: *Norges Geologiske Undersøkelse*.
- Riis, F., Lundschie, B. A., Høy, T., Mørk, A., and Mørk, M. B. E., 2008, Evolution of the Triassic shelf in the northern Barents Sea region: *Polar Research*, v. 27, no. 3, p. 318-338.
- Rowan, M., and Lindsø, S., 2017, Salt Tectonics of the Norwegian Barents Sea and Northeast Greenland Shelf, *Permo-Triassic Salt Provinces of Europe, North Africa and the Atlantic Margins*, Elsevier, p. 265-286.
- Rønnevik, H., and Jacobsen, H.-P., 1984, Structural highs and basins in the western Barents Sea, *Petroleum Geology of the North European Margin*, Springer, p. 19-32.
- Stadtler, C., Fichler, C., Hokstad, K., Myrland, E. A., Wienecke, S., and Fotland, B., 2014, Improved salt imaging in a basin context by high resolution potential field data: Nordkapp Basin, Barents Sea: *Geophysical Prospecting*, v. 62, no. 3, p. 615-630.
- Stemmerik, L., 2000, Late Palaeozoic evolution of the North Atlantic margin of Pangea: *Palaeogeography, Palaeoclimatology, Palaeoecology*, v. 161, no. 1-2, p. 95-126.
- Stemmerik, L., Elvebakk, G., and Worsley, D., 1999, Upper Palaeozoic carbonate reservoirs on the Norwegian arctic shelf; delineation of reservoir models with application to the Loppa High: *Petroleum Geoscience*, v. 5, no. 2, p. 173-187.
- Stemmerik, L., and Worsley, D., 2005, 30 years on-Arctic Upper Palaeozoic stratigraphy, depositional evolution and hydrocarbon prospectivity: *Norwegian Journal of Geology/Norsk Geologisk Forening*, v. 85.

- Tsikalas, F., Faleide, J. I., Eldholm, O., and Blaich, O. A., 2012, The NE Atlantic conjugate margins, *Regional geology and tectonics: Phanerozoic passive margins, cratonic basins and global tectonic maps*, Elsevier, p. 140-201.
- Turcotte, D., and Schubert, G., 2002, *Geodynamics*, 456 pp, Cambridge Univ. Press, New York.
- Waples, D. W., 1994, *Maturity Modeling: Thermal Indicators, Hydrocarbon Generation, and Oil Cracking: Chapter 17: Part IV. Identification and Characterization.*

Appendix

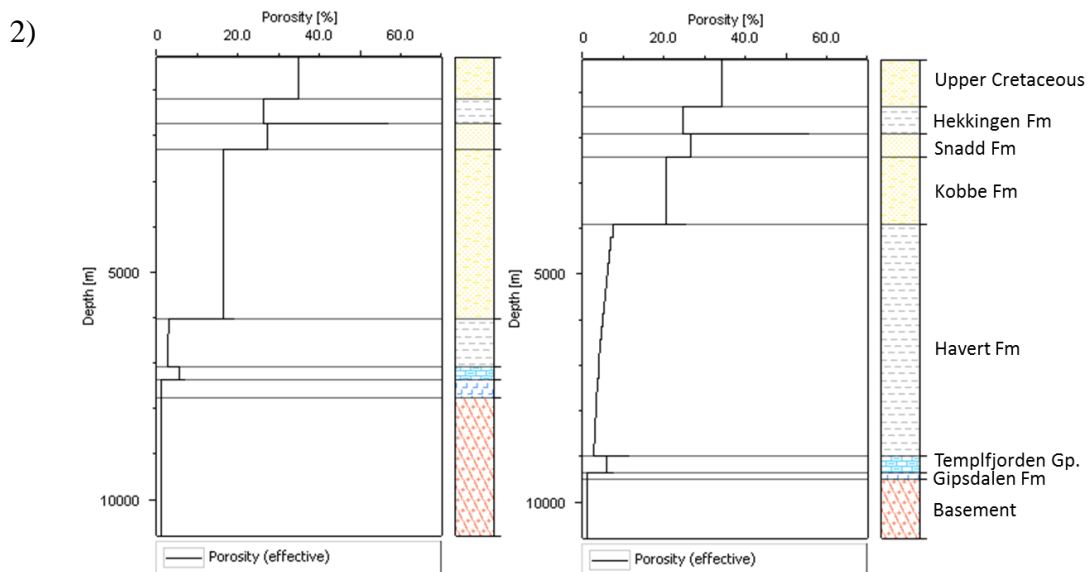
10. Section 1

10.1. Porosity Evolution



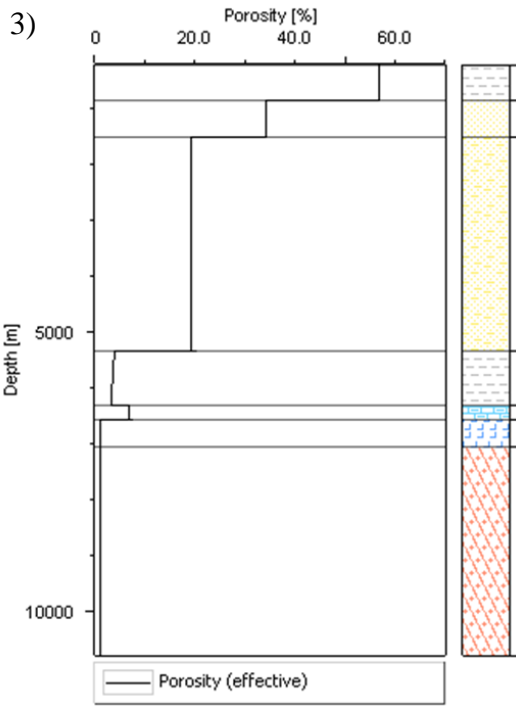
A) Present Day, 50 km

B) Present Day, 69 km

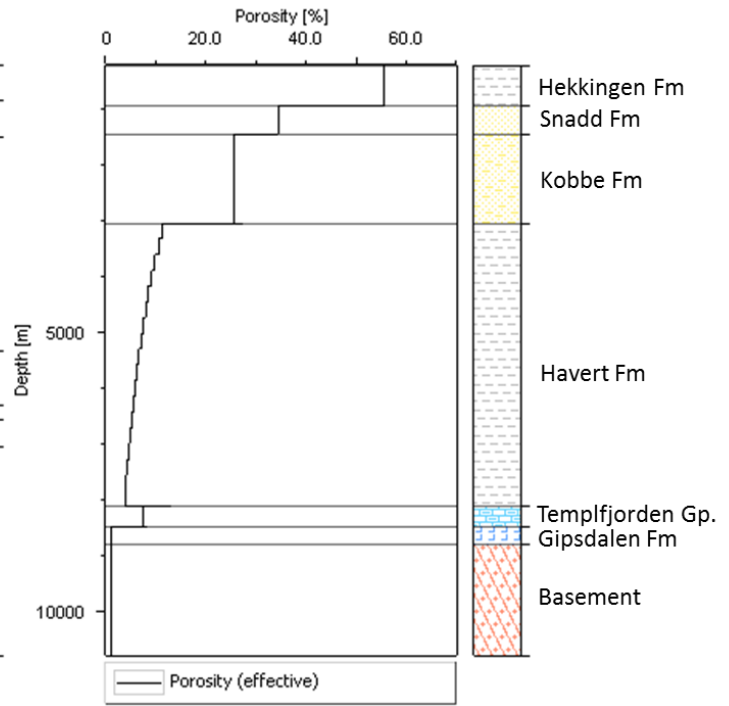


A) 100 My, 50 km

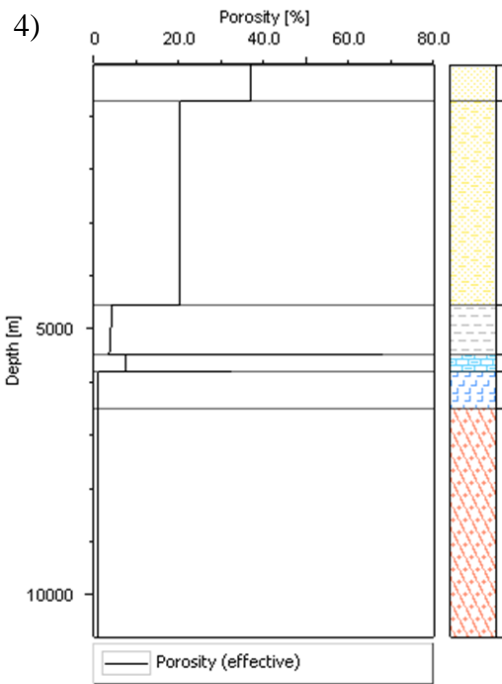
B) 100 My, 69 km



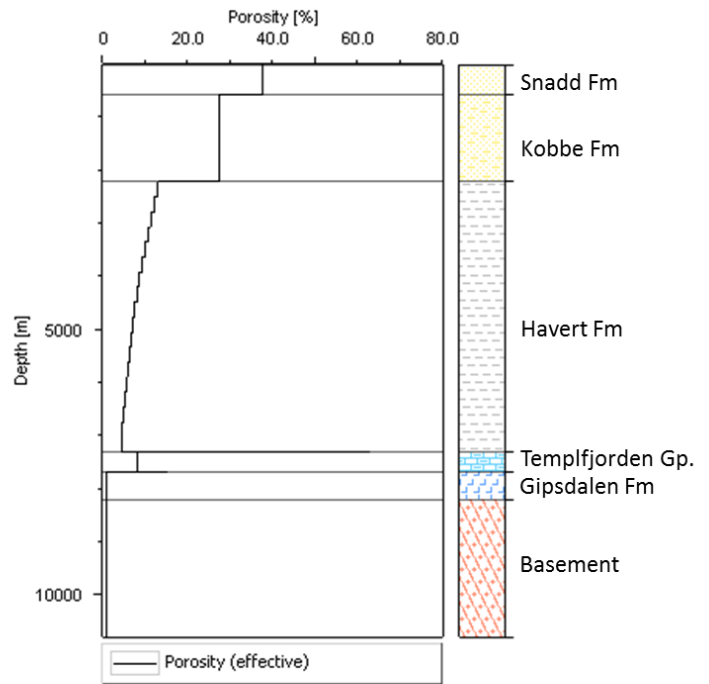
A) 152 My, 50 km



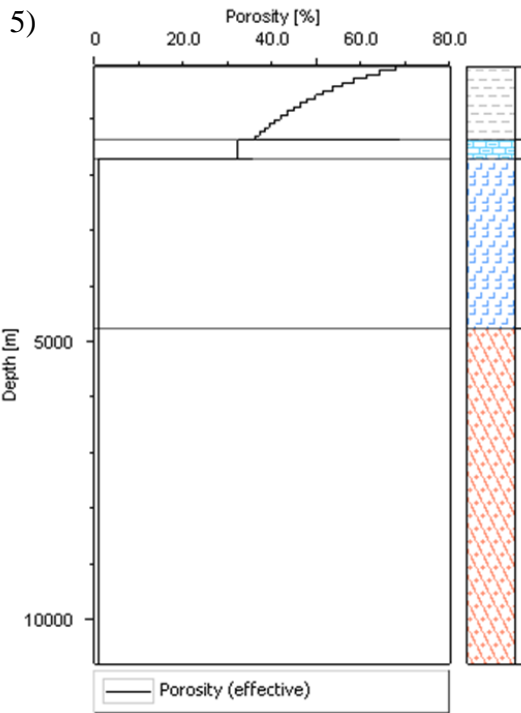
B) 152 My, 69 km



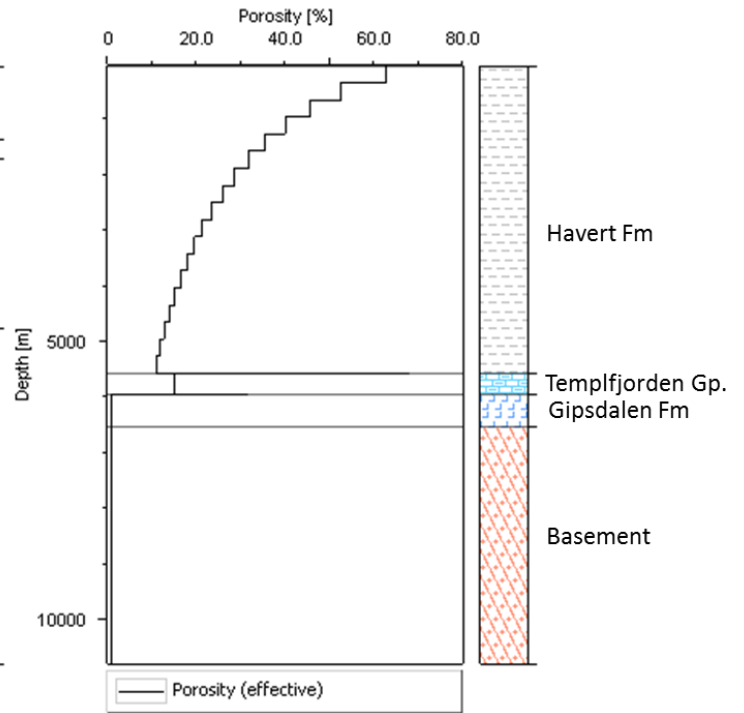
A) 208 My, 50 km



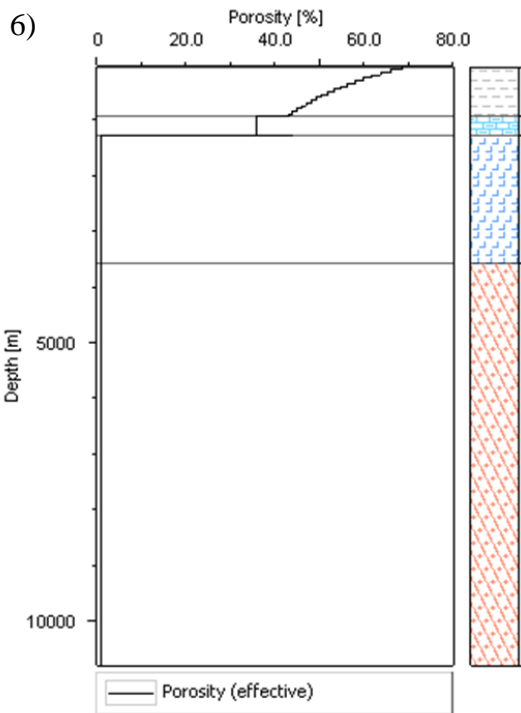
B) 208 My, 69 km



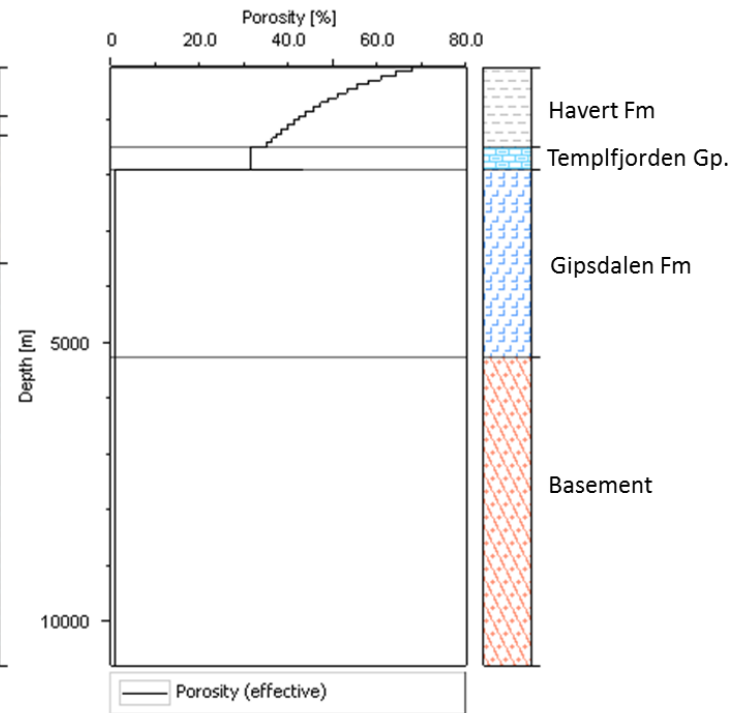
A) 220 My, 50 km



B) 220 My, 69 km



A) 250 My, 50 km



B) 250 My, 69 km

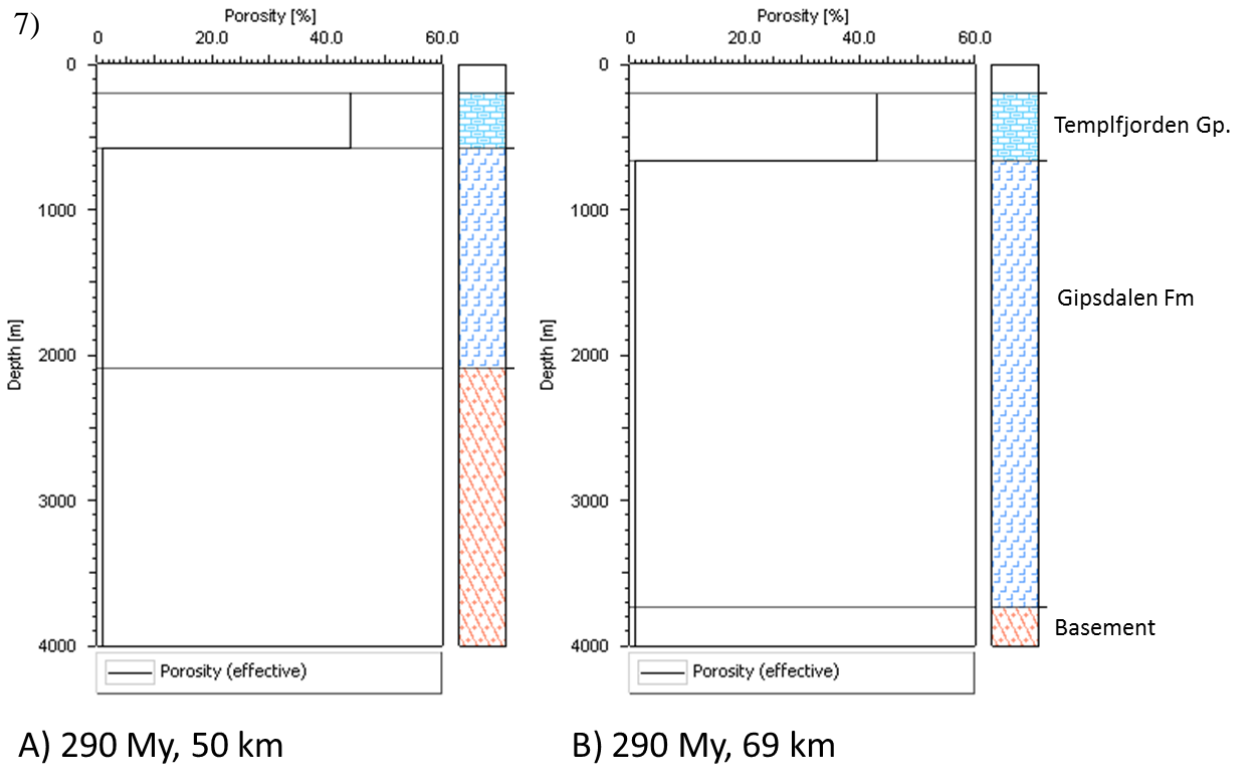
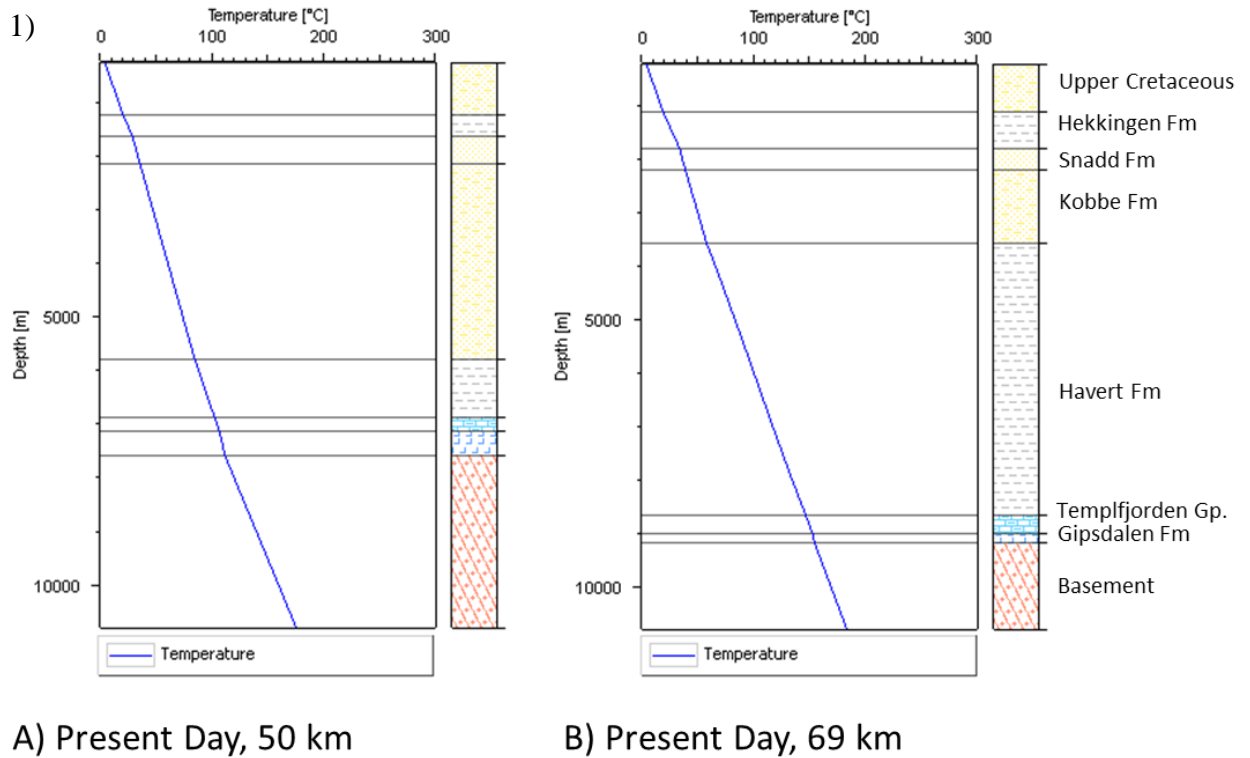
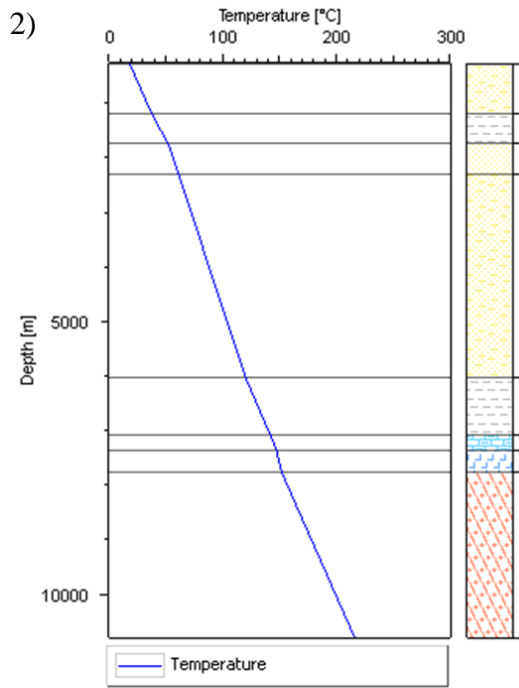


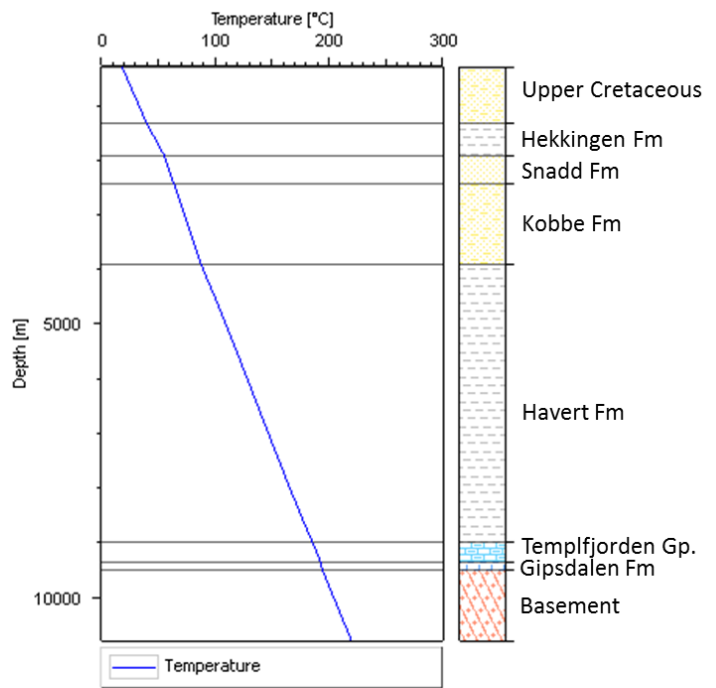
Figure 32 – At the top is present day section 1 with pseudowell positions. Below are the porosity modeled data from section 1 pseudowells. (1) Present day; (2) 100 My; (3) 152 My; (4) 208 My; (5) 220 My; (6) 250 My; (7) 290 My.

10.2. Thermal Evolution

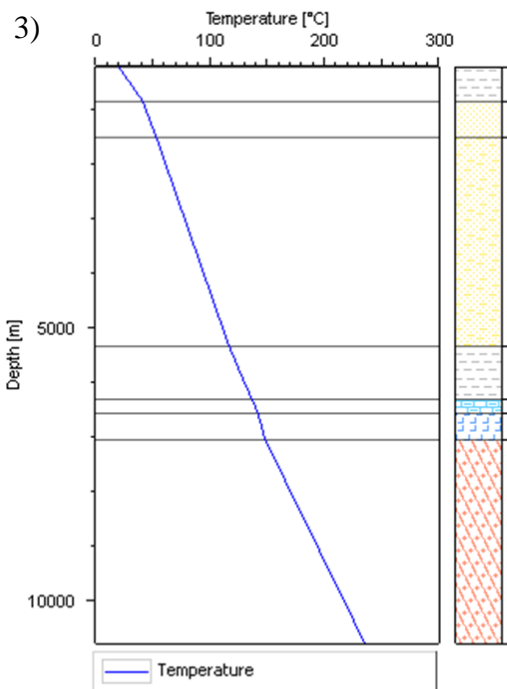




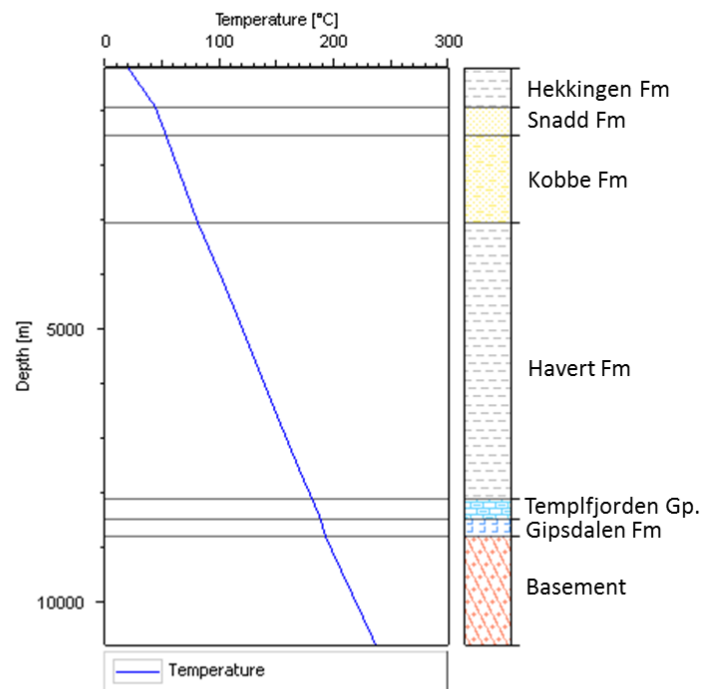
A) 100 My, 50 km



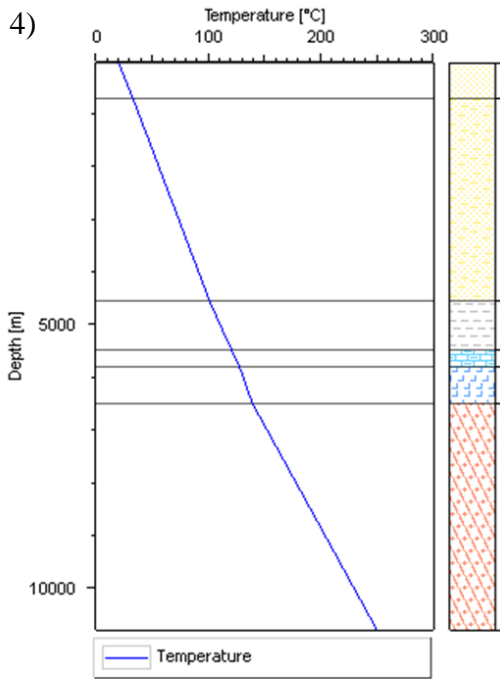
B) 100 My, 69 km



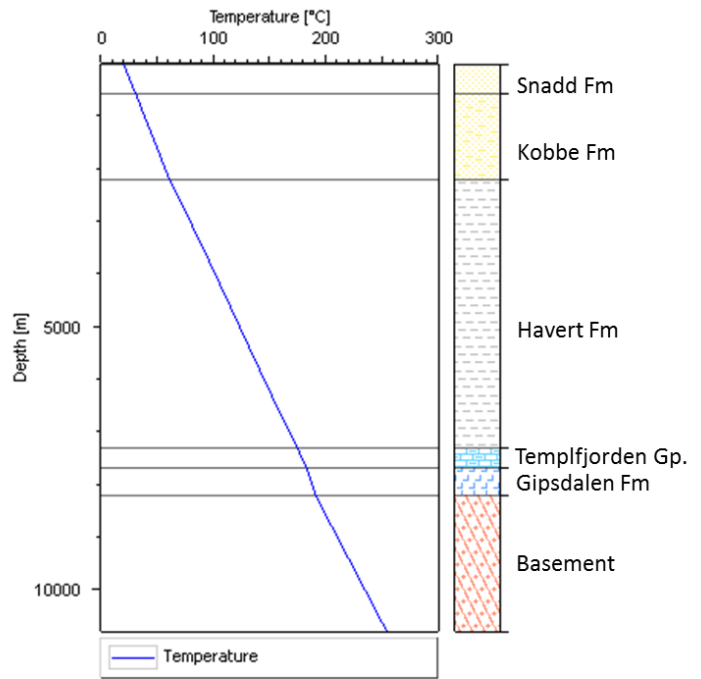
A) 152 My, 50 km



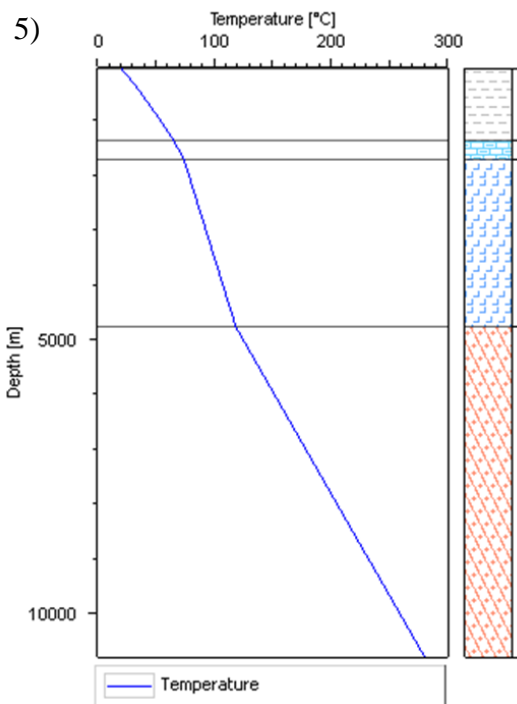
B) 152 My, 69 km



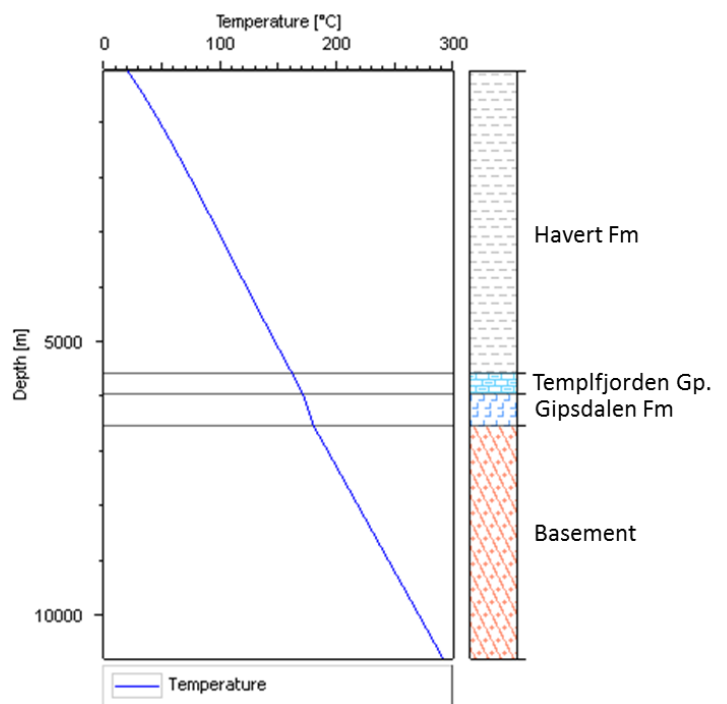
A) 208 My, 50 km



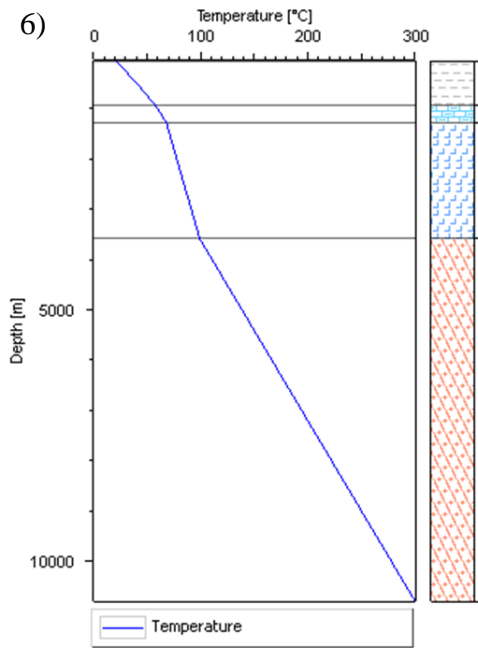
B) 208 My, 69 km



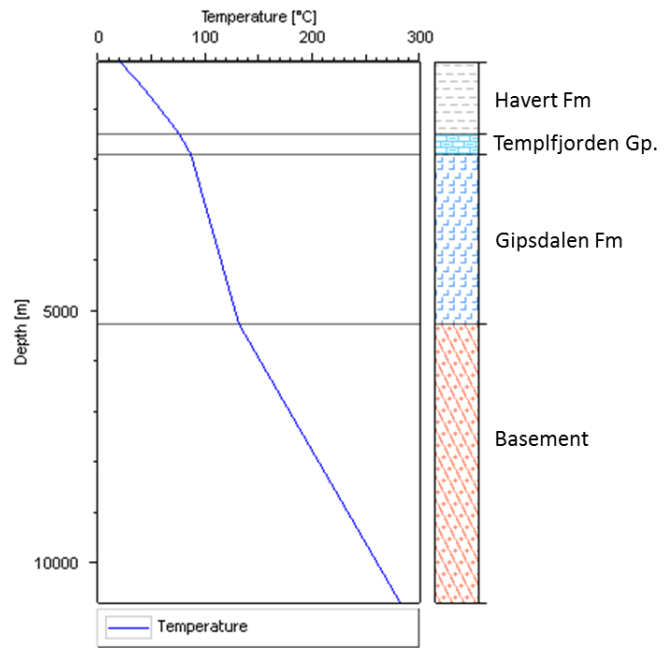
A) 220 My, 50 km



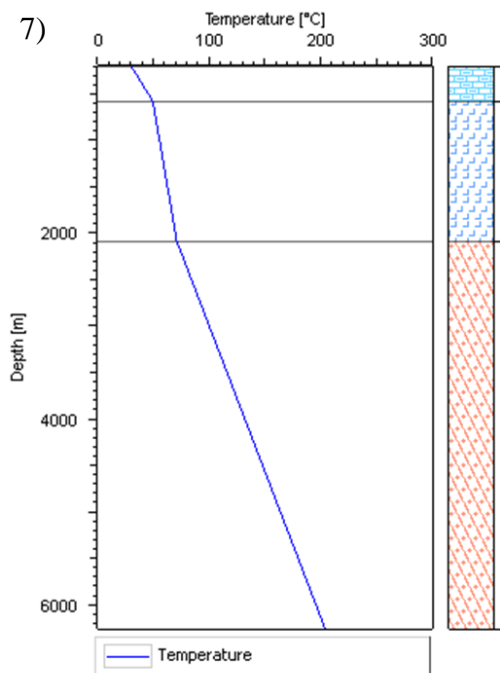
B) 220 My, 69 km



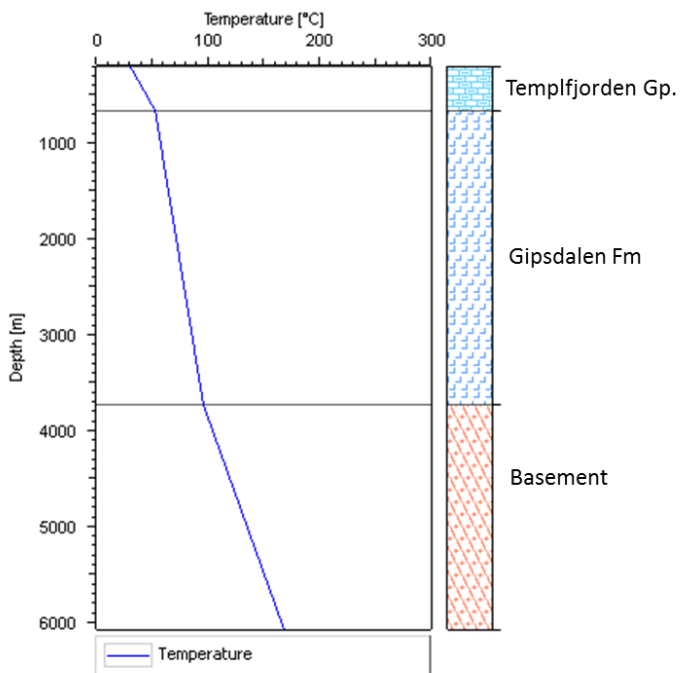
A) 250 My, 50 km



B) 250 My, 69 km



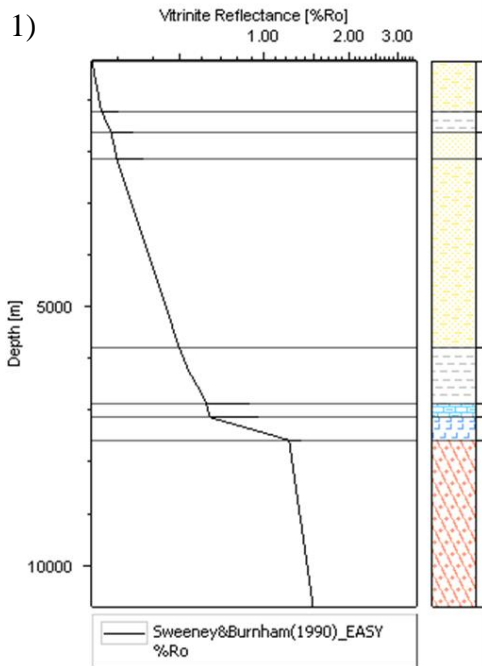
A) 290 My, 50 km



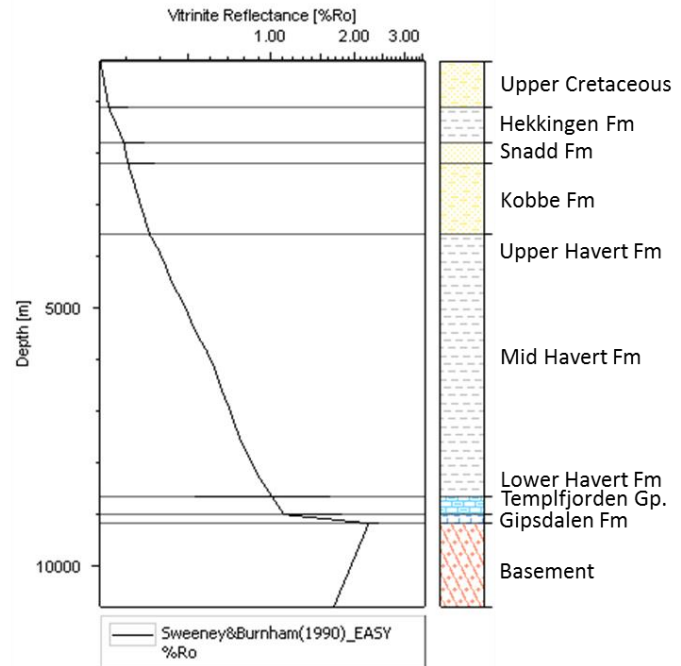
B) 290 My, 69 km

Figure 33 - Temperature modeled data from section 1 pseudowells. (1) Present day; (2) 100 My; (3) 152 My; (4) 208 My; (5) 220 My; (6) 250 My; (7) 290 My.

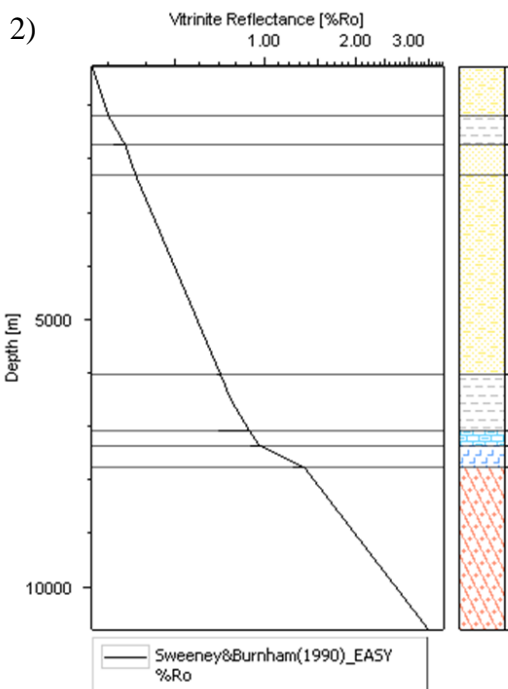
10.3. VRo Maturation Evolution



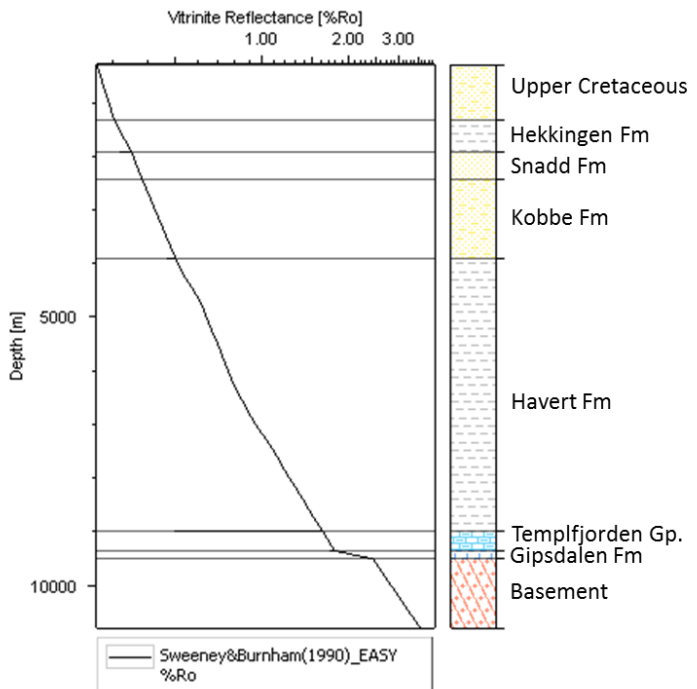
A) Present Day, 50 km



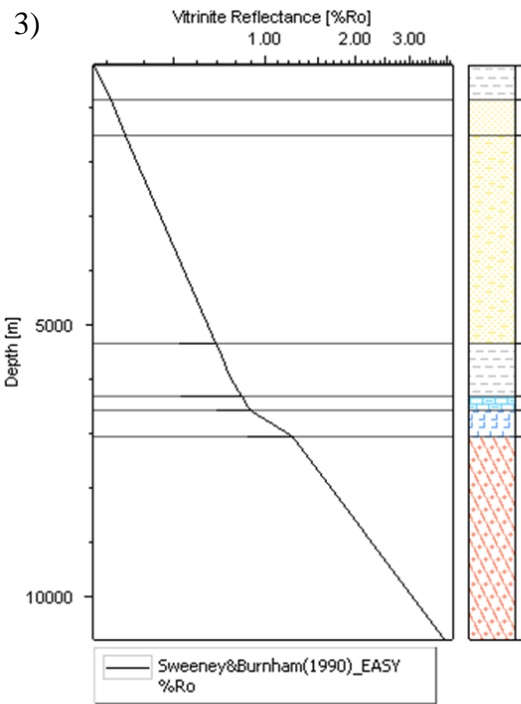
B) Present Day, 69 km



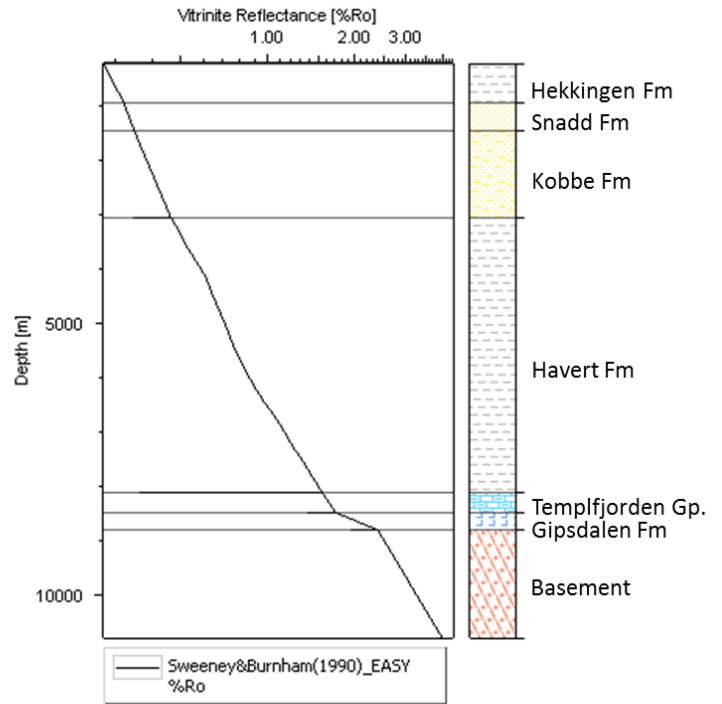
A) 100 My, 50 km



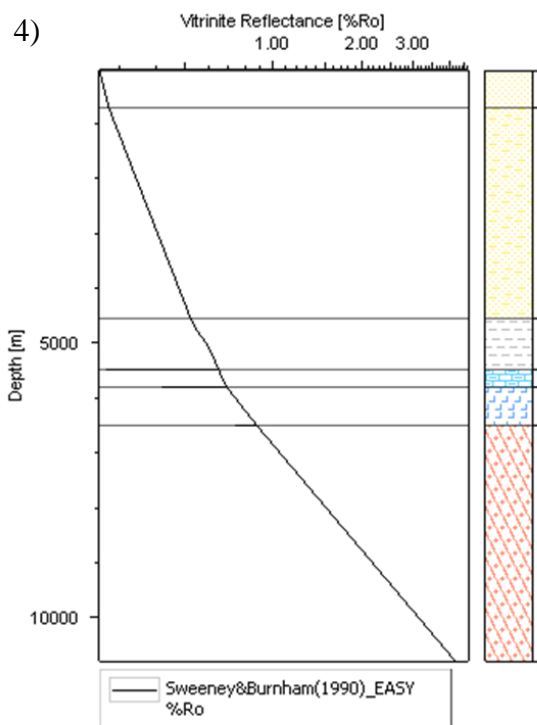
B) 100 My, 69 km



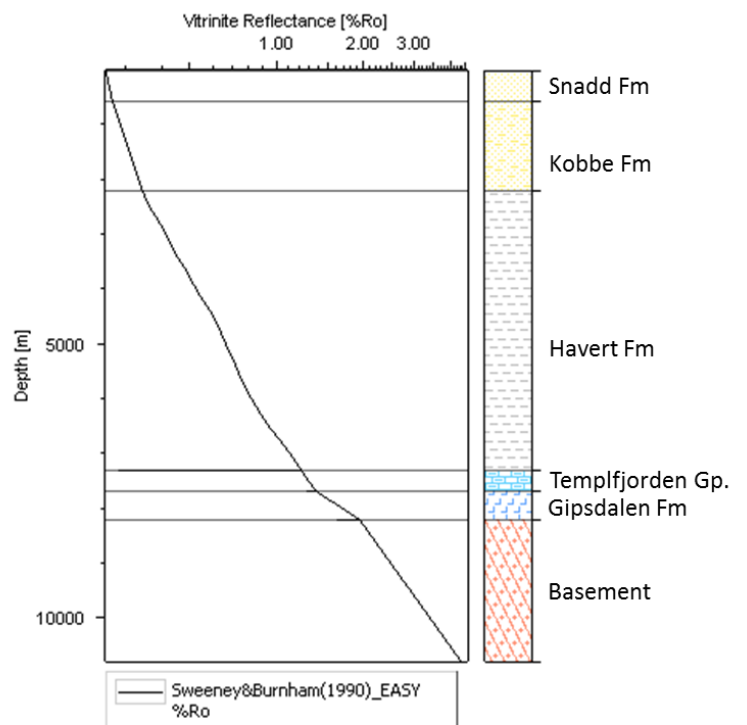
A) 152 My, 50 km



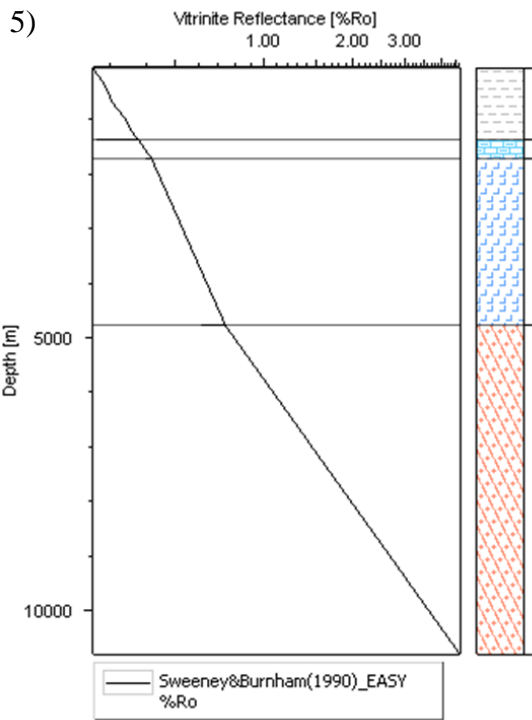
B) 152 My, 69 km



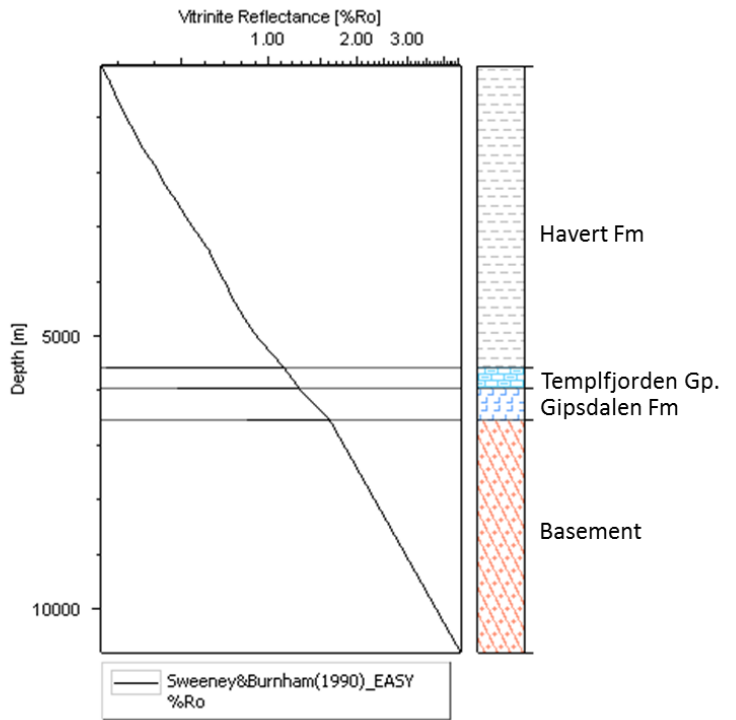
A) 208 My, 50 km



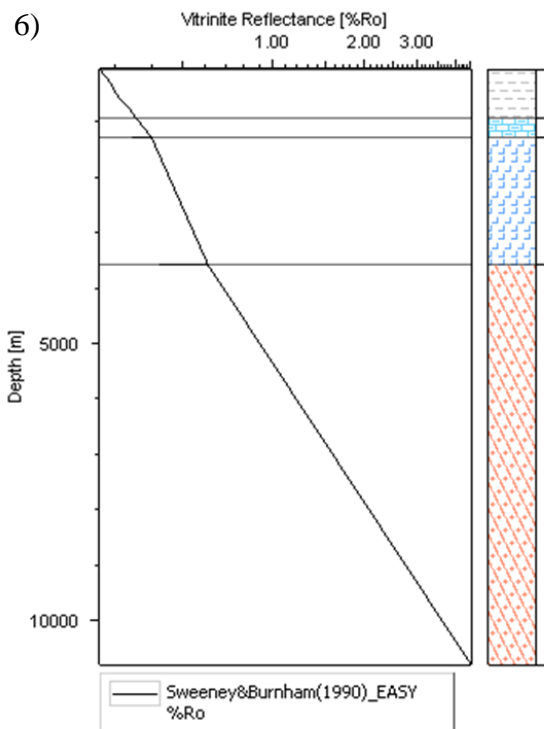
B) 208 My, 69 km



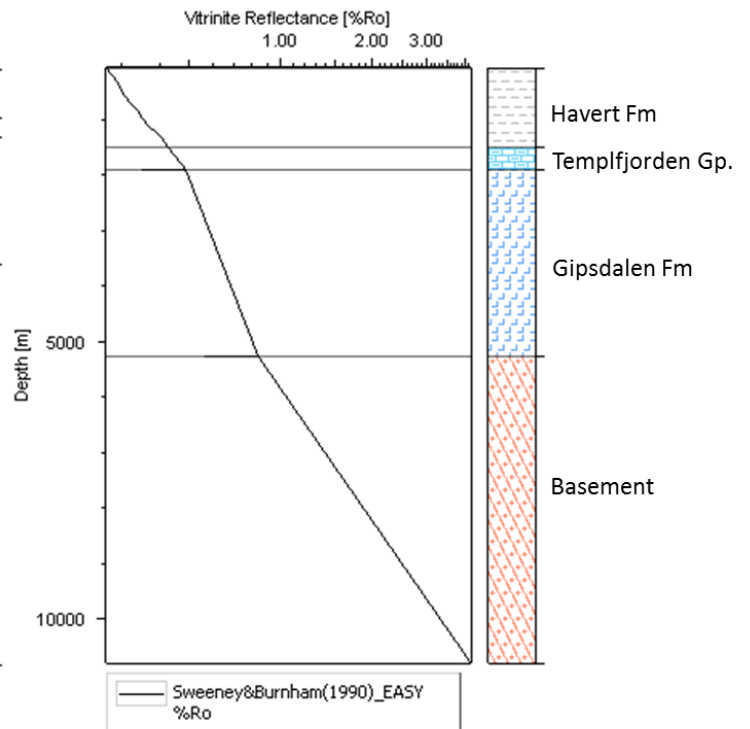
A) 220 My, 50 km



B) 220 My, 69 km



A) 250 My, 50 km



B) 250 My, 69 km

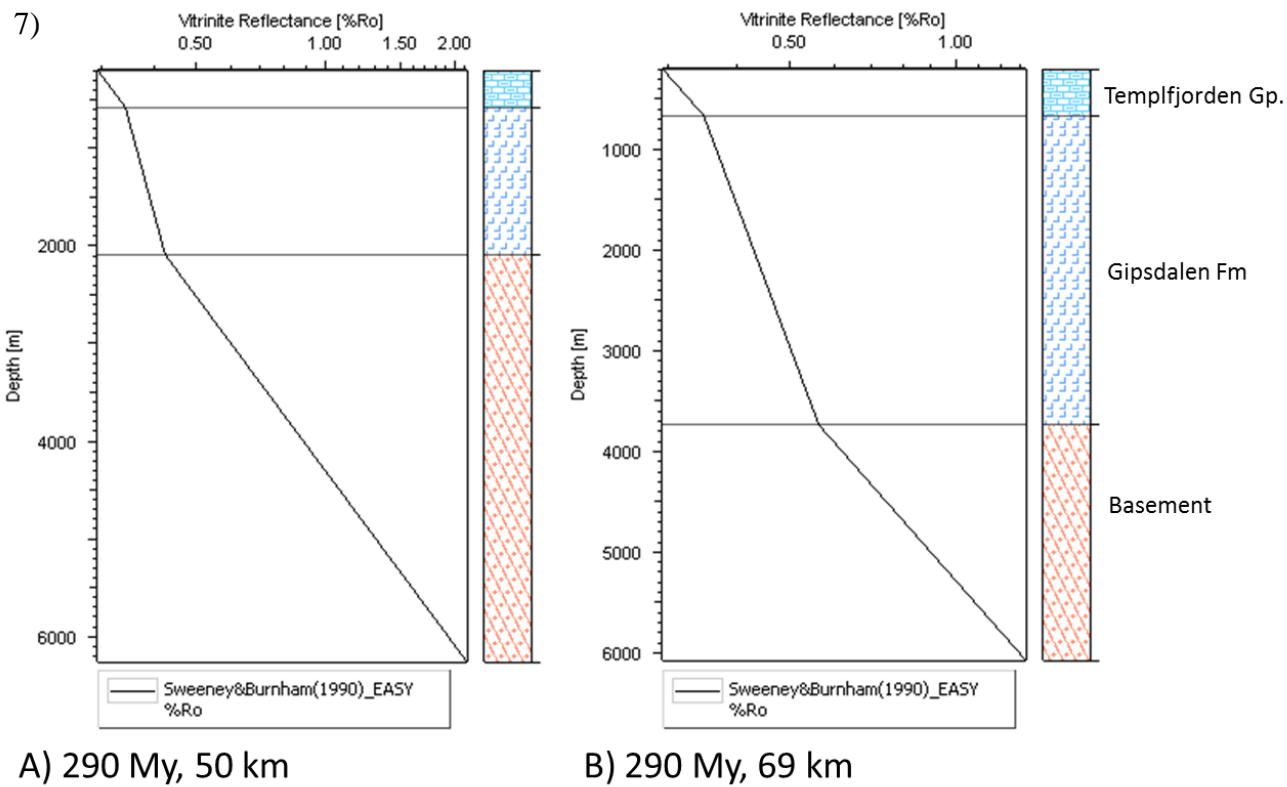
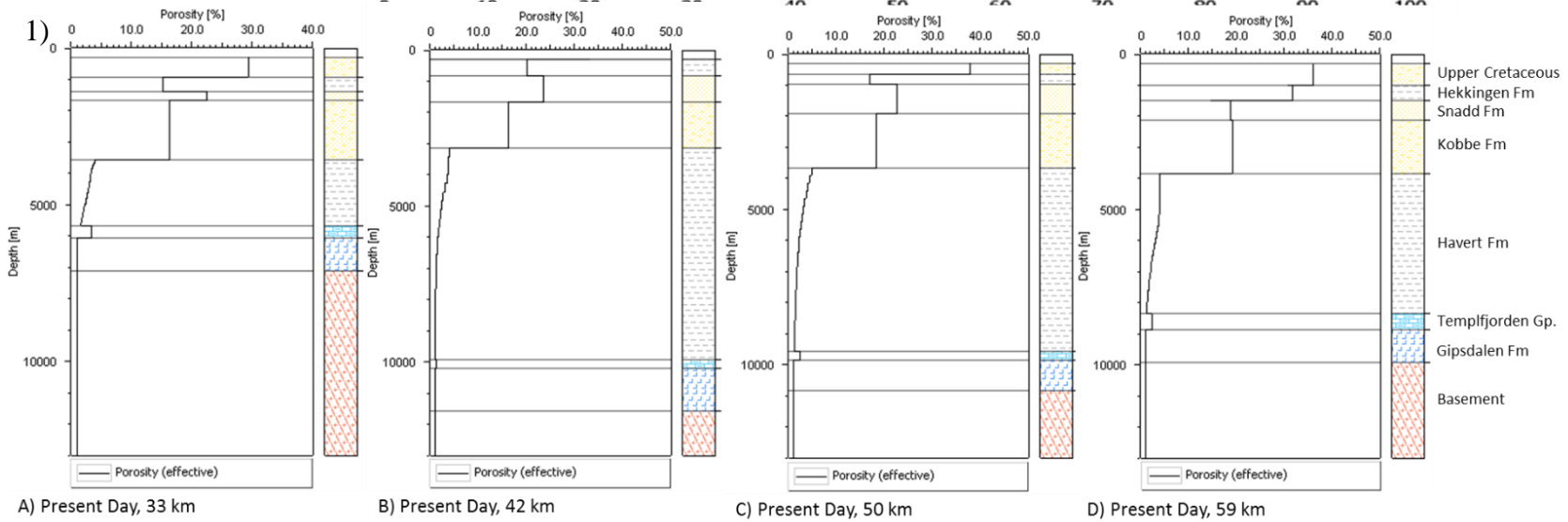
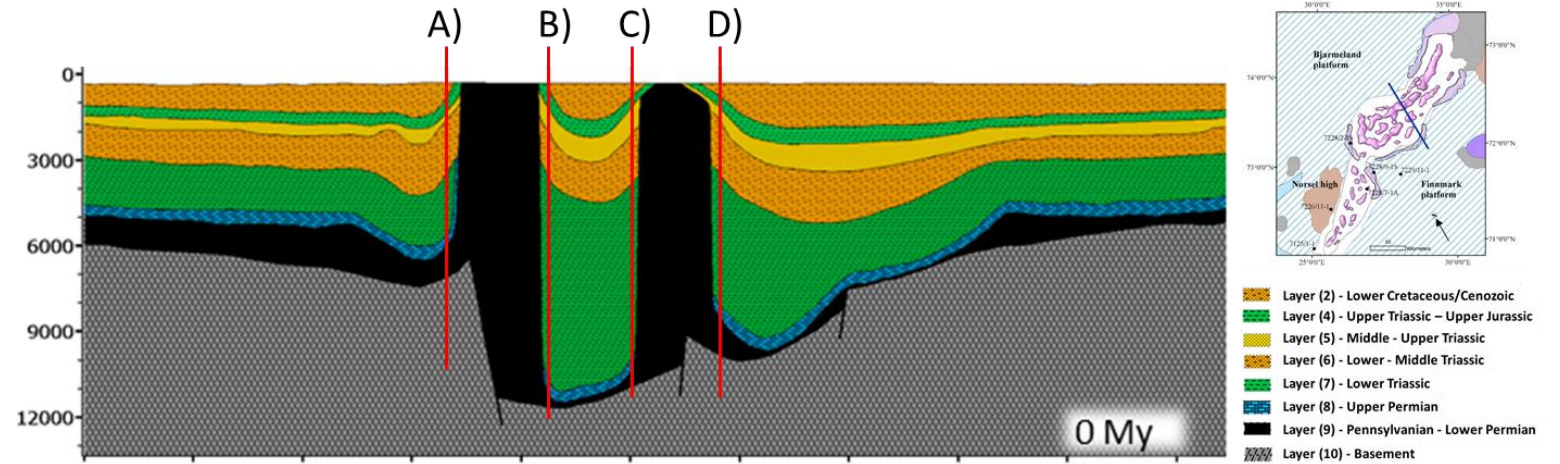
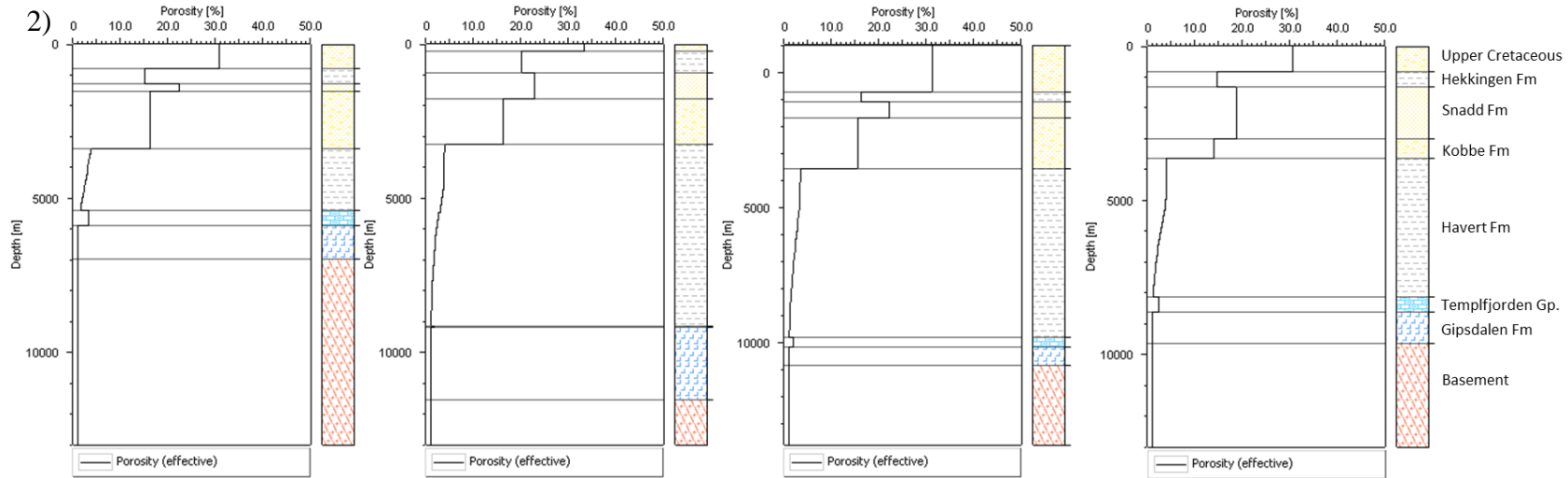


Figure 34 - Vitrinite Reflectance modeled data from section 1 pseudowells. (1) Present day; (2) 100 My; (3) 152 My; (4) 208 My; (5) 220 My; (6) 250 My; (7) 290 My.

11. Section 2

11.1. Porosity Evolution



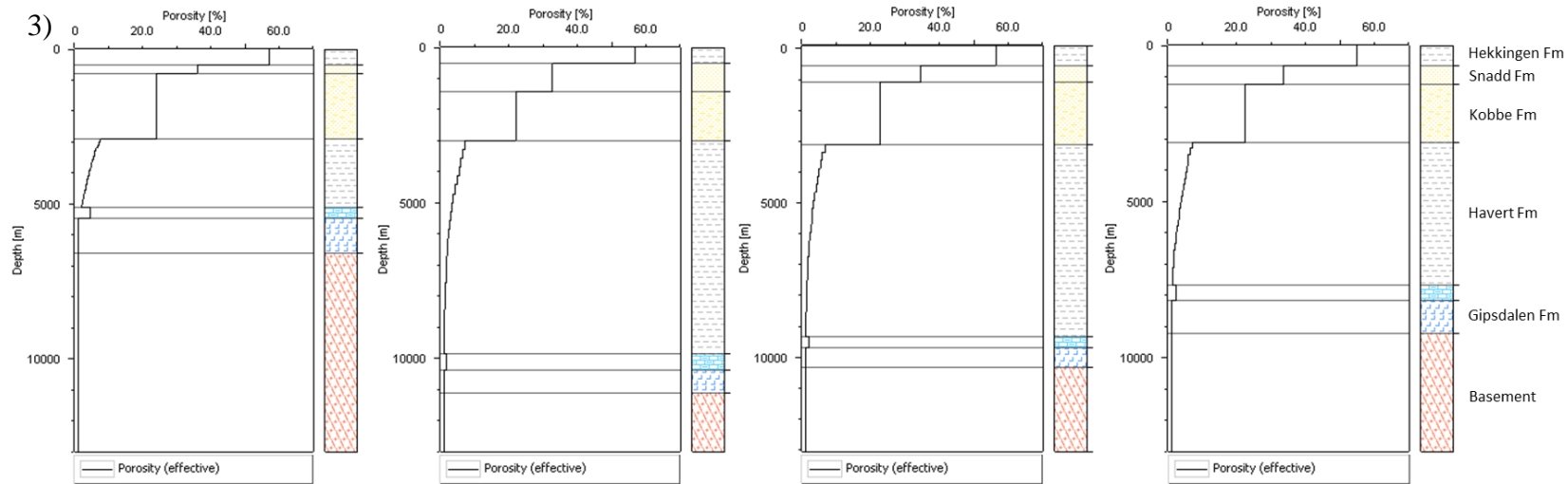


A) 100 My, 33 km

B) 100 My, 42 km

C) 100 My, 50 km

D) 100 My, 59 km

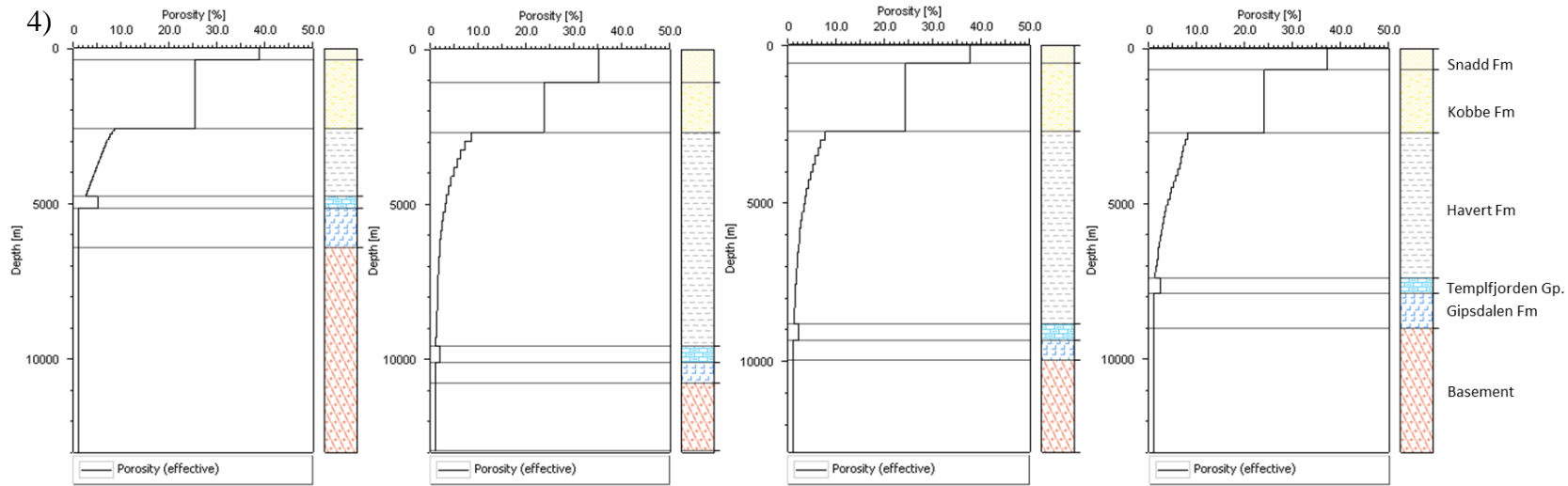


A) 152 My, 33 km

B) 152 My, 42 km

C) 152 My, 50 km

D) 152 My, 59 km

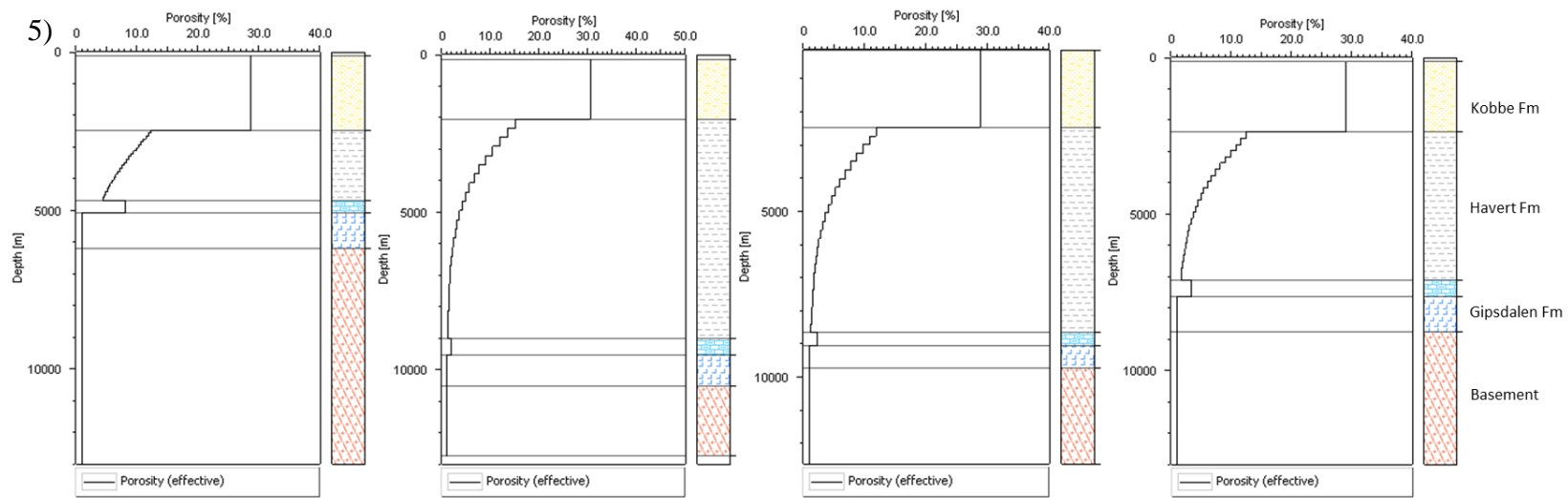


A) 208 My, 33 km

B) 208 My, 42 km

C) 208 My, 50 km

D) 208 My, 59 km



A) 220 My, 33 km

B) 220 My, 42 km

C) 220 My, 50 km

D) 220 My, 59 km

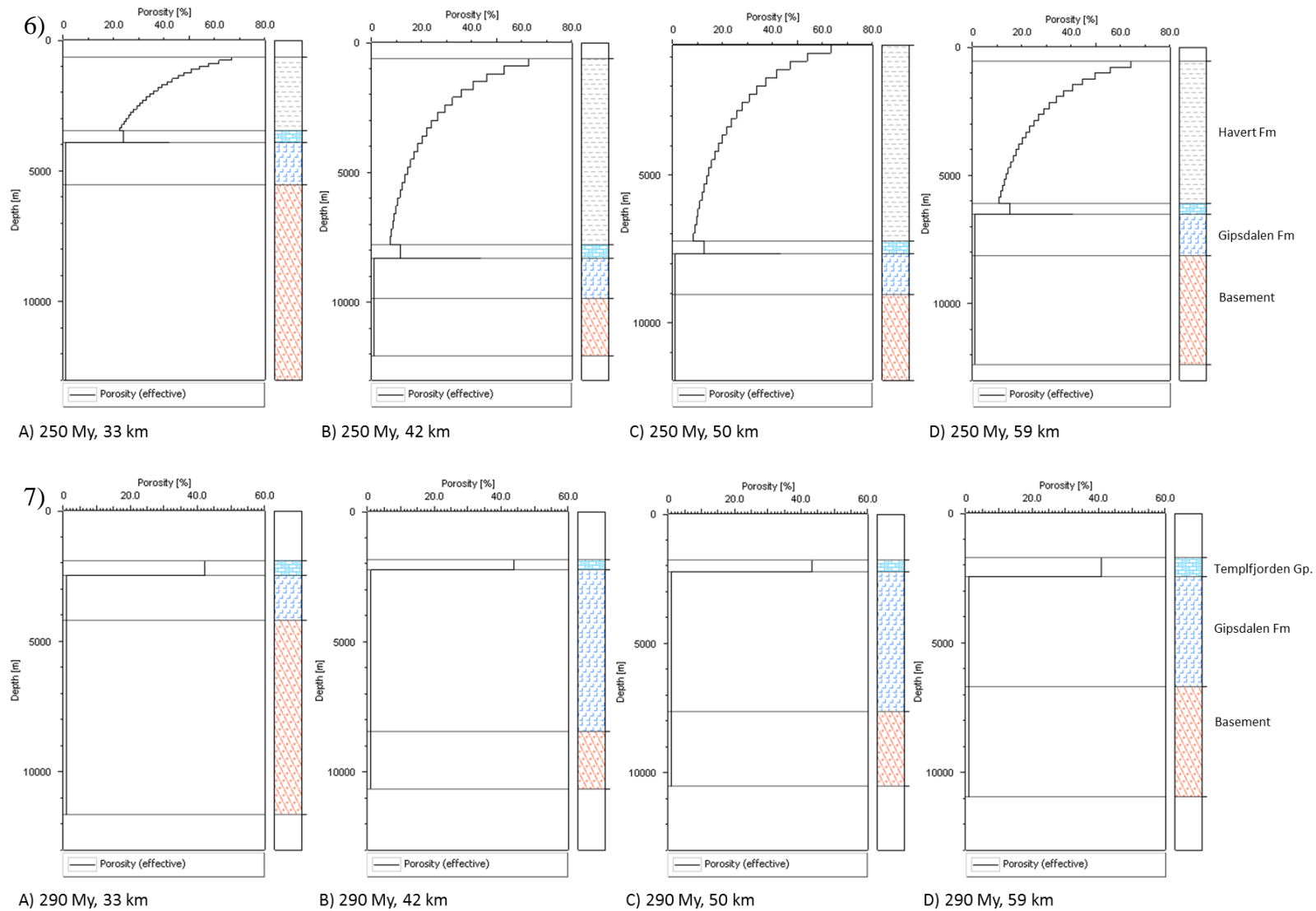
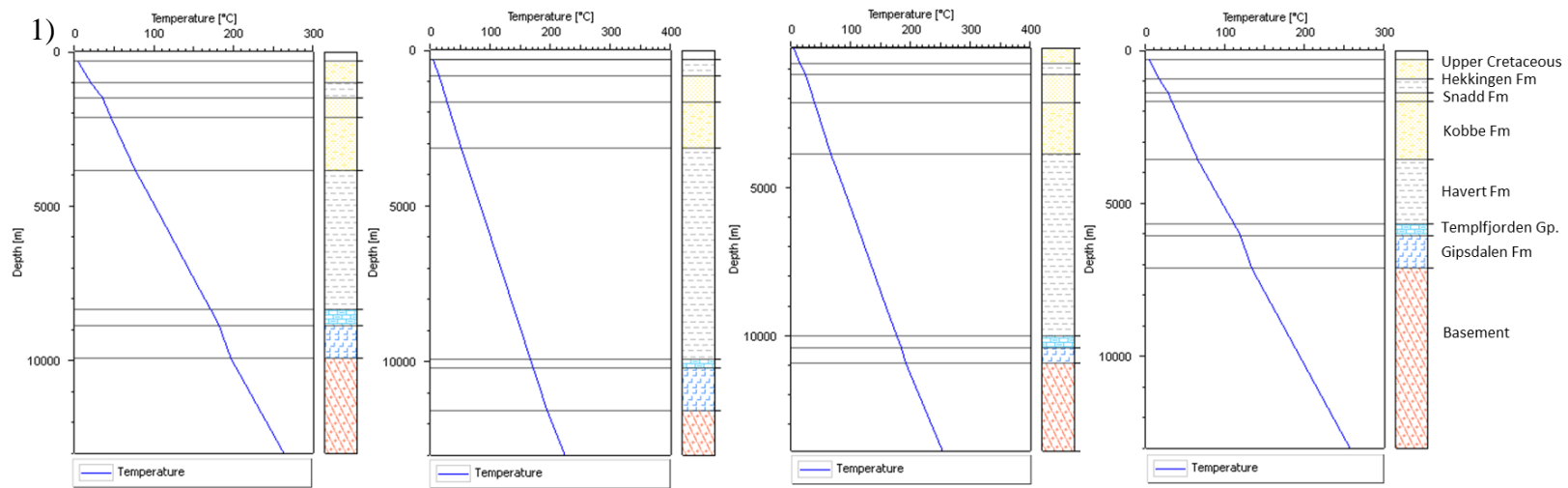


Figure 35 – At the top is present day section 2 with pseudowell positions. Below are the Porosity modeled data from section 2 pseudowells. (1) Present day; (2) 100 My; (3) 152 My; (4) 208 My; (5) 220 My); (6) 250 My; (7) 290 My.

11.2. Temperature Evolution

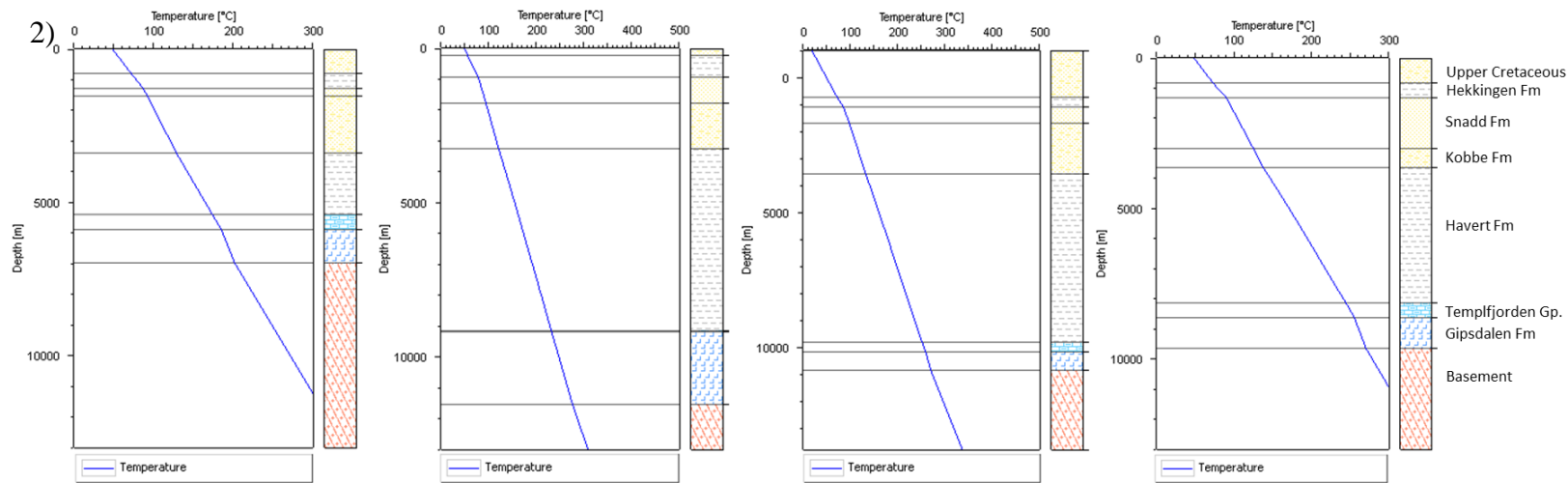


A) Present Day, 33 km

B) Present Day, 42 km

C) Present Day, 50 km

D) Present Day, 59 km

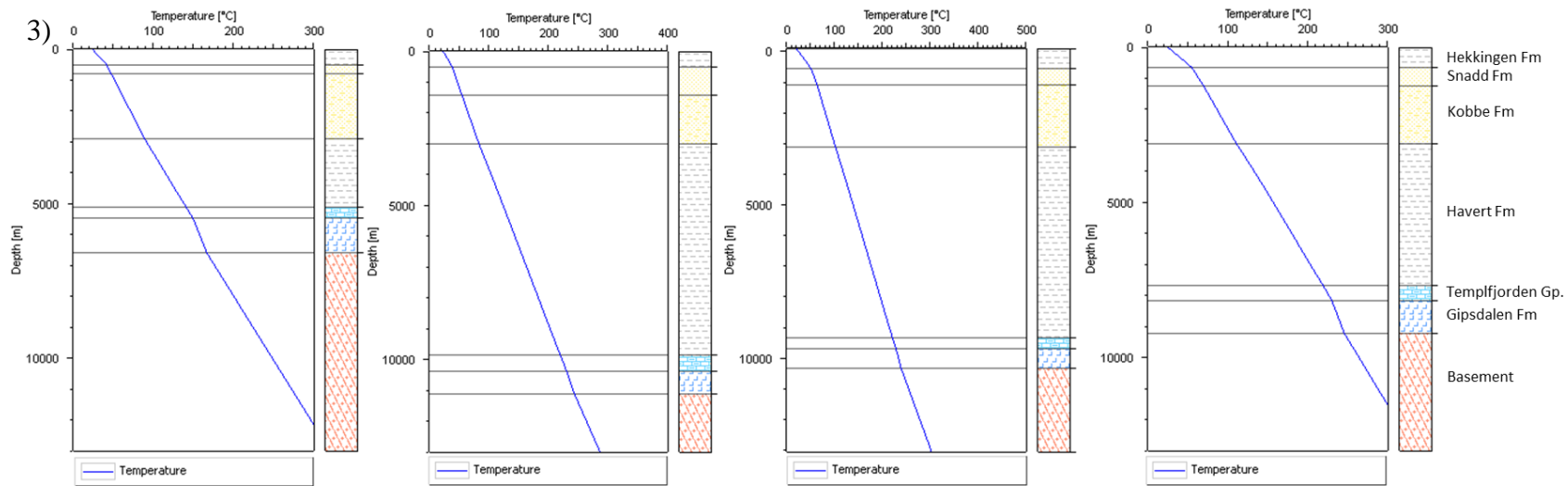


A) 100 My, 33 km

B) 100 My, 42 km

C) 100 My, 50 km

D) 100 My, 59 km

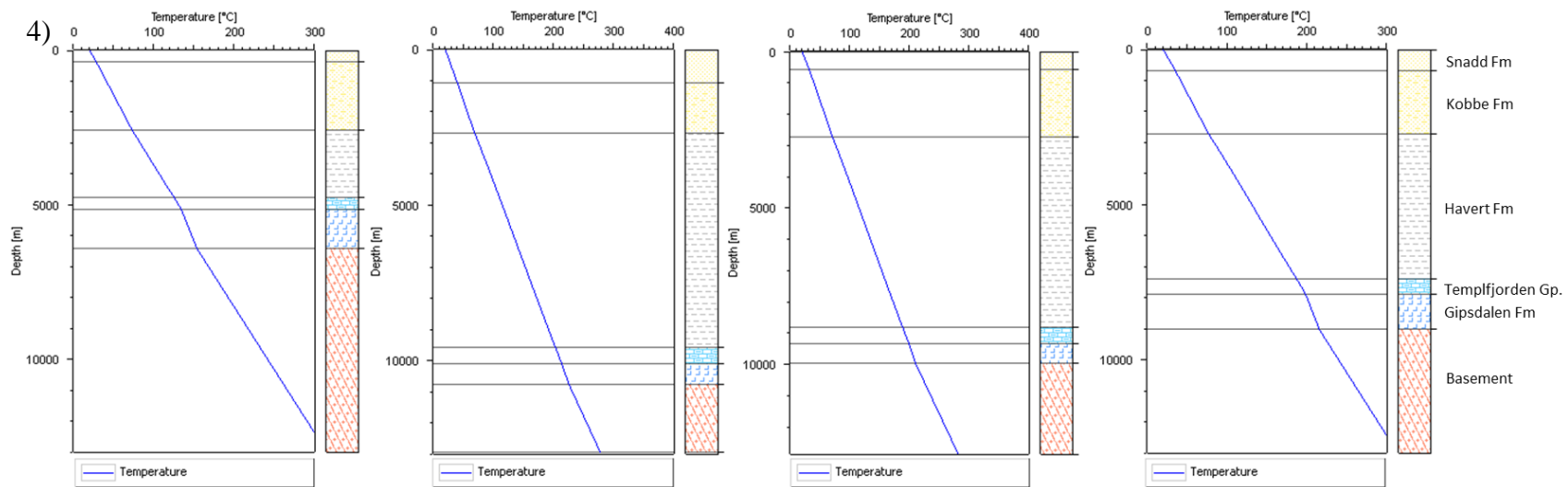


A) 152 My, 33 km

B) 152 My, 42 km

C) 152 My, 50 km

D) 152 My, 59 km

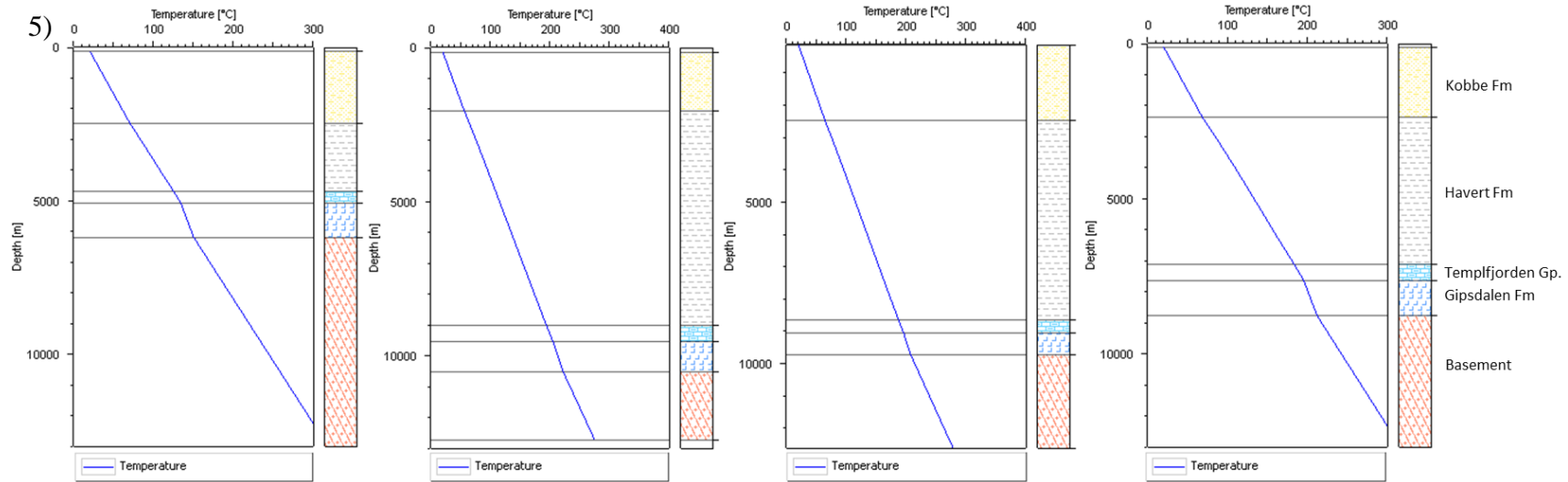


A) 208 My, 33 km

B) 208 My, 42 km

C) 208 My, 50 km

D) 208 My, 59 km

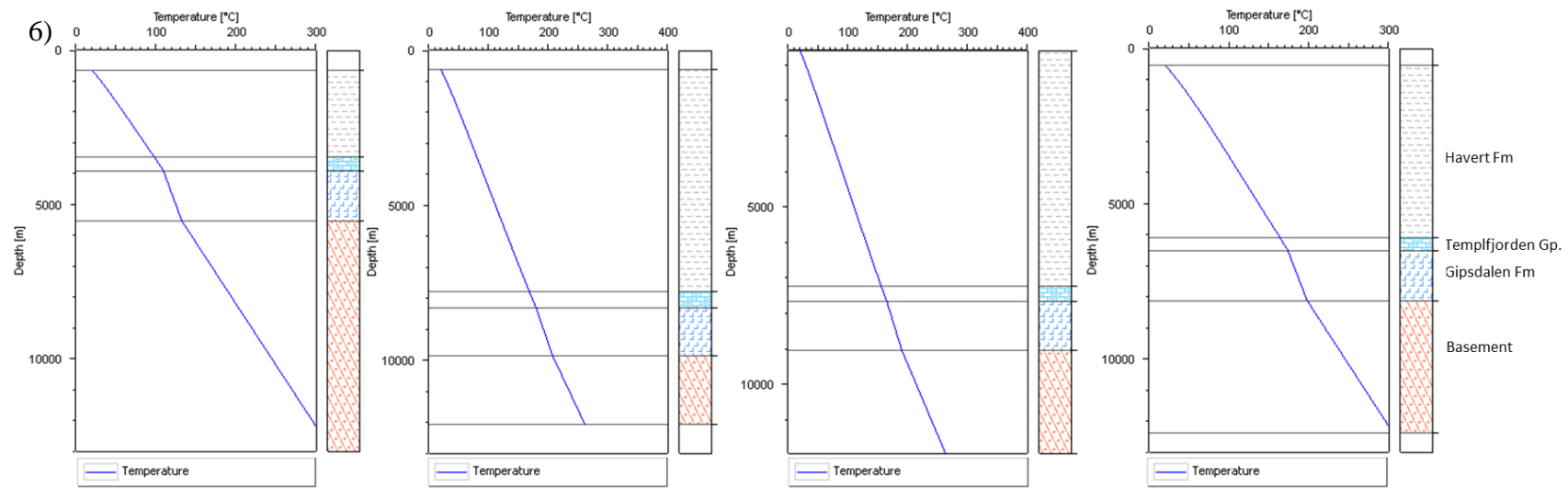


A) 220 My, 33 km

B) 220 My, 42 km

C) 220 My, 50 km

D) 220 My, 59 km



A) 250 My, 33 km

B) 250 My, 42 km

C) 250 My, 50 km

D) 250 My, 59 km

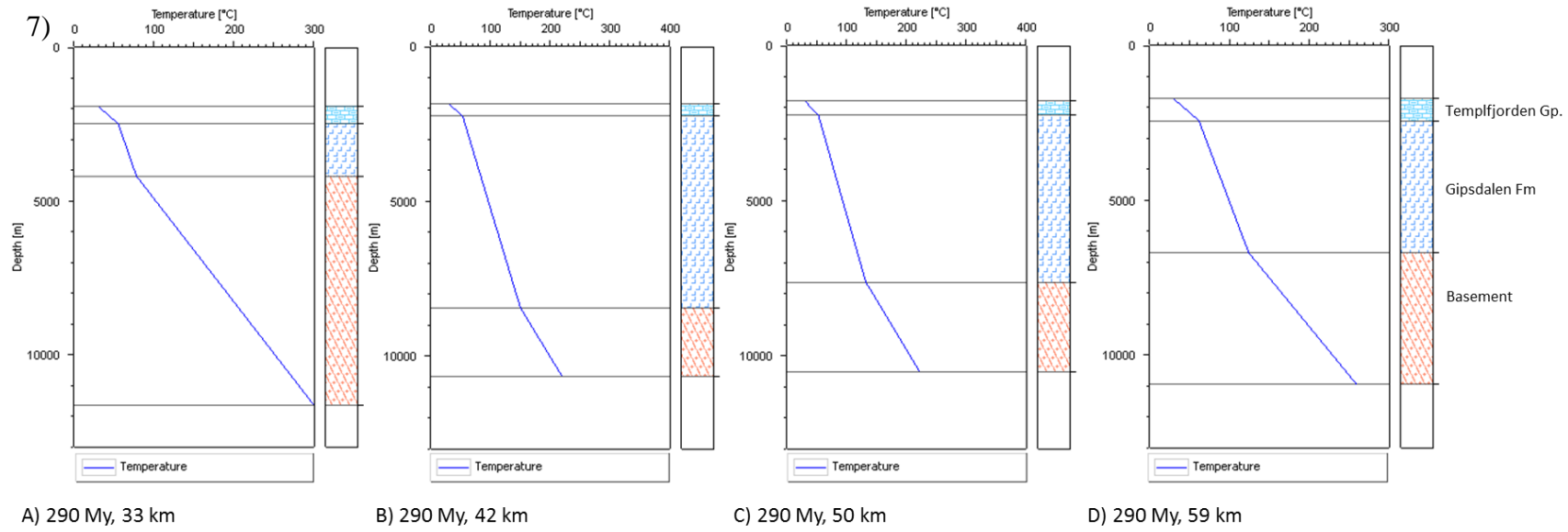
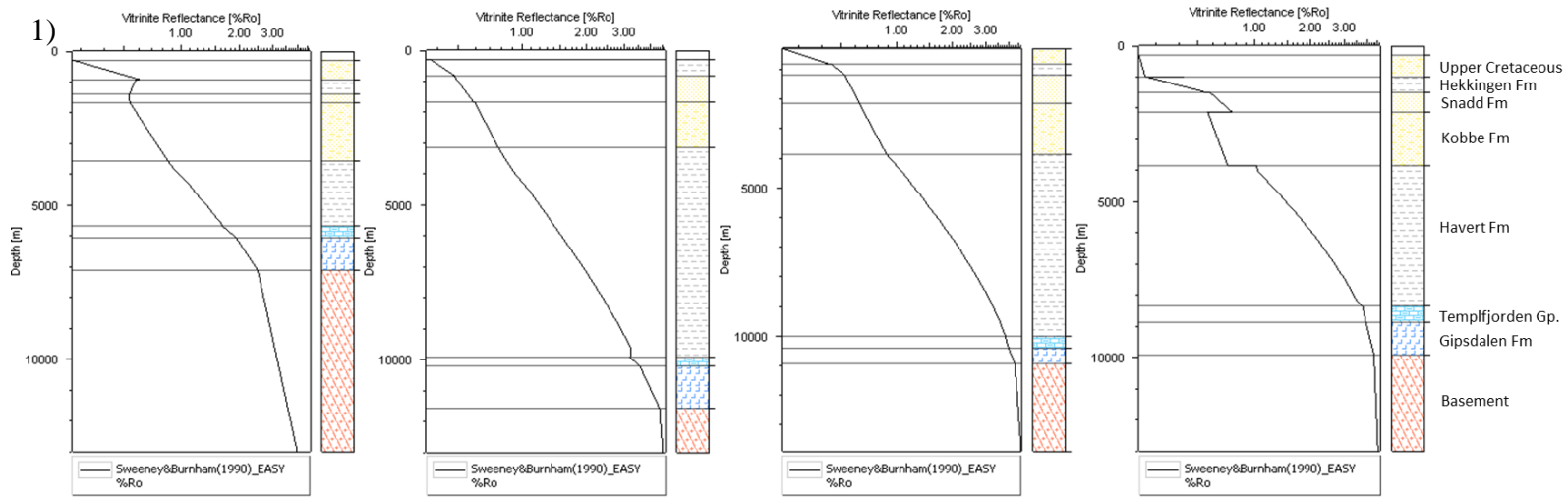


Figure 36 - Temperature modeled data from section 2 pseudowells. (1) Present day; (2) 100 My; (3) 152 My; (4) 208 My; (5) 220 My; (6) 250 My; (7) 290 My.

11.3. VRo Maturation Evolution

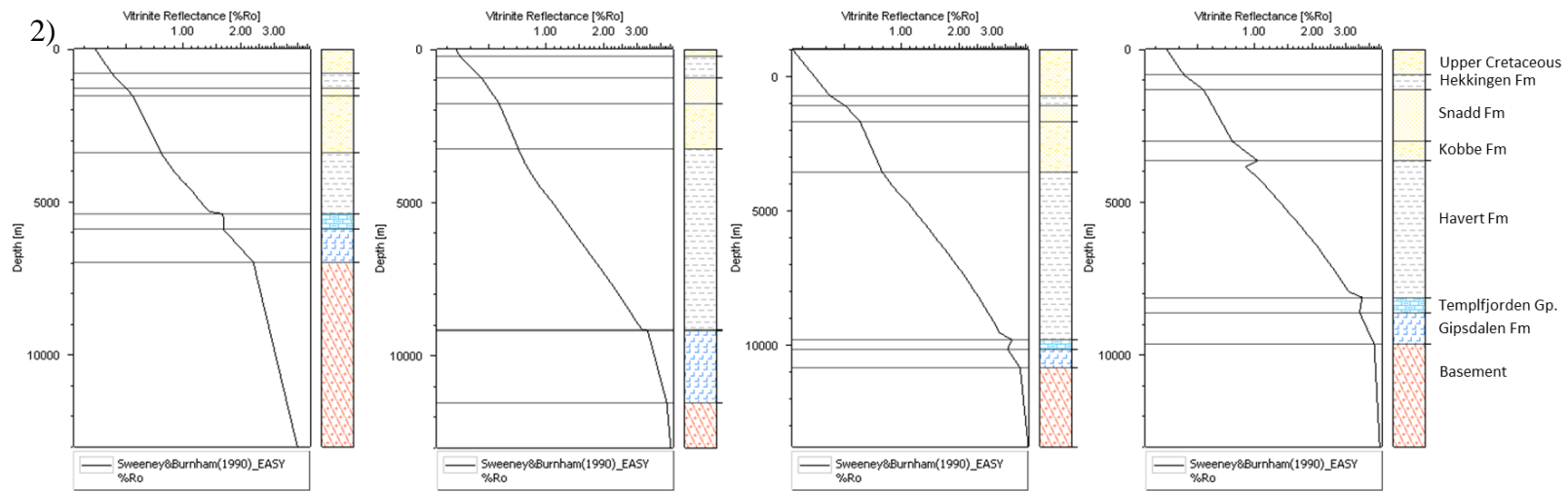


A) Present Day, 33 km

B) Present Day, 42 km

C) Present Day, 50 km

D) Present Day, 59 km

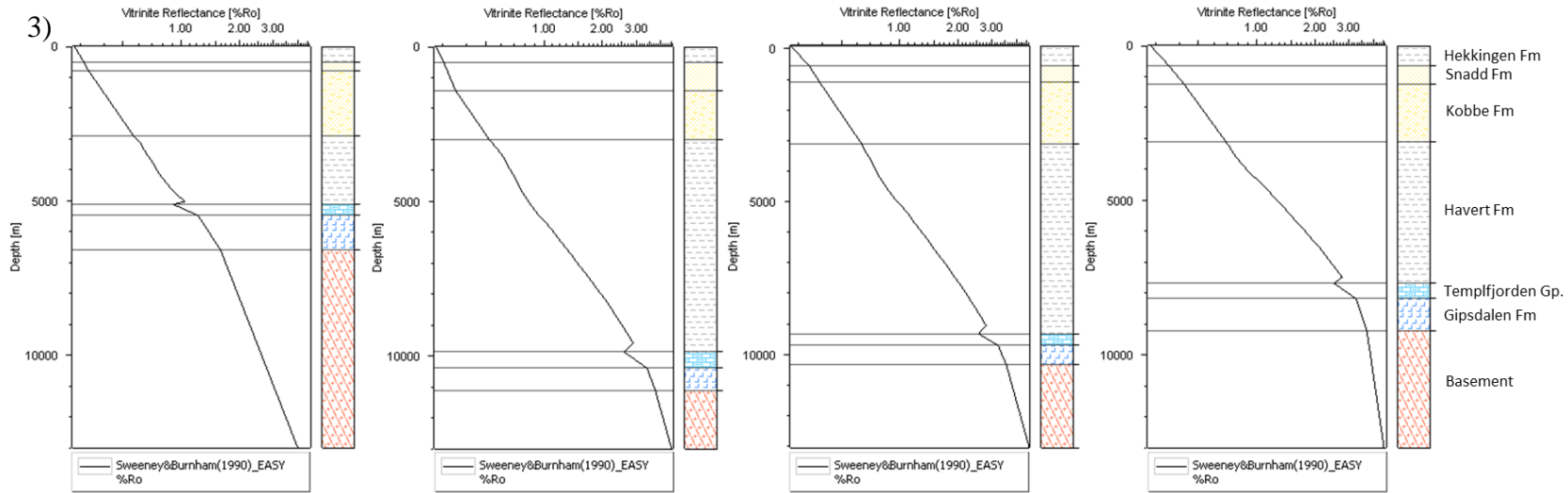


A) 100 My, 33 km

B) 100 My, 42 km

C) 100 My, 50 km

D) 100 My, 59 km

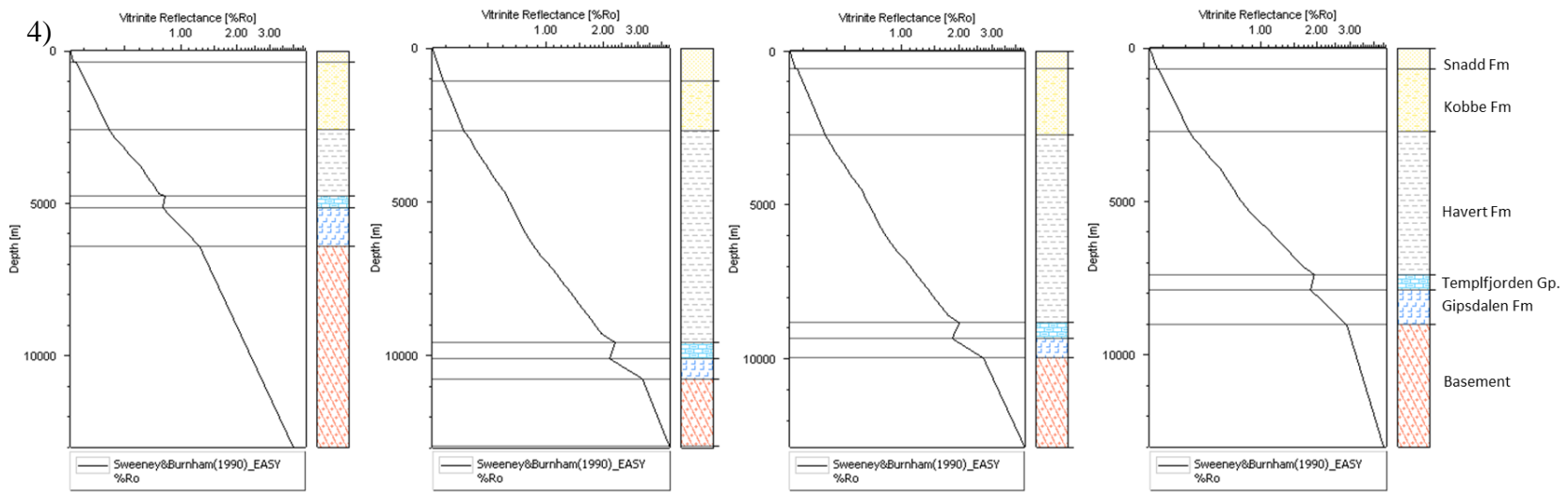


A) 152 My, 33 km

B) 152 My, 42 km

C) 152 My, 50 km

D) 152 My, 59 km

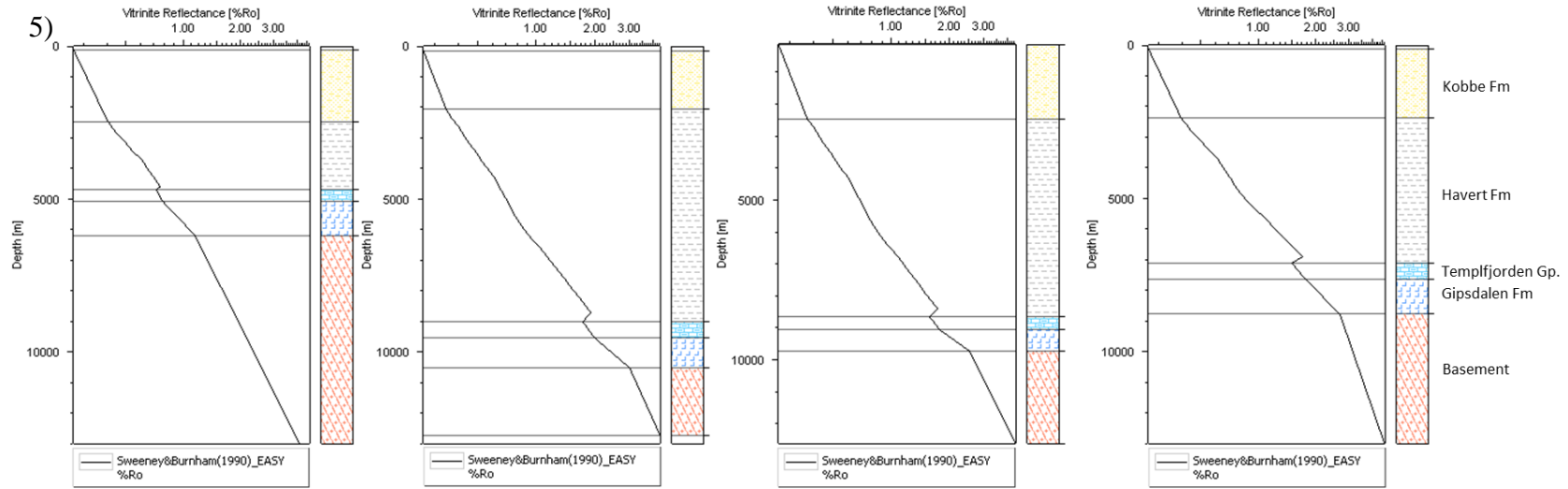


A) 208 My, 33 km

B) 208 My, 42 km

C) 208 My, 50 km

D) 208 My, 59 km

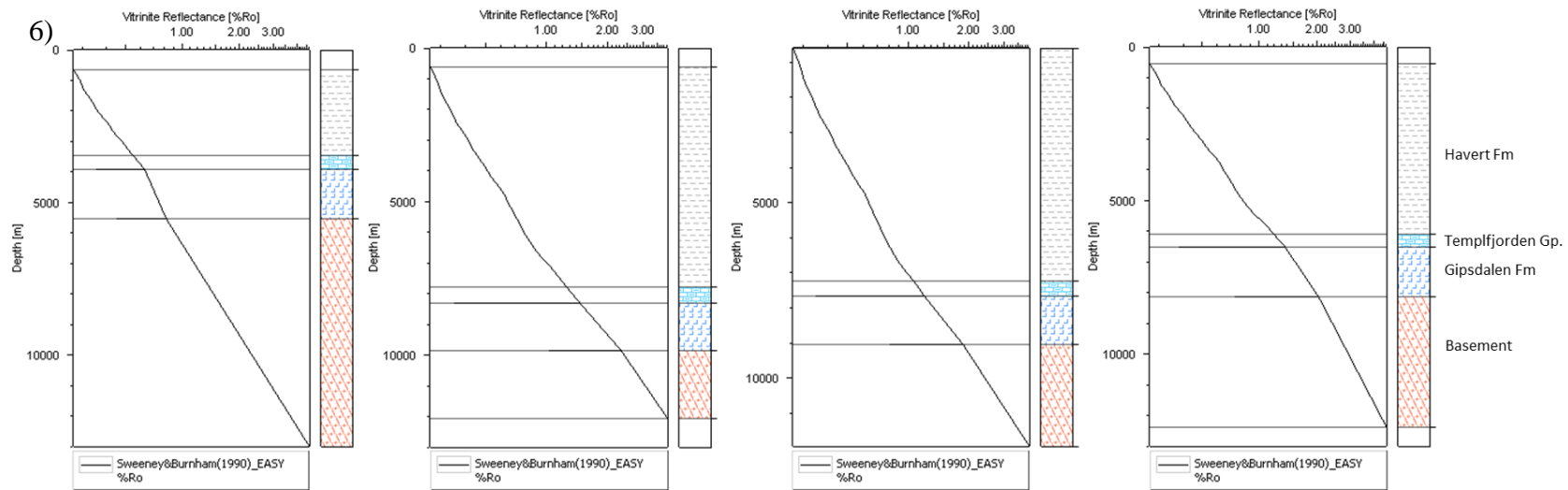


A) 220 My, 33 km

B) 220 My, 42 km

C) 220 My, 50 km

D) 220 My, 59 km



A) 250 My, 33 km

B) 250 My, 42 km

C) 250 My, 50 km

D) 250 My, 59 km

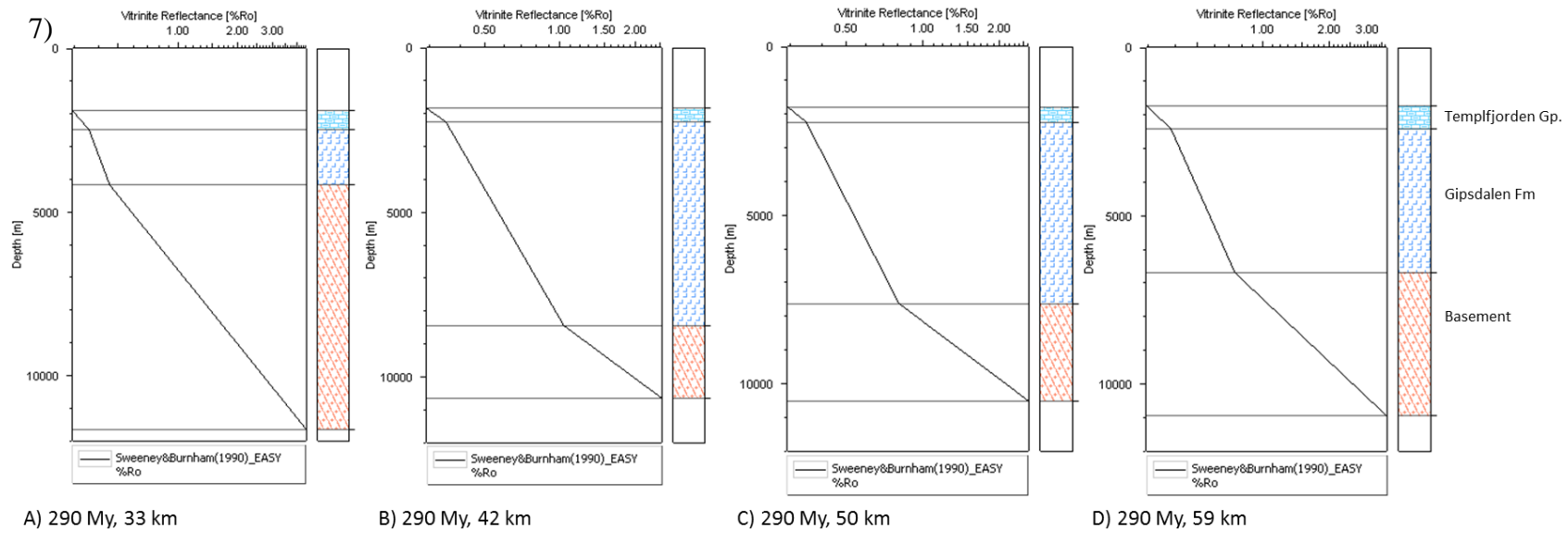


Figure 37 – Vitrinite Reflectance modeled data from section 2 pseudowells. (1) Present day; (2) 100 My; (3) 152 My; (4) 208 My; (5) 220 My; (6) 250 My; (7) 290 My.

12. Reservoir rock temperature/time plots

12.1. Section 1

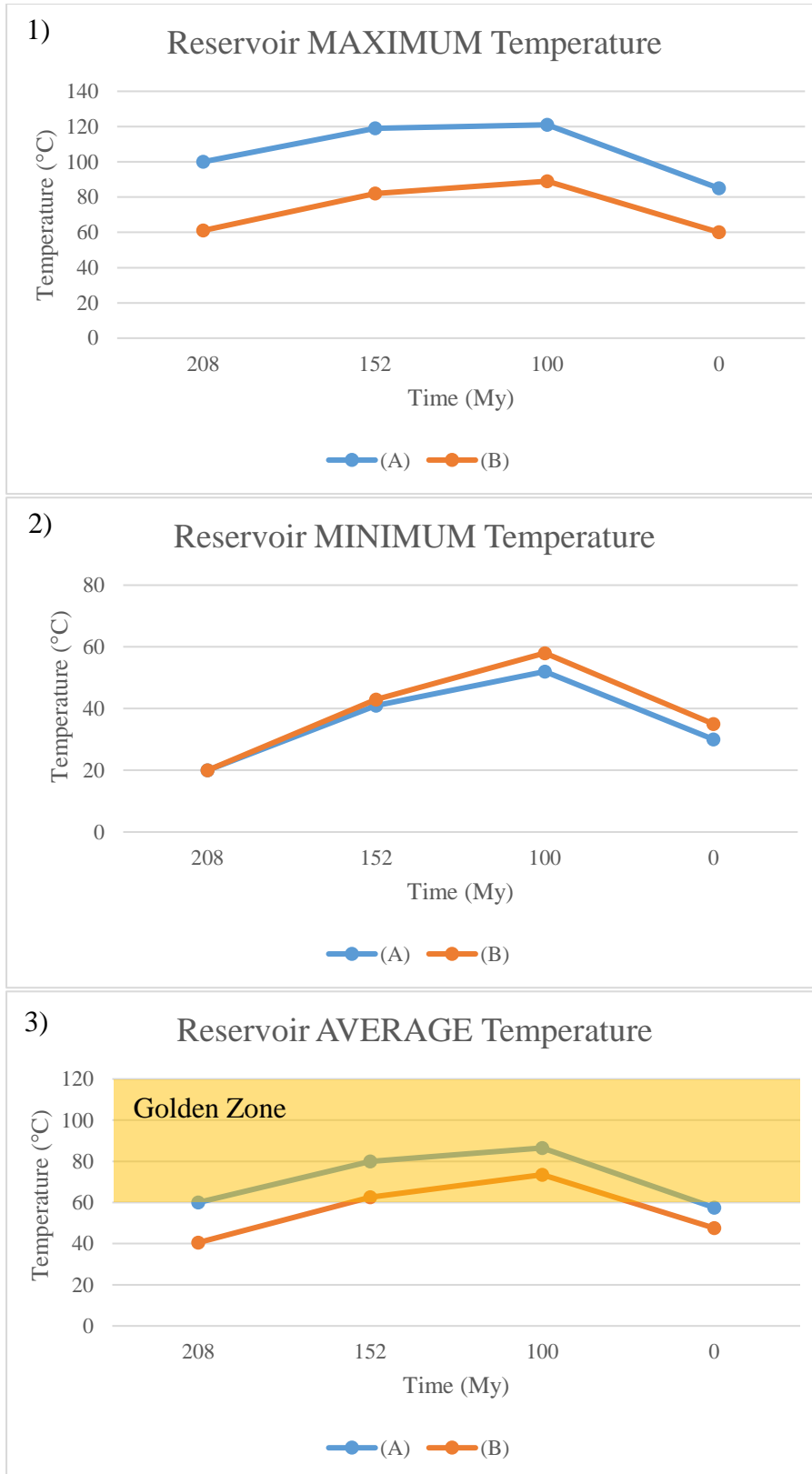


Figure 38 - Reservoir temperature to time plots for section 2. (1) Maximum temperature values of the reservoir units; (2) Minimum temperature values of the reservoir units; (3) Average temperature values of the reservoir units.

12.2. Section 2

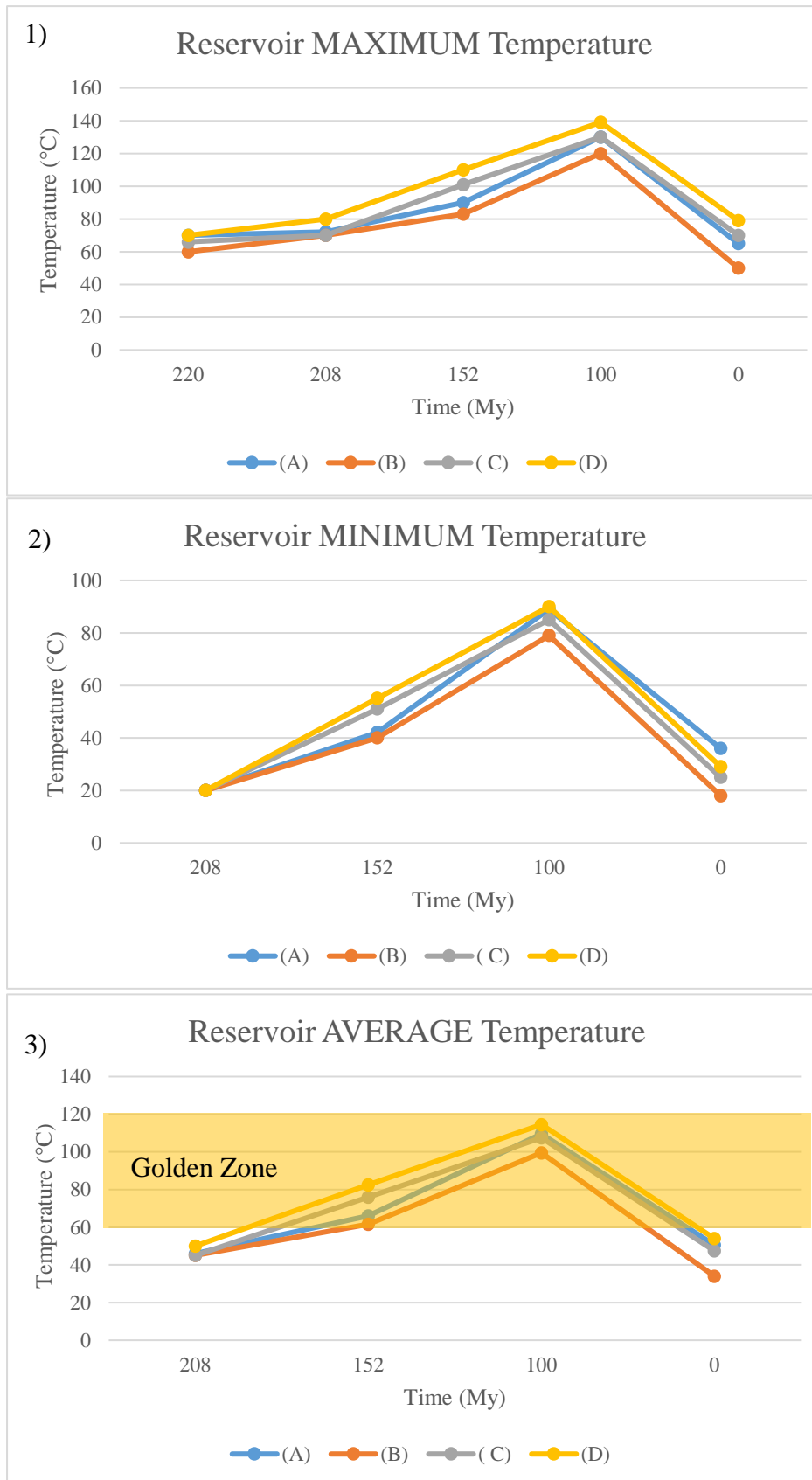


Figure 39 - Reservoir temperature to time plots for section 2. (1) Maximum temperature values of the reservoir units; (2) Minimum temperature values of the reservoir units; (3) Average temperature values of the reservoir units.